Numerical Simulation of Deep-Sea Minings Plume Using Arbitrary, Non-Orthogonal Mesh

Agung Christy Rado Togaraja Simarmata

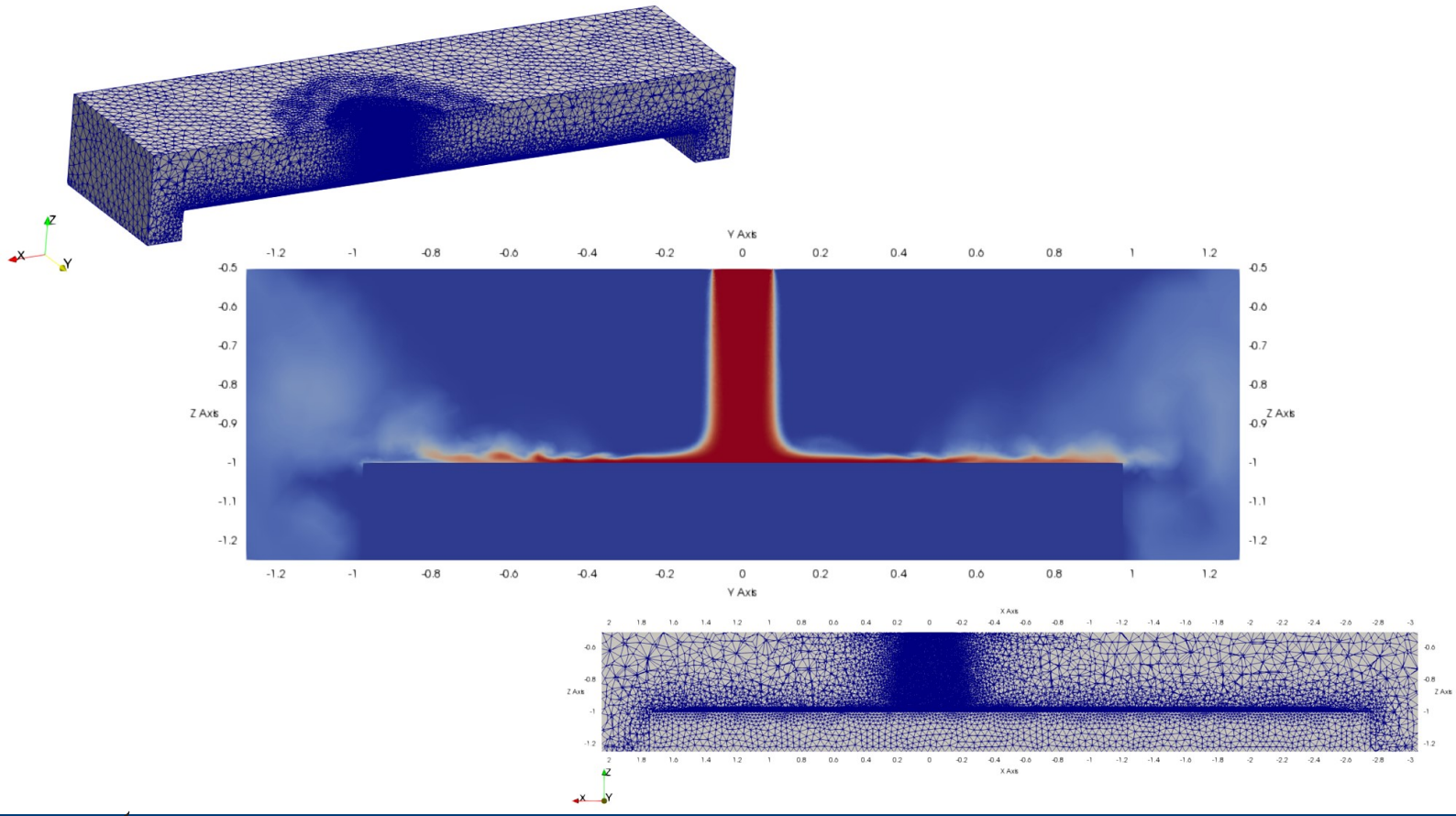

TU Delft

Numerical Simulation of Deep-Sea Minings Plume Using Arbitrary, Non-Orthogonal Mesh

by

Agung Christy Rado Togaraja Simarmata

to obtain the degree of Master of Science Offshore and Dredging Engineering
at the Delft University of Technology,
to be defended publicly on Monday October 14, 2019 at 14:00 PM.

Student number:	4687124	
Thesis committee:	Prof. Dr. ir. C. van Rhee,	TU Delft
	Dr. ir. G. H. Keetels,	TU Delft
	Ir. F. van Grunsven,	TU Delft

TU Delft

Preface

This report is the result of my graduation research to obtain master degree in MSc Offshore and Dredging Engineering program, Delft University of Technology. This graduation thesis aims to explore the applicability of implementing arbitrary non-orthogonal mesh to the simulation of Deep-Sea Mining tailings plume, to study the flow behavior of the tailings plume and hopefully asses the environmental-impact of the tailings for the sake of sustainable Deep-Sea Minings operation in the future.

The journey of this thesis and master life are not walk in a park to be honest. However every joy and struggle processed me to be a better person. As the wise man said, a quite sea never creates a great sailor. I realized I have learned a lot of things in this journey and I can not be more grateful for this opportunity. Therefore I would like to thank these special people which support me throughout this journey.

First of all, I would like to say my highest praise and thanks to Jesus Christ, my Lord and Saviour. Only by His grace that I am able to stand and reach this point in my life. Whatever happens in my life, You are always good, Lord. I am ready for the next bigger challenge.

Secondly, I cannot express my sincere gratitude to my graduation committee, who has supported me throughout this graduation research. To Dr. ir. G. H. Keetels and Prof. Dr. ir. C. van Rhee, thank you for your patience, kindness, and willingness to take me as one of your graduate students and guide me throughout this thesis. To Ir. Frans van Grunsven, thank you for not only being a supportive graduation committee, but also a good friend. I will never forget all of your support, such as responding to my email early in the morning, going to the university during the weekends so I can have a discussion with you, and many more that I can not write down.

I would like to thanks my family (Mom, Dad, and Mutiara Simarmata) for the unconditional love, constant support, and the opportunity so that I can process myself in this beautiful country. I would like to thank you as well to my brother, Charles Simarmata, who is always supporting me since the first day I arrived in the Netherlands, and also to all of my uncles, aunts, cousins, nephews, and nieces from Simarmata and Silalahi family who always cheering and supporting me in every video calls. Last but not least, I dedicate this thesis to my Grandma, Tiamsa br. Simanjuntak, who passed away in the middle of my thesis work. I am sorry that I can not make you see me graduating once again, but I hope you see me proudly from the Heaven above now. I love you, Grandma.

I want to say thank you to all my Indonesian friends and colleagues in Delft, and especially PPI Delft. Thank you for all your trust and support throughout these years. To Ingrid Sitorus, Floriana Ayumurti, Grace Peranginangin, Yosep Pandji, Hanif Dinul, Fadhil Qamar, Eureka Mahaerani, Haris Suwignyo, and Caecilia Grace, thank you for everything.

Finally, I want to say a special thanks again to Ingrid Sitorus for always supporting and believing me in every situation. Let us go to the next challenge and level.

Delft, October 2019

Agung Christy Rado Togaraja Simarmata

Summary

In recent years, the demand for minerals and rare-earth elements are escalating due to rapid technological advancements and developments. This condition raises the importance of Deep-Sea Mining (DSM) as an option to fulfill the global demands, for the sake of future ambitious projects. On the other hand, DSM still faces some drawbacks and obstacles in its operations, e.g. environmental impact of its tailings discharge. Thus, the presence of tools for predicting the behavior and environmental impact of DSM tailings becomes crucial for the sake of conducting sustainable DSM operations. Researches, both numerical and laboratory experiments, are then done to achieve this goal.

In the study of DSM tailings behavior through numerical simulation, the challenge lies in the ability to implement the complex physics phenomena around DSM plumes to a numerical model. This research is thus aimed to observe one of the parts of the so-called physical phenomena, and numerical constraints on the simulation of DSM plumes: the effects of implementing arbitrary non-orthogonal mesh. Arbitrary non-orthogonal mesh would give users the freedom to refine the mesh based on the required resolution on a certain area in the simulation domain.

In this research, an arbitrary non-orthogonal mesh is constructed forming a domain geometry of 3D tank with round pipe as a source of tailings discharge, adapting the laboratory setup of Byishimo (2018). Mesh refinement is done around the pipe discharge area, where the jet mainstream expected to occur, and near the bottom, where settling of solids fraction and high velocity-gradients are expected to occur. Top-hat approximation theory is then used for defining the inlet boundary condition of the simulation domain, and smooth solid wall is used for the bottom boundary.

In observing the effect of arbitrary mesh, two parameters are varied: solids settling rate, and differentiation scheme. Following this, six simulation cases are prepared, containing three solids-settling conditions (minimum, realistic, and extreme solids fraction settling) and two differentiation schemes (Gauss Gamma and Gauss Linear). These cases are then simulated using the CFD drift-flux model in OpenFOAM for two incompressible fluids, with ambient fluid and tailings mixture as the two incompressible fluids. Turbulence is modeled using LES method, with Wall-Adapting Local Eddy-viscosity (WALE) LES model for modeling the subgrid-scale of the turbulence. Two simulated field variables are picked to be observed and compared with the laboratory measurement data: flow velocities and local Suspended Solids Concentration (SSC).

Simulations show that the constructed domain able to generate stable results using not only Gauss Gamma differencing scheme but also Gauss Linear, which originally expected to give unbounded results. From simulations with various solids settling conditions, it is analyzed that the implementation of solids settling using the mentioned function leads to constant settling rate with inability to re-suspend the settled solids. Thus, simulation of cases with extreme solids settling leads to hyper-concentration of solids fraction in the cells on the bottom. The top-hat profile of the inlet boundary condition is constantly sustained throughout the simulation, resulting in uniform jet vertical velocity profile. The simulations also show that momentum-driven jet-like flow can be observed around the impingement point, while gravity current generated further from the impingement point.

The simulation results show that the mesh refinement is enabling simulating and validating the flow with

the required resolutions. Moreover, the constructed domain also shows that Gauss Linear can be used for simulating DSM plumes, furthermore using full tank domain. The simulated SSC also turns out not only affected by the simulation domain and mesh, but also the differencing scheme, and the presence of settling and pick-up functions.

Keywords: CFD, tailings plume, non-orthogonal mesh, solids settling, buoyant-jet, deep-sea mining

Contents

List of Figures

List of Tables

Abbreviations & Symbols

Abbreviations

CFD	Computational Fluid Dynamics
CV	Control Volume
DSM	Deep-Sea Mining
DNS	Direct Numerical Simulation
DSTP	Deep-Sea Tailings Placement
FV	Finite of Volume
GAMG	Geometric Agglomerated Algebraic Multigrid
LES	Large Eddy Simulation
LHS	Left-Hand Side
NVD	Normalised Variable Diagram
OpenFOAM	Open-source Field Operation And Manipulation
PISO	Pressure Implicit with Splitting of Operator
RAS	Reynolds Average Simulation
RHS	Right-Hand Side
SIMPLE	Semi-Implicit Method for Pressure-Linked Equations
SSC	Suspended Solids Concentration
WALE	Wall-Adapting Local Eddy-viscosity
ZEF	Zone of Established Flow
ZFE	Zone of Flow Establishment

Symbols

Greek Symbols

B	Plume width
b_j	Jet width
b_p	Plume width
$\bar{c}$	Average concentration
Co	Courant number
C_1	Ferguson coefficient 1
C_2	Ferguson coefficient 2
C_w	WALE coefficient
c_m	Maximum concentration in Gaussian profile
d_p	Particle diameter
D	Source diameter
E	Neighboring CV
F	Face flux, buoyancy flux
f	Face of CV
g	Gravitational vector
g'	Specific gravity
l_s	Length scale
M	Momentum flux
n	Richardson-Zaki coefficient
P_m	Mixture pressure
Q	Mass flux
r	Radial direction
Re_p	Particle Reynolds number
$\bar{S}$	Average dillution
$\mathbf{dS}$	Surface area vector
$\delta\mathbf{S}$	Closed-bounding surfaces of a CV
S_{ij}	Rate-of-strain tensor
$\mathbf{T}$	Viscous shear stress
$\mathbf{T}^t$	Turbulent shear stress
$\mathbf{v}_m$	Mixture velocity
$\mathbf{v}_k$	Phase velocity
$\mathbf{v}_t s$	Terminal settling velocity
$\mathbf{v}_p$	Particle velocity
$\mathbf{v}_f$	Fluid velocity
$\mathbf{v}_{km}$	Phase relative-velocity to the mixture velocity
z	Vertical distance

Latin Symbols

B	Plume width
b_j	Jet width
b_p	Plume width
$\bar{c}$	Average concentration
Co	Courant number
C_1	Ferguson coefficient 1
C_2	Ferguson coefficient 2
C_w	WALE coefficient
c_m	Maximum concentration in Gaussian profile
d_p	Particle diameter
D	Source diameter
E	Neighboring CV
F	Face flux, buoyancy flux
f	Face of CV
g	Gravitational vector
g'	Specific gravity
l_s	Length scale
M	Momentum flux
n	Richardson-Zaki coefficient
P_m	Mixture pressure
Q	Mass flux
r	Radial direction
Re_p	Particle Reynolds number
$\bar{S}$	Average dillution
$\mathbf{dS}$	Surface area vector
$\delta\mathbf{S}$	Closed-bounding surfaces of a CV
S_{ij}	Rate-of-strain tensor
$\mathbf{T}$	Viscous shear stress
$\mathbf{T}^t$	Turbulent shear stress
$\mathbf{v}_m$	Mixture velocity
$\mathbf{v}_k$	Phase velocity
$\mathbf{v}_t s$	Terminal settling velocity
$\mathbf{v}_p$	Particle velocity
$\mathbf{v}_f$	Fluid velocity
$\mathbf{v}_{km}$	Phase relative-velocity to the mixture velocity
z	Vertical distance

1

Introduction

In recent years, the demand for minerals and rare-earth elements are escalating, due to rapid technology developments (Dutta et al., 2016). The global focus on developing technologies for industries, such as renewable energies, creates a global environment that requires high usage of minerals. This condition urges the mining industry to expand its operations for fulfilling the mentioned demands. Soon mining stakeholders are required to seek an alternative exploration option besides onshore mining. The rising land usage for residences and the latest This condition raises the importance of Deep-Sea Mining, as an option for fulfilling this demand, for the sake of future ambitious projects. With its great potential lies within, DSM has become a hot topic among mining industry for several decades. Researches aiming to investigate the feasibility of executing one has been around since 1960s, with a pilot project conducted in Japan. Nevertheless, DSM sector is still considered to be at an early stage of development, where drawbacks still need to be answered and solved before conducting a sustainable DSM operation.

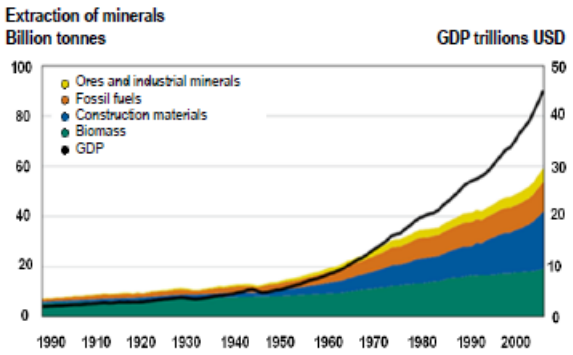

Figure 1.1: The growth of mineral resources demand in the world economy (Dubiński, 2013)

One of the drawbacks of DSM operation is the environmental impact of its waste-water (tailings), see Figure 1.2. Due to geographical and economic considerations, conventional tailings management method (using onshore tailings dam) is considered not feasible for DSM operation. Thus in 1977, a method called Deep-Sea Tailings Placement (DSTP) was proposed. By using DSTP, tailings are discharged back to the deep-sea through a submerged pipe and expected to remain on the bed due to settling (Ramirez-Llodra et al., 2015).

This method is considered as a suitable method for DSM operation. Although its advantages, DSTP method still creates number of environmental impacts that still not yet understood completely, such as plume generation on the seafloor, turbidity occurrence in the water column, and addition of bottom sediments (Sharma, 2015). To ensure a fulfilment to the requirement for the environmental policy for the sake of a sustainable DSM operation, a tool for predicting the behavior of Deep-Sea tailings plume, and consequently its environmental impact, is crucial. Researches are then done, both through numerical and laboratory experiments, for observing and understanding the behavior of the flow created by tailings discharge.

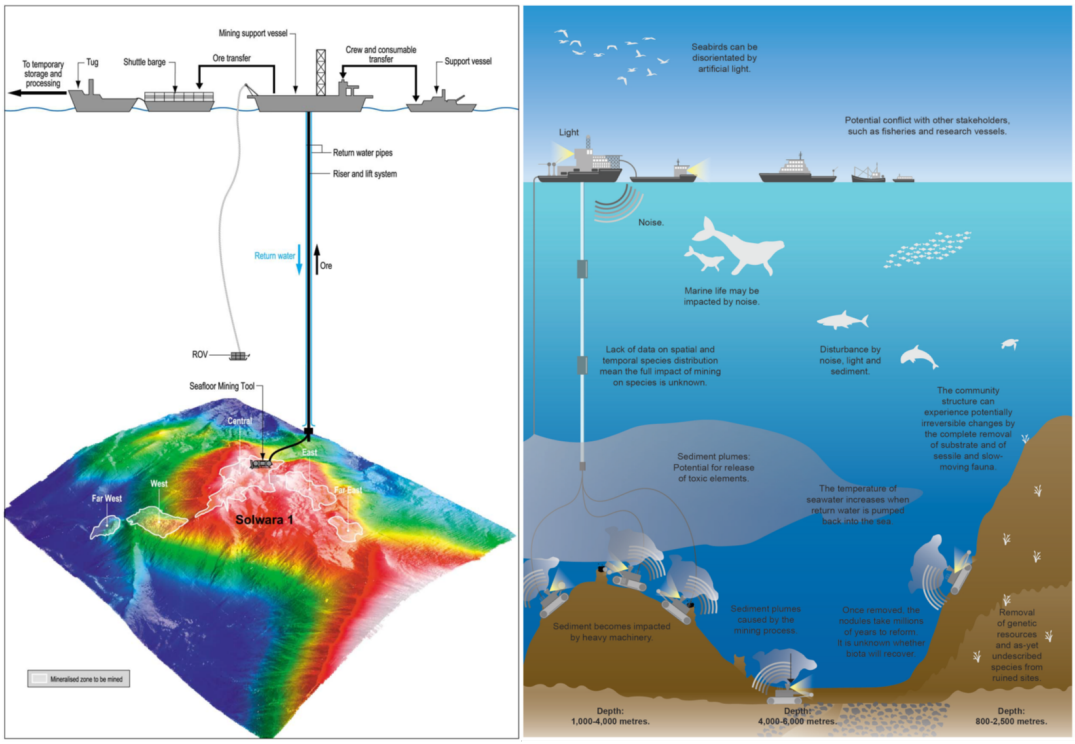

Figure 1.2: (left) Schematic illustration of DSM operation (Hoagland et al., 2010) and (right) its environmental impact (Miller et al., 2018)

1.1. Problem Identification

In the study of Deep-Sea Minings plume through numerical simulation, the challenge lies in the implementation of the complex physics phenomena and constrains around the plume to a numerical model. Researches are then done to observe the implementation of each physics phenomenon individually and explore the possibility of constructing a proper numerical model for simulating the Deep-Sea Minings plume. Some of these researches are briefly summarised as follows.

van Grunsven et al. (2016) did numerical simulations to observe the interaction between a turbidity source and its environment. In this research, the main focus is the interaction between turbidity source with cross-flow, submerged pipe, and various source types (plane and round). van Grunsven et al. (2016) used structured block mesh for constructing the simulation domain, which is a 3D tank geometry. It was found in this research that simulations using LES method show a considerably good agreement with measurement data.

Byishimo (2018) also did laboratory experiments and numerical simulations for observing the development of DSM tailings with various discharge conditions, and its interaction with two types of seabeds: flat and inclined by 10 degrees. The main goal of the research was to observe and also provide necessary mea-

surement data for further use in validating similar numerical simulations. Both laboratory experiments and numerical simulations were done by using domain setup of a tank with scale of 1:50, representing actual field dimensions of 255m (length), 113m (width), and 105m (height). Numerical simulations were done using structured orthogonal mesh, and LES model as in De Wit (2015).

In the numerical researches done so far, it is found that some simulation area requires higher resolution compared to other areas. This treatment is important especially in simulation domain where high gradients are expected to occur. On the other hand, such treatment is limited when orthogonal mesh is used in constructing the domain mesh. Thus an idea is proposed to observe the effect of implementing arbitrary, non-orthogonal mesh.

Summarising the identified problems, the main goal of this research is formulated:

"To numerically simulate Deep-Sea Minings Plume using arbitrary, non-orthogonal mesh"

For achieving this research goal, some simulation cases are prepared for answering the following questions:

- How is the simulated DSM plumes using non-orthogonal mesh, with various solids settling condition?
- How is the simulated DSM plumes using non-orthogonal mesh, with various differentiation schemes?
- How is the simulated DSM plumes compared with laboratory measurement data?

1.2. Research Approach

In this research, numerical simulations are done using a method called Computational Fluid Dynamics (CFD). Since tailings mixture can be considered as a fluid mixture, CFD is seen as a proper method. The numerical simulation is then done using the drift-flux model (Brennan, 2001) for a system of a multiphase flow consisting of two incompressible fluids. The drift-flux model would save some computational cost since it solves only one momentum equation of the mixture, not the momentum equation of each phase in the system. The tailings mixture is modeled as a slurry, consisting of monosize solid fraction. The settling of solid fraction within the tailings mixture is modeled using the formulation of terminal settling velocity of Ferguson and Church (2004).

The numerical simulation is done using a software called OpenFOAM (Open-source Field Operation and Manipulation) version of 1706 (*OpenFOAM-v1706*). The governing equations of the flow are discretized using Finite of Volume method. The used drift-flux model can be found in the OpenFOAM as a solver named *driftFluxFoam*.

1.3. Research Outline

The outline of this research is as follow:

- Chapter 1
  In this chapter, the reader is presented with the introduction of the research, including the background story of the research, the identified problem of the research, and also the research goal. The approach of the research is also presented in this chapter.
- Chapter 2
  This chapter presents the background theory related to physics phenomena occurred when tailings mixture is discharged to a deep-sea environment. This chapter also addresses how is the interaction between the tailings mixture and solid seabed as it impinges the seabed.

- Chapter 3

  In this chapter, the modeling techniques used in this study are presented. These include how to model the tailings mixture and its governing equations. The modeling of the settling of the solids fraction in the mixture is also discussed in this chapter. Another important subject within tailings flows modeling is the modeling of the turbulence. This is also addressed in this chapter.

- Chapter 4

  Chapter 4 presents the numerical implementation of the flow governing equations to the numerical model. In this study, the governing equations are implemented using the Finite of Volume method. The discretization of the simulation domain using non-orthogonal Control Volume and the discretization of the flow governing equations are presented in this chapter. In OpenFOAM, these numerical implementations are done by choosing available algorithms within it. In this study, PIMPLE algorithm is used and also discussed within this chapter.

- Chapter 5

  In this chapter, the preparation of the flow model is discussed, such as the simulated cases, the geometry of the simulation domain, the mesh construction, and the boundaries. In this study, two simulation domains are used due to computational constraints. The motive and preliminary study regarding the reconstruction of the domain are also presented in this chapter. The decomposition method used to simulate in parallel also describes in this chapter.

- Chapter 6

  This chapter presents the result of the simulations. The validation method of the simulation results is also discussed in this chapter. The resulting spatial plot of the simulated SSC and flow velocities are also discussed in this chapter, as well as the validation results.

- Chapter 7

  This report then ends with an overview of the insight found in this research, summarised in conclusion points. This chapter also proposes some recommendations for future researches.

2

Physics Around DSM Tailings Plume

In studying the behavior of DSM tailings plume, questions may arise regarding what physics phenomena occur as a tailings mixture discharged to deep-sea environment. This chapter addresses such of this. The chapter mainly consists of two parts. The first part focuses on briefly describing the physics phenomena occurring around DSM plume, starting from the discharge point until its interaction with ambient environment and seabed. The addressed physics phenomena are such as classification of tailing discharge as a buoyant-jet, mixing occurred during discharging, entrainment of ambient water, and also top-hat approximation method. Then the chapter continues with the second part, focusing on how to mathematically describe tailings buoyant-jet flow in a set of governing equations. In this research, drift-flux approach is used to determine the motion between each phase in the tailings flow (Zuber and Findlay, 1965).

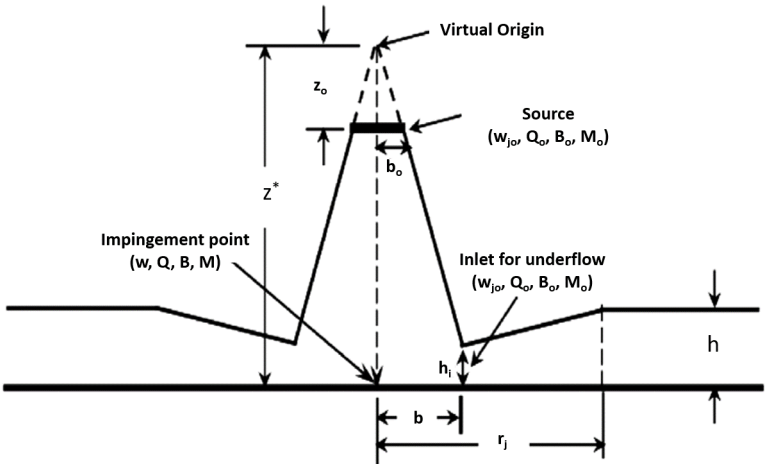

Figure 2.1: Schematic illustration of a discharging dense vertical buoyant-jet, adopted from Chowdhury and Testik (2014)

2.1. Deep-Sea Tailings Plume As A Buoyant-Jet

A discharged dense fluid, such as tailings, can be classified as a jet or plume, see Table 2.1. In this research, DSM tailings discharge is considered as a vertical buoyant-jet (Lee and Chu, 2012). Tailings mixture experi-

ences both continuous buoyancy and momentum fluxes at its discharging source. This buoyancy flux occurs due to the density difference between tailings and the ambient fluid (seawater). Moreover the presence of solids fraction in the tailings mixture is the cause of this density difference. Since solids fraction is heavier and denser than seawater, this buoyancy flux results in a downward motion of the mixture. On the other hand, tailings mixture also experiences momentum flux at its source due to the momentum coming from the jet. Since both fluxes work in the same direction, buoyancy and momentum fluxes amplified, resulting in the same downward motion of the tailings flow (List, 1982), see Figure 2.1.

Table 2.1: Flow classifications based on the source type (Lee and Chu, 2012)

Source Type	**Source Duration**	
	Continuous	**Intermittent**
Momentum	Jet	Puff
Buoyancy	Plume	Thermal
Momentum + Buoyancy	Buoyant-Jet	Buoyant-Puff

For a vertical buoyant-jet discharged through a round-source, there are four important flow parameters, defining the development of the flow: initial discharge velocity w_{jo}, initial volumetric flux Q_o, initial momentum flux M_o, and initial buoyancy flux F_o. These parameters are mathematically expressed as (Jirka and Domeker, 1991):

$$Q_o = \frac{\pi D^2}{4} w_{jo} \tag{2.1}$$

$$M_o = Q_o w_{jo} \tag{2.2}$$

$$F_o = Q_o g' \tag{2.3}$$

Where D is the source diameter, and g' is called specific gravity, and mathematically expressed as:

$$g' = \frac{\rho_m - \rho_a}{\rho_a} g \tag{2.4}$$

Where ρ_m is the mixture density, ρ_a is the ambient-water density, and g is gravity acceleration $[m/s^2]$. For tailings mixture, the specific gravity can be calculated using the volumetric concentration of the solids fraction in the tailings mixture. This specific gravity is mathematically calculated as Byishimo (2018):

$$g'_o = g\,\alpha_{s,o} \left(\frac{\rho_s - \rho_w}{\rho_w} \right) \tag{2.5}$$

Where $\alpha_{s,o}$ is the initial volumetric concentration of solids fraction in tailings mixture, ρ_s is the solids fraction density, and ρ_w is the water density.

As tailings buoyant-jet discharges, physics phenomena, such as mixing and entrainment, occurs between tailings mixture and the ambient water. These are addressed in the following section.

2.2. Mixing of Tailings Buoyant-Jet

For vertical buoyant-jet, mixing between the discharged mixture and ambient water behaves differently with distances from discharging source. This mixing classification is affected by the intensity of buoyancy and momentum fluxes experienced by the discharged mixture at each distance from the source. As the tailings mixture propagates further from the source, the balance between momentum and buoyancy fluxes are changing.

A parameter in this classification is called length-scale l_s. The momentum flux experiences by the tailings mixture from the jet source decay with distance, thus lowering the input of kinetic energy to the tailings mixture. Consequently, buoyancy flux will dominate over momentum flux at a certain distance. This distance is thus called the length-scale l_s.

For calculating the length-scale, the contribution of each flux to a flow motion should be treated separately. Consider a flow generated only by momentum flux. The velocity at a certain distance z from the discharging source is estimated as (Lee and Chu, 2012):

$$w_j \approx 7M_o^{1/2} z^{-1} \tag{2.6}$$

On the other hand, for a flow generated only by buoyancy flux, the velocity at a certain distance z from the discharging source is (Lee and Chu, 2012):

$$w_p \approx 4.7F_o^{1/3} z^{-1/3} \tag{2.7}$$

Then, length-scale can be estimated as a distance from source where momentum-induced velocity w_j is approximately equal to the buoyancy-induced velocity w_p:

$$l_s \approx \frac{M_o^{3/4}}{F_o^{1/2}} \tag{2.8}$$

By using this length-scale, the buoyant-jet is expected to behave plume-like, and the mixing is buoyant-dominated for vertical distance z with $z/l_s > 1$. On the other hand, the buoyant-jet is expected to behave jet-like and thus creating jet-dominated mixing for vertical distance z with $z/l_s < 1$.

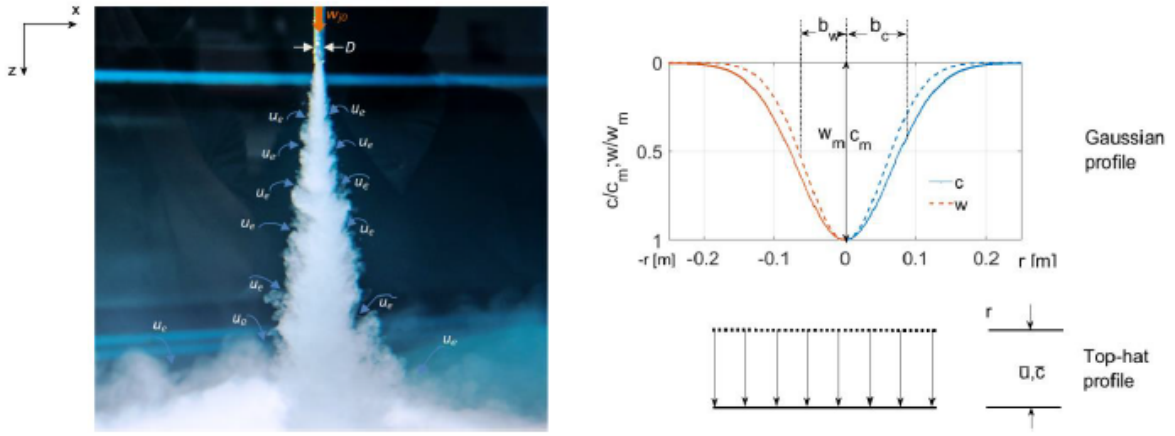

Figure 2.2: *(left)* Illustration of entrainment in vertical buoyant-jet, *(upper-right)* its resulting Gaussian profile of the streamwise velocity and SSC, and *(lower-right)* and its top-hat approximation profile, adopted from Byishimo (2018)

2.3. Entrainment of Ambient Water

Another physics phenomenon that occurs during the discharging of tailings mixture is the entrainment of ambient water to the main jetstream, see Figure 2.2. Entrainment causes the momentum and buoyancy fluxes of the tailings buoyant-jet to approach ambient values. Concerning entrainment, Lee and Chu (2012) classified plume spatial region into two zones: Zone of Flow Establishment (ZFE) and Zone of Established

Flow (ZEF).

ZFE is the region located in a range of distance $z < 6.2D$ from the discharging source, where D is the source diameter. In this region, the profile of streamwise velocity and Suspended Solids Concentration (SSC) are uniform, with value of the initial streamwise velocity and SSC (Lee and Chu, 2012).

$$w(z,r) = w_{jo} \tag{2.9}$$

$$C(z) = C_o \tag{2.10}$$

Where C_o is the initial SSC at the dischraging source. Meanwhile, ZEF is the region located in a range of distance $z > 6.2D$. In this region, the profiles of streamwise velocity and SSC are following Gaussian profile.

$$w(z,r) = w_m(z)exp(-\left(\frac{r}{b_w}\right)^2) \tag{2.11}$$

$$C(z,r) = C_m(z)exp(-\left(\frac{r}{\alpha b_c}\right)^2) \tag{2.12}$$

Where z, r are streamwise and radial coordinates, w_m and C_m are respectively maximum streamwise velocity and SSC, located at the centerline of the jetstream.

2.3.1. Top-Hat Approximation

For many practical problems, a Gaussian profile would result in an extensive analysis. A method is therefore required to approximate the necessary profile of buoyant-jet flow velocity and SSC. A method called top-hat approximation was introduced. In this method, the profile of buoyant-jet velocity and SSC are approximated as uniform profiles across the jet (Lee and Chu, 2012). These are assumed to represent the overall mass and momentum transports in the flow, which responsible for the large eddies in the jet. The top-hat approximation is mathematically expressed as:

$$W = \frac{w_m}{2} \tag{2.13}$$

$$B = \sqrt{2}\, b_j \tag{2.14}$$

$$\bar{C} = \frac{C_o}{\bar{S}} \tag{2.15}$$

Where W, B, and $\bar{C}$ are respectively the top-hat velocity, plume-width, and average concentration, w_m is the centerline velocity of the jet, b_j is the jet-width, C_o is the initial SSC, and $\bar{S}$ is average dilution of the plume. The resulting top-hat profile can be seen in Figure 2.2. Top-hat approximation offers analytical simplicity in analyzing the profile of the buoyant-jet, and also avoid the ambiguity in profile assumption at the transition between flow regimes. Besides, it also provides simplicity in mathematical derivations.

2.4. Tailings Buoyant-Jet Interaction With Seabed

Besides interacting with the surrounding water, tailings buoyant-jet which released at deep-sea environment will also interact with the ocean bed, which represents a solid boundary. As a buoyant-jet impinges a solid bottom, its flow propagates radially away from the impingement point (Chowdhury and Testik, 2014). This flow is called underflows or outflows. Chowdhury and Testik (2014) also stated that this underflow experiences two main propagation phases: (a) initial adjustment propagation phase at a distance near the impingement point and (b) gravity current propagation phase. Experiments done by Kotsovinos (2000), Lawrence and

Maclatchy (2001), Kaye and Hunt (2007), and Cooper and Hunt (2007) showed that the first propagation phase of the underflows (i.e. the initial adjustment propagation phase) is a momentum-driven wall jet-like phase. As the underflow propagates further from the impingement point, buoyancy becomes more dominant over momentum. Thus the underflow behaves as a fully-developed gravity current.

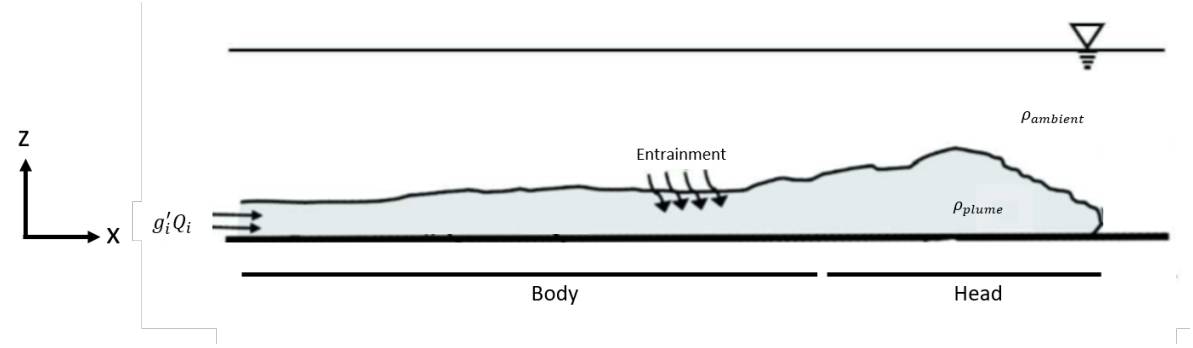

Figure 2.3: Illustration of gravity current structure (Ahmed, 2017)

Gravity current, itself, is a flow of fluid with a certain density in a certain ambient fluid with different density (Ahmed, 2017). For bottom gravity currents, it is usually identified by the presence of a head region at the front of the flow, and followed by its body (see Figure 2.3). As the flow propagates, the head must displace the stationary ambient water. Thus it results in a thicker size compared to the body.

The typical profile of the velocity of a bottom gravity-current usually can be decomposed vertically into the inner region and outer region (Ahmed, 2017), see Figure 2.4. These regions are separated by a vertical height where maximum velocity occurs. The inner region consists of a positive velocity gradient. Therefore it behaves like a conventional turbulent boundary layer. On the other hand, the outer region consists of a negative velocity gradient, resulting it as a shear layer. The vertical location of the maximum velocity depends on the ratio of the shear forces between the outer and inner regions.

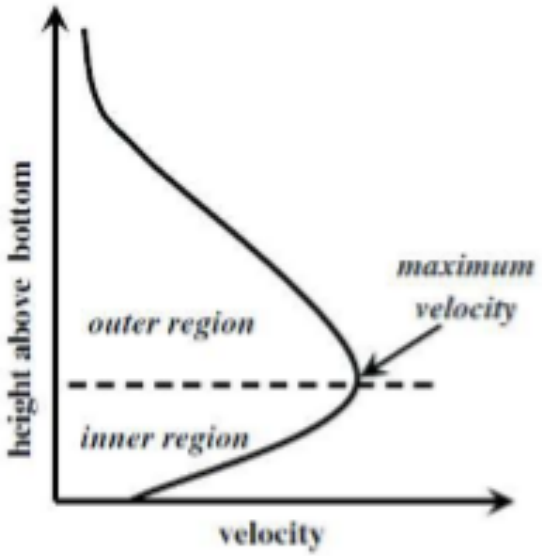

Figure 2.4: Typical velocity profile of a bottom gravity current (Ahmed, 2017)

3

Modeling Techniques

3.1. Tailings Mixture Modeling

In the practical, tailings mixture is a multiphase liquid, consisting of water as a continuous phase or carrier fluid, and solids fractions dispersing within the continuous phase. Each of these phases fills the mixture volume with each certain volumetric concentration. As tailings mixture usually consists of multiple solids fractions, the resulting flow consists of two or more phases. The computational cost for this flow condition is considerably large. Thus an alternative method is implemented in this research.

In this research, the tailings mixture is modeled as a continuum slurry, consisting of single solid fraction. By using continuum approach, the obligation to describe each particle motion is neglected. The solid fraction in the mixture is assumed to fill the whole volume of the fraction uniformly. The resulting flow governing equations are as follows.

3.1.1. Flow Governing Equations

In this research, drift-flux modeling is used for governing the flow motion. By using the drift-flux model, the momentum equation for each phase is summed together, yielding a single mixture momentum equation (Brennan, 2001). Thus the governing equations for the flow are as follow. For the derivations, see Zuber and Findlay (1965), Manninen et al. (1996), Brennan (2001), Ishii and Hibiki (2010), and Goeree (2018). A short derivation of the flow governing equations is also presented in Appendix section. The governing equations are as follow:

Mixture Continuity Equation

The mixture continuity equation is defined as:

$$\frac{\partial \rho_m}{\partial t} + \nabla \cdot (\rho_m . \mathbf{v}_m) = 0 \tag{3.1}$$

Where ρ_m and $\mathbf{v}_m$ are respectively the mixture density and velocity vector.

Mixture Momentum Equation

The mixture momentum equation is defined as:

$$\frac{\partial \rho_m \mathbf{v}_m}{\partial t} + \nabla \cdot \left(\rho_m \mathbf{v}_m \mathbf{v}_m\right) = -\nabla P_m + \nabla \cdot \left[\mathbf{T} + \mathbf{T}^t - \sum_k \alpha_k \rho_k \mathbf{v}_{km} \mathbf{v}_{km}\right] + \rho_m \mathbf{g} \tag{3.2}$$

Where P_m, $\mathbf{T}$, $\mathbf{T}^t$, $\mathbf{v}_{km}$, and $\mathbf{g}$ are respectively the mixture pressure, viscous and turbulent shear stress tensor, phase relative-velocity with respect to mixture velocity, and gravitational acceleration vector.

Disperse-Phase Transport Equation

The transport equation for the phases in the two-phase flow system is defined as:

$$\frac{\partial \alpha_k \rho_k}{\partial t} + \nabla \cdot \left(\alpha_k \rho_k \mathbf{v}_k\right) = 0 \tag{3.3}$$

Where α_k, ρ_k, and $\mathbf{v}_k$ respectively the phase volumetric concentration, density, and velocity vector.

3.2. Solids Settling Modeling

In this research, the settling of the solid fraction within the tailings mixture is done by implementing the terminal settling velocity of a particle of the solid fraction as the phase relative-velocity in the drift-flux model. As mentioned before, tailings mixture is assumed to be filled by monosize fraction. Thus, the terminal settling velocity of a particle of this solid fraction is assigned as the settling velocity of whole particle of the tailings mixture.

In this research, the Richardson-Zaki relative velocity model is assigned to calculate the mentioned relative velocity. Consider the tailings mixture as the dispersed-phase (subscript d) within this two-fluid system, the relative velocity of the dispersed phase to the mixture velocity is calculated as (Richardson and Zaki, 1997):

$$\mathbf{v}_{dm} = \frac{\rho_c}{\rho} \mathbf{v}_{ts} (1 - \alpha_d)^n \tag{3.4}$$

Where $\mathbf{v}_{ts}$ is the terminal settling-velocity of a single solid particle in the mixture, α_d is the disperse-phase volumetric concentration, and n is the Richardson-Zaki coefficient. This formulation is equal to the calculation of a hindered settling velocity for particle with a certain concentration. The terminal settling velocity is calculated using formula of Ferguson and Church (2004):

$$w_o = \frac{\Delta g d^2}{C_1 \nu + \sqrt{0.75 C_2 \Delta g d^3}} \tag{3.5}$$

Where d is the particle diameter, ρ_s is the solid-particle density, ρ_w is the water density, and ν is the water kinematic viscosity. For natural sands, C_1 and C_2 are 18 and 1. For spherical particles, the value for C_1 and C_2 are 1 and 0.44. Richardson-Zaki coefficient is calculated using the formula of Rowe (1987), which smoothly represents the empirical formulation of Richardson-Zaki.

$$n = \frac{4.7 + 0.43 \cdot Re_p^{0.75}}{1 + 0.175 \cdot Re_p^{0.75}} \tag{3.6}$$

Where Re_p is particle Reynolds number and calculated as:

$$Re_p = \frac{\rho_w \left|\mathbf{v}_w - \mathbf{v}_p\right| d_p}{\nu_w} \tag{3.7}$$

With $\mathbf{v}_p$ is the velocity of the particle, ρ_f is the fluid density, ν_f is the fluid kinematic-viscosity, and d_p is the particle diameter.

3.3. Turbulent Modeling

In this research, turbulent is modeled using Large Eddy Simulation (LES) method. In LES method, the turbulence in a three-dimensional turbulent flow is classified into two scales: (a) larger unsteady motions and (b) smaller scale motions. Eddies larger than the grid size, which are considered as the larger unsteady motion, are directly solved while eddies smaller than the grid size are modeled using subgrid-scale modeling. LES is expected to be a solution to overcome the extensive computational price of Direct Numerical Simulation (DNS) method and the accuracy of Reynolds Averaging (RAS) method. In summary, there are four important conceptual steps in LES (Pope, 2001):

1. Filtering operation.
   By using filtering, the field variables (*e.g.* flow velocity) are spatially filtered into two components: spatially-filtered component, which represents the large scale of turbulent, and subgrid-scale component.

2. The evolution of filtered field variables are derived from Navier-Stokes equations.

3. Closure is done by implementing a model for the subgrid-scale eddy-viscosity.

4. The filtered equations are then modeled to obtain the approximation of the large-scale motion of the flow in one realisation.

A thing to be considered in LES method is the selection of the subgrid-scale model. In this research, WALE LES model is used to model the turbulent subgrid-scale tensor. For further derivations and implementation of LES to the flow governing equations, see Wilcox et al. (1998), Pope (2001), and Goeree (2018).

3.3.1. WALE LES Model

In WALE LES Model, the turbulent eddy-viscosity is modeled as:

$$\mu_t = \rho C_w \Delta V^{1/3} \frac{S_{ij}^d S_{ij}^d}{\bar{S}_{ij} S_{ij} + (S_{ij}^d S_{ij}^d)^{5/4}} \tag{3.8}$$

Where C_w is the constant in the model, S_{ij} is the rate-of-strain tensor, and ΔV is the filter size which equals to the cell size. In this research, the assigned value of C_w is 0.0325, the default value of C_w. WALE LES model is picked as it is considered to be more stable compared to Smagorinsky model for simulating flow impinging to a solid boundary since it is developed for industrial applications that contain complex geometries and shapes (Goeree, 2018).

4

Numerical Implementation

To simulate the tailings buoyant-jet flow, the governing equations of the flow should be implemented to the numerical model. There are several methods available for doing the implementation. The widely used discretisation methods are Finite of Difference Method, Finite of Element Method, and Finite of Volume method. In this study, Finite of Volume method is used which is the main method of OpenFOAM (Greenshields, 2015). The discretisation of Navier-Stokes equations is addressed in this chapter, where special attention to the discretisation should be given as the domain is constructed using non-orthogonal mesh. In this research, Gauss Gamma and Gauss Linear differencing schemes are picked for discretisation of the advective and diffusive terms, while the temporal derivative is discretised using Backward Differencing scheme. The boundary conditions are also addressed in this chapter. In this study, the solution algorithm used in OpenFOAM is PIMPLE (Pressure Implicit with Splitting of Operator) algorithm, which is a combination of PISO and SIMPLE methods that are also available in OpenFOAM.

4.1. Finite of Volume Discretisation

To numerically simulate the turbulent buoyant-jet, the governing equations of the flow should be numerically implemented through discretization. In this research, the flow governing equations are discretized using Finite of Volume (FV) method. In general, the algorithm of FV method is as follow (Versteeg and Malalasekera, 2007):

- Governing equations are transformed to integral form.
- Simulation domain is divided into finite number of Control Volume (CV).
- Rate of change of field variables in each CV are determined by fluxes over the CV surfaces.
- Surface value of the field variables are calculated using differentiation scheme.

As can be seen from the algorithm above, FV method consists of two major steps: discretization of solution domain and discretization of flow governing equations. These are addressed in this section. Since the research uses non-orthogonal mesh, a special treatment is needed during the discretization.

4.1.1. Discretisation of Simulation Domain

The first step of the FV method is the discretization of the solution domain. The simulation domain is then divided into number of non-orthogonal Control Volume (CV), as can be seen in Figure 4.1. Each CV consists of one centroid point (P) and bounded by a set of flat faces (f). Each of these faces is shared with another neighboring CV.

In the simulation domain, CV faces can be classified into two types: internal faces and boundary faces. Internal faces are cell faces bounded between two CVs, while boundary faces are cell faces that coincide with boundaries of the simulation domain. This face is also represented by vector **S**, representing normal vector of the cell-face that pointing outward from the CV.

Non-orthogonal meshes give users higher freedom for creating mesh refinement in the domain area where higher resolutions are required. This property is useful in the practice of complex three-dimensional geometrical configurations (Jasak, 1996).

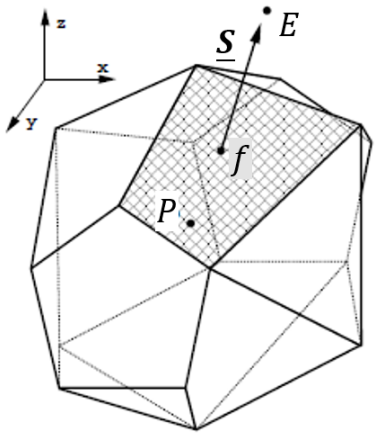

Figure 4.1: Illustration of non-orthogonal mesh (Jasak, 1996)

4.1.2. Discretisation of Flow Governing Equations

Here the discretization of flow governing equations is described. Once the simulation domain has been discretised, then the governing equations of the flow should be discretised. This is done by integrating the governing equations over each CV, and applying Gauss' theorem. An important concept that needs to be understood in this part of discretization process is the usage of Gauss theorem, which translates a volumetric integral to a surface integral. The Gauss theorem is mathematically expressed as follow:

$$\int_V \nabla \cdot \phi dV = \int_{\delta \mathbf{S}} \phi \cdot \mathbf{dS} \tag{4.1}$$

$$\int_V \nabla \phi dV = \int_{\delta \mathbf{S}} \phi \mathbf{dS} \tag{4.2}$$

Where **dS** is the surface area vector and δ**S** is the closed-bounding surfaces of the CV. This step results in a set of discretised equations, written in terms of the CV centre values. By using Gauss theorem, the rate of change of a field variable in a CV can be seen to be defined by the summation of all fluxes of the surrounding faces of the CV.

In order to achieve this, the governing equations of the flow in drift-flux model is written in a generic form

of transport equation for scalar or vector as follow (Brennan, 2001):

$$\frac{\partial \rho\phi}{\partial t} + \nabla \cdot \rho \mathbf{v}\phi - \nabla \cdot \rho \Gamma_\phi \nabla \phi = S_\phi(\phi) \tag{4.3}$$

Where the first term on LHS represents the temporal derivative, the second term on LHS represents the convection term, the third term on LHS represents the diffusion term, and the term on RHS represents the source term. The corresponding value of ϕ, Γ_ϕ, and $S_\phi(\phi)$ for each governing equations in drift-flux model are summarised in Table 4.1. Since FV method requires the governing equations to be satisfied over the Control Volume around its centre point, Equation 4.3 is written as follow. Consider a CV with a volume of V_P and centre point P:

$$\int_t^{t+\Delta t} \left[\int_{V_P} \left(\frac{\partial \rho\phi}{\partial t} \right) dV + \int_{V_P} \left(\nabla \cdot \rho \mathbf{v}\phi \right) dV - \int_{V_P} \left(\nabla \cdot \rho \Gamma_\phi \nabla \phi \right) dV \right] dt = \int_t^{t+\Delta t} \left[\int_{V_P} \left(S_\phi(\phi) \right) \right] dt \tag{4.4}$$

The discretisation of each term in Equation 4.4 is addressed in the following section.

Table 4.1: Assigned values of ϕ, Γ_ϕ, and S_ϕ for each governing equations of drift-flux model (Brennan, 2001)

Equation	ϕ	Γ_ϕ	S_ϕ
Mixt. Continuity	1	0	0
Mixt. Momentum	$\mathbf{v}_m$	μ_{eff}	$-\nabla P_m + \nabla \cdot \left[\mathbf{T} + \mathbf{T}^t - \sum_k \alpha_k \rho_k \mathbf{v}_{km} \mathbf{v}_{km} \right] + \rho_m \mathbf{g}$
Phase Transport	α_k	$\frac{\mu_t}{\sigma}$	$\nabla \Gamma_\phi \nabla \alpha_k$

Discretisation of Spatial Terms

There are two spatial terms that can be identified in Equation 4.4: the convective term, and the diffusive term. Each of these terms are discretised separately.

- **Convective Term Discretisation**

  Using Gauss' theorem and midpoint rule, the convective term is discretised as the summation of the mass-flux of all faces of the CV. Thus it is mathematically expressed as in Equation 4.5. Consider again a CV with a volume of V_P and centre point of P:

  $$\int_{V_P} \nabla \cdot (\rho \mathbf{v}\phi) \, dV = \sum_f F \phi_f \tag{4.5}$$

  Where subscript f denotes the cell faces, ϕ_f represents the value of ϕ at the cell-face, $\sum_f$ represents the summation over all faces of CV, and F represents the mass-flux through each face of CV. The mass-flux F is mathematically expressed as:

  $$F = \mathbf{S} \cdot \left(\rho \mathbf{v} \right)_f \tag{4.6}$$

  Equation 4.5 and 4.6 requires the calculations of face value of the variables ϕ and $\mathbf{v}$. This can be done by calculating from the values of the cell-centres, using a convection differencing scheme. In the framework of using arbitrary non-orthogonal mesh, the used cell-centre values should be limited only to the nearest neighboring CV due to a risk of storage overhead associated with the additional addressing information. Thus the relation between the value of face f, the CV centre value P, and the neighboring CV value E is illustrated in Figure 4.2. There are various differencing schemes available for Finite of Volume method, see Jasak (1996), Brennan (2001), and Goeree (2018). In this research, Gauss Linear and Gauss Gamma differencing schemes are used.

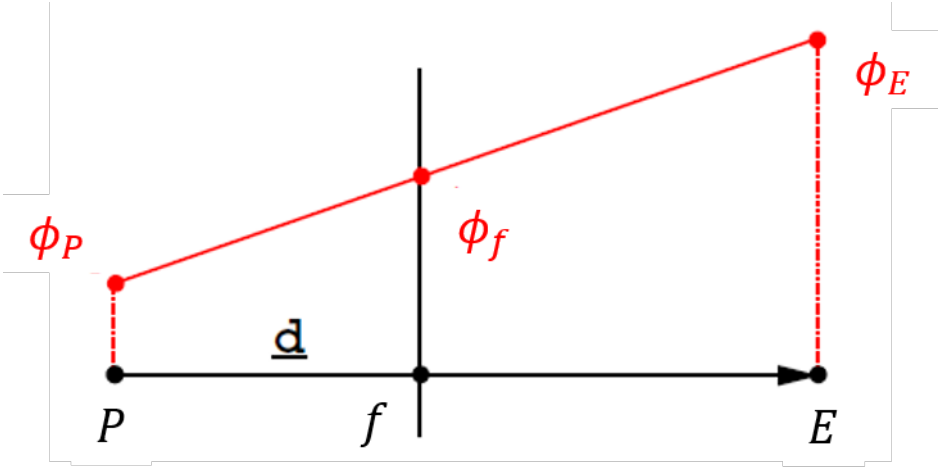

Figure 4.2: Illustration of face f, the value of ϕ_f, and its surrounding CVs (P and E)

In Gauss Linear differencing scheme, the variation of ϕ between centre point P and E is assumed to be linear, see Figure 4.2. Thus the face value ϕ_f can be calculated as:

$$\phi_f = f_x \phi_P + (1 - f_x)\phi_E \tag{4.7}$$

Where f_x is the interpolation factor, and calculated as the ratio of distances face f to neighboring centre E and CV centre P to neighboring centre E.

$$f_x = \frac{\overline{fE}}{\overline{PE}} \tag{4.8}$$

Gauss Linear differencing scheme is expected to give solution that is second-order accurate (Ferziger and Peric, 2012). Although its accuracy, Gauss Linear differencing could results in unphysical oscillations of the solution for convection-dominated flows (Jasak, 1996). Thus it could create unbounded solution.

Gamma differencing scheme is a High Resolution second-order differencing scheme (Jasak, 1996), based on Normalised Variable Diagram (NVD). This differencing scheme is specially developed for arbitrary non-orthogonal mesh. The algorithm of Gamma differencing scheme is described in Jasak (1996). Gamma differencing scheme is seen as the blending between Upwind Differencing scheme and Central Differencing scheme, and the blending is defined by a variable called blending factor (γ). For a good resolution of sharp profile, the blending factor is recommended to be defined as 0.1 (Jasak, 1996). Thus in this study, blending factor of 0.1 is assigned.

- **Diffusive Term Discretisation**

  The discretisation of diffusive term is done in a similar way as the discretisation of convective term. Firstly, the diffusive term is discretised using Gauss' theorem and midpoint rule as:

$$\int_{V_P} \nabla \cdot (\rho \Gamma_\phi \nabla \phi)\, dV = \sum_f \mathbf{S} \cdot (\rho \Gamma_\phi \nabla \phi) \tag{4.9}$$

  In the discretisation of diffusive term for non-orthogonal mesh, it is important to consider the vector representing the distance between centre point of the neighboring CVs (vector **d**) and also the normal

vector of the cell face (vector **S**), see Figure 4.3. When the mesh is orthogonal, vector **d** and **S** are parallel.

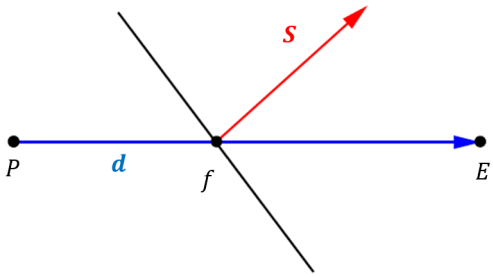

Figure 4.3: Vector **d** and **S** in a non-orthogonal mesh, adopted from (Jasak, 1996)

Thus, the value of gradient of ϕ at cell face can be assumed as a linear interpolation between both values at each cell centres, and calculated as follow:

$$\mathbf{S} \cdot \left(\nabla \phi\right)_f = |\mathbf{S}| \frac{\phi_E - \phi_P}{|\mathbf{d}|} \tag{4.10}$$

Using the interpolation factor, the face value is also calculated as follow:

$$(\nabla \phi)_f = f_x \left(\nabla \phi\right)_P + (1 - f_x) \left(\nabla \phi\right)_E \tag{4.11}$$

For non-orthogonal mesh, an adjustment needs to be done to Equation 4.10. The product of $\mathbf{S} \cdot (\nabla \phi)_f$ is splitted into two parts: a part representing the orthogonal contribution (first term RHS of Equation 4.12) and a part representing the non-orthogonal correction (second term RHS of Equation 4.12) (Jasak, 1996).

$$\mathbf{S} \cdot (\nabla \phi)_f = \Delta \cdot (\nabla \phi)_f + \mathbf{k} \cdot (\nabla \phi)_f \tag{4.12}$$

Where Δ and **k** are vectors decomposing vector **S** (see Figure 4.4) and should satisfy the following identity:

$$\mathbf{S} = \Delta + \mathbf{k} \tag{4.13}$$

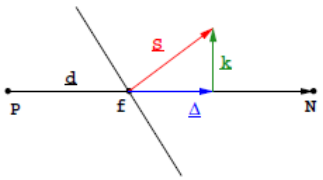

Figure 4.4: Illustration of vectors configuration for non-orthogonal mesh, using minimum correction method, as adopted from Jasak (1996)

There are several methods available for decomposing **S**, see Jasak (1996). In this research, minimum-correction method is used. The decomposition of vector **S** results in vector Δ which parallel with vector **d**. Thus Equation 4.10 can be directly used representing the orthogonal contribution in Equation 4.12. By implementing minimum-correction method, **S** is decomposed in such a way that the non-orthogonal correction is kept as low as possible. The non-orthogonal correction got a potential to create unboundedness, especially when the non-orthogonality degree of the mesh is high Jasak (1996). Thus when the priority of the simulation is to preserve stability and boundedness, the non-orthogonal correction should be limited as low as possible. This is done by making vector **k** and Δ perpendicular.

This condition is mathematically expressed as:

$$\Delta = \frac{\mathbf{d}\cdot\mathbf{S}}{\mathbf{d}\cdot\mathbf{d}}\mathbf{d} \tag{4.14}$$

Then $\mathbf{k}$ is calculated using Equation 4.13. Therefore the final form of the discretised diffusive term is as follow. Since $\mathbf{d}$ and Δ is kept in parallel, the orthogonal contribution is discretised as:

$$\Delta\cdot(\nabla\phi)_f = |\Delta|\frac{\phi_E-\phi_P}{|\mathbf{d}|} \tag{4.15}$$

Thus the discretised form of Equation 4.12 is:

$$\mathbf{S}\cdot(\nabla\phi)_f = |\Delta|\frac{\phi_E-\phi_P}{|\mathbf{d}|} + \mathbf{k}\cdot(\nabla\phi)_f \tag{4.16}$$

Where the face interpolate of $\nabla\phi$ is calculate using Equation 4.11.

Discretisation of Temporal Terms

In this research, to achieve the second-order requirement, Backward Differencing method is used, see Jasak (1996). The discretisation starts by considering Taylor expansion of ϕ in time. In Backward Differencing, three time levels are used. Thus the Taylor series is expanded to include two "old" time-level:

$$\phi(t-\Delta t) = \phi^{oo} = \phi^n - 2\frac{\partial\phi}{\partial t}\Delta t + 2\frac{\partial^2\phi}{\partial t^2}\Delta t^2 + O(\Delta t^3) \tag{4.17}$$

Where $\phi^n = \phi(t+\Delta t)$, and $\phi^o = \phi(t)$. Therefore, the second-order approximation of the temporal derivative is:

$$\frac{\partial\phi}{\partial t} = \frac{3/2\phi^n - 2\phi^o + 1/2\phi^{oo}}{\Delta t} \tag{4.18}$$

Therefore the final form of the discretised transport equation is:

$$\frac{3/2\phi^n - 2\phi^o + 1/2\phi^{oo}}{\Delta t}V_P + \sum_f F\phi_f - \sum_f(\rho\Gamma_\phi)_f\mathbf{S}\cdot(\nabla\phi)_f = SuV_P + SpV_P\phi_P^n \tag{4.19}$$

4.2. Numerical Solution and Algorithm Controls

4.2.1. Pressure Poisson Equation Solver

In Finite of Volume method, the pressure field values are solved using pressure Poisson Equation (see Jasak (1996), Moukalled et al. (2016), and Goeree (2018) for the derivations). To solve the pressure Poisson equation numerically, a solver is required. In this research, Multi-grid method is used in this research (in OpenFOAM: *GAMG* solver). In Multi-grid method, the pressure Poisson equation is solved using multiple cells on coarse level of the domain, using Jacobi relaxation method. Then the solution obtained from the coarse levels are mapped to the finer cells, until finally mapped to the finest cells. This procedure is repeated several times until the solution reaches convergence. The convergence are defined when one of the following conditions are fulfiled:

- The residual falls below the assigned tolerance.
- The ratio of current to initial residual falls below the assigned relative tolerance.
- The number of iteration exceeds the assigned maximum number of iterations.

In this research, for solving the pressure Poisson equation, the assigned tolerance is $1 \cdot 10^{-9}$, with relative tolerance of 0.01. The coarse level is assigned to include 10 cells. The number ofiteration of this solver is based on the number of corrector iterations in the pressure-velocity coupling algorithm. Since the velocity field affects the resulting pressure field and vice versa, the pressure and velocity needs to be coupled. This is addressed in the following section.

4.2.2. Pressure-Velocity Coupling

To solve the Navier-Stokes equations for the incompressible flows, the pressure and velocity needs to be coupled. In this research, PIMPLE algorithm is used, which is ainly used for transient cases. PIMPLE algorithm is a variation of PISO (Pressure Implicit with Splitting of Operator) algorithm and SIMPLE (Semi-Implicit Method for Pressure-Linked Equations) (Robertson et al., 2015). The flowchart of PIMPLE algorithm is illustrated in Figure 4.5.

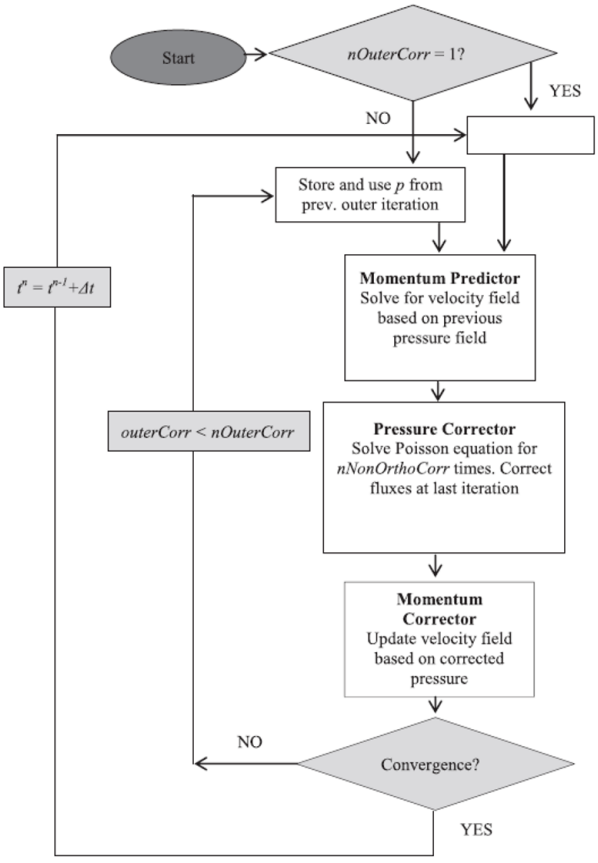

Figure 4.5: Flowchart of PIMPLE algorithm (Robertson et al., 2015)

In PIMPLE algorithm, there are variables to be defined: outer correctors, inner correctors, relaxation factors, and tolerance. The number of outer correctors defines how many system of equations are performed beforer the simulation is forced to move onto the next timestep, regardless of whether that timestep has reached convergence or not. The criteria of timestep convergence is defined as the absolute tolerance of the solver. In this research, the number of outer corrector is defined as 100, with the absolute tolerance of $1 \cdot 10^{-5}$.

The number of inner correctors is the number of times the algorithm solves the pressure eqeuation and momentum corrector in each timestep. The suggested value of inner corrector is 1 - 3 (Greenshields, 2015). In this research, the number of inner correctors is defined as 2.

Under-relaxation, a technique used for improving the stability of the computation, is used in this study. Under-relaxation works by limiting the amount which a variable changes from one iteration to the next iteration. In this study, the value of relaxation factors of 0.1 is used for the pressure, and 0.7 for the velocity.

4.2.3. Solution Procedure for Navier-Stokes System

As the discretisation and the solution solvers already defined, it is now possible to describe the algorithm for solving the Navier-Stokes equations. For solving a transient incompressible flows, the algorithms are as follow (Jasak, 1996):

1. Setup the initial and boundary conditions for all field values.
2. Start the calculation of the new timestep of the field values.
3. Go through PIMPLE algorithm until the conergence is reachd. In this stage, the pressure and velocity fields for current timestep are obtained, as well as the new set of conservative fluxes.
4. Using these conservative fluxes, solve all equations in the system.
5. If the final timestep is not yet reached, return to step 2.

The assigned setting of numerical solution and algorithm controls in this study is summarised in Table 4.2.

Table 4.2: Setting of numerical solution and algorithm controls in this study

Pressure Poisson solver: Multi-Grid (GAMG)	
Number of cells in coarse level	10
Pressure-velocity coupling: PIMPLE	
Outer correctors	100
Inner correctors	2
Non-orthogonal correctors	2
Residual (Pressure):	
(1). Tolerance	(1). $5 \cdot 10^{-4}$
(2). Absolute tolerance	(2). 0
Residual (Velocity)	
(1). Tolerance	(1). $1 \cdot 10^{-5}$
(2). Absolute tolerance	(2). 0
Under-relaxation factor:	
Pressure	0.1
Velocity	0.7

5

Model and Simulation Setup

In numerically simulating flow in computational fluid dynamics, things need to be set up before conducting one simulation: domain of the simulation and also the setting in OpenFOAM. These are addressed in this chapter. The chapter starts by describing the domain used in the simulation, and the preliminary study was done regarding the simulation domain. Then the chapter continues with the setup done in OpenFOAM, including the algorithm setting and transport properties of the simulated flow, such as the mixture density, volumetric concentration, and inlet condition. This chapter also addresses the decomposition method of the domain in order to do parallel simulation the flow.

5.1. Simulation Cases Setup

In this research, six cases are prepared to be simulated. The cases are summarised in Table 5.1. These cases are prepared following one of the laboratory experiment case of Byishimo (2018). In observing the implementation of the arbitrary non-orthogonal mesh, two parameters are varied throughout the prepared cases: solids settling condition and differentiation scheme. Since the simulated tailings use monosize solids fraction assumption, three solids settling conditions are prepared, named "minimum," "extreme," and "realistic" solids settling conditions.

In cases using the "minimum solids settling" condition, the assigned terminal settling velocity of the solids fraction within the tailings mixture is 0, thus creating as well 0 hindered settling velocity. Therefore the settling of the tailings mixture is assumed to be affected only by the gravitational body force of the tailings as a continuum fluid, not by the relative velocity between both fluids in the system. In the Table 5.1, these cases are represented by Case 1 (both A and B).

In cases using "extreme solids settling" condition, the settling of the tailings mixture is assumed due to a high settling velocity of the solids particle within the tailings mixture. For creating such of condition, the tailings mixture is assumed to be filled by monosize particles with a diameter of $95 \cdot 10^{-6} m$. The resulting terminal settling velocity of this particle diameter is $6.878 \cdot 10^{-3} m/s$. In these cases, we can see the extreme effect of implementing solids settling in drift-flux method. These cases are represented by Case 2 (both A and B).

"Realistic solids settling" condition should give the simulation results closer to the laboratory experiment

results. In these cases, the tailings mixture is assumed to be filled by monosize particle with a diameter of $45 \cdot 10^{-6} m$, which is the d_{50} of the mixture used in the laboratory experiment of Byishimo (2018). By using this diameter, the expected settling velocity of the solid particle is $1.487 \cdot 10^{-3} m/s$, approximately six times less than the cases with "extreme solids settling" condition. These cases are represented by Case 3 (both A and B).

In these cases as well, the effect of two differencing schemes are observed. These differencing schemes are Gauss Gamma differencing scheme and Gauss Linear differencing scheme. Cases with Gauss Gamma differencing scheme are represented by alphabetic A, while cases with Gauss Linear differencing scheme are represented by alphabetic B.

All cases are simulating a discharging tailings mixture with initial velocity of $0.71 m/s$. The discharged tailings has a density of $1011.5 kg/m^3$. These mixture density represents a mixture with solids concentration of $20 g/l$, or equal to 0.0005 solids volumetric concentration. The ambient water density is assigned as $1000 kg/m^3$.

Table 5.1: Setup of the simulation cases

Cases	**1A**	**1B**	**2A**	**2B**	**3A**	**3B**
Description	"Minimum solids settling" cases		"Extreme solids settling" cases		"Realistic solids settling" cases	
Discharging jet-velocity $[m/s]$	0.710	0.710	0.710	0.710	0.710	0.710
Mixt. Density (ρ_m) (kg/m^3)	1011.5	1011.5	1011.5	1011.5	1011.5	1011.5
Water Density (ρ_w) (kg/m^3)	1000	1000	1000	1000	1000	1000
Solid-fraction density (ρ_s) (kg/m^3)	2650	2650	2650	2650	2650	2650
initial SSC $[g/l]$	20	20	20	20	20	20
α_s	0.0005	0.0005	0.0005	0.0005	0.0005	0.0005
Particle diameter $[m]$	-	-	$95 \cdot 10^{-6}$	$95 \cdot 10^{-6}$	$45 \cdot 10^{-6}$	$45 \cdot 10^{-6}$
$\mathbf{v}_{ts}$ **[m/s]**	-	-	$6.878 \cdot 10^{-3}$	$6.878 \cdot 10^{-3}$	$1.487 \cdot 10^{-3}$	$1.487 \cdot 10^{-3}$
Differentiation Scheme	Gauss Gamma	Gauss Linear	Gauss Gamma	Gauss Linear	Gauss Gamma	Gauss Linear

5.2. Geometries of Simulation Domain

In this research, the simulation domain is following a tank geometry with a round pipe as the inlet of the tailings mixture, adopted from the laboratory experiments of Byishimo (2018). The construction of the simulation domain and mesh are done with assistance and help from Frans van Grunsven. These geometries, mesh construction, and geometries adaptation are discussed in this section.

The domain geometry is constructed as a modular tank with dimensions as described in Table 5.2 and illustrated in Figure 5.1. This setup is picked as it showed no sediment deposition-ring during the laboratory experiment done by Byishimo (2018), which needs to be avoided as it would lead to numerical complexity. This tank was constructed to mimic a deep-sea field condition, with a scale of 1:50. An artificial seabed is implemented by placing a table at the bottom of the tank to create a gap between the observed flow and the tank walls. Therefore the interaction between tank walls and the flow can be minimized. A round pipe is located 1m above the tabletop, with a diameter of 0.01m. This round pipe is assigned as the source of the tailings discharge.

Table 5.2: Dimensions of the simulation domain, following the laboratory setup of Byishimo (2018)

	Prototype	Field	Unit
Tank:			
Length	5	255	$[m]$
Width	2.25	113	$[m]$
Height	2	105	$[m]$
Table:			
Length	4.5	225	$[m]$
Width	1.75	98	$[m]$
Height	1	50	$[m]$
Round pipe:			
Diameter	0.01	0.5	$[m]$
Height (from table surface)	1	50	$[m]$

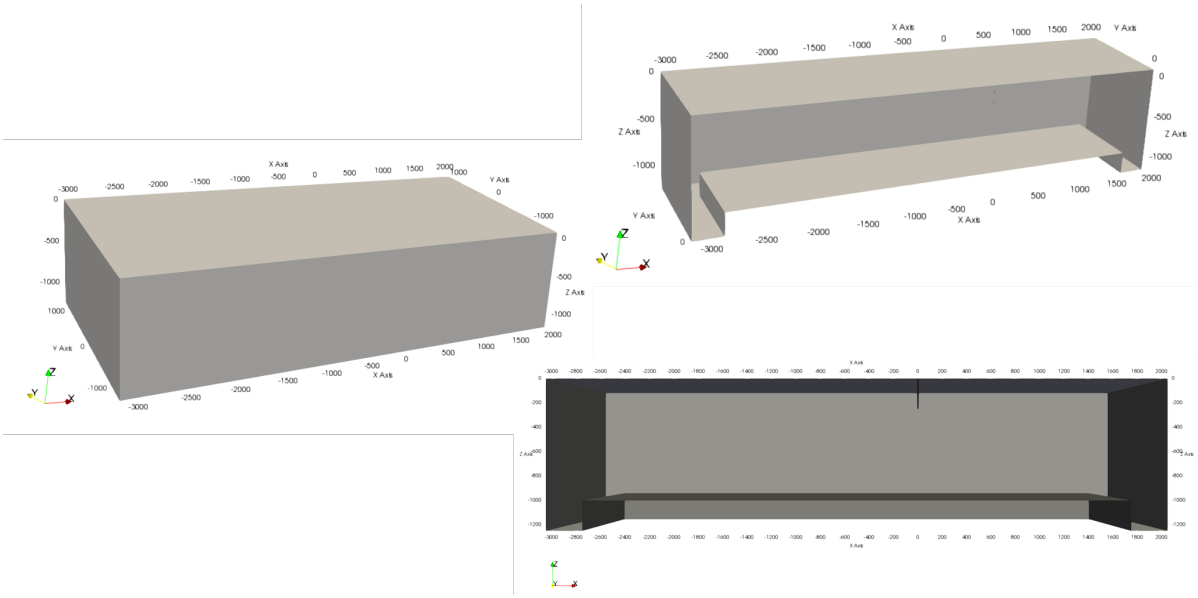

Figure 5.1: Geometries of the simulation domain

5.2.1. Mesh Construction

The construction of the mesh in the original domain is illustrated in Figure 5.2. In this study, the mesh construction is done with help by Ir. Frans van Grunsven. In the original domain, the mesh is constructed to be filled by 5,255,692 cells in total. Refinement is done in the inlet pipe, near the pipe-end, and the area where main jetstream expected to occur. For achieving the required resolution as in the laboratory measurement and also resolving the turbulent boundary layer, cell layers are constructed near the tabletop and also at the inlet pipe walls, where the resulting y^+ value should be 12. Coarser cells are constructed at the area further from the inlet and tabletop.

5.3. Preliminary Study: Original Domain

A preliminary study is then done to ensure whether the constructed domain should be able to simulate the wanted physics and flow. This is done by simulating one of the prepared cases for a short simulation time and

then checking the numerical performance of the simulation. In this study, the preliminary simulation is done using Case 1A and 2A. During the simulations, the used timestep is assigned to be adjustable, based on the maximum allowable Courant number. This is done to see the maximum allowable timestep when simulating using this domain. As can be seen in Table 5.3, the obtained timestep when using maximum Courant number of 0.9 is $3 \cdot 10^{-5}$s. Hence the simulation can only run until 0.1691s for a realtime of 18 hours.

Consequently, using this domain, running 1-minute of simulation time would require 6386 hours of realtime. This is equal to approximately 266 days and considered not feasible due to the time restriction of the research. Therefore an adjustment needs to be done to the simulation domain. This is addressed in the following section.

Table 5.3: Numerical performance using original domain

	Case 1A	**Case 2A**
Max. allowable Co [-]	0.9	0.9
Obtained timestep [s]	$3 \cdot 10^{-5}$	$3 \cdot 10^{-5}$
Obtained simulation time [s]	0.1691	0.079
Realtime [hours]	18	18

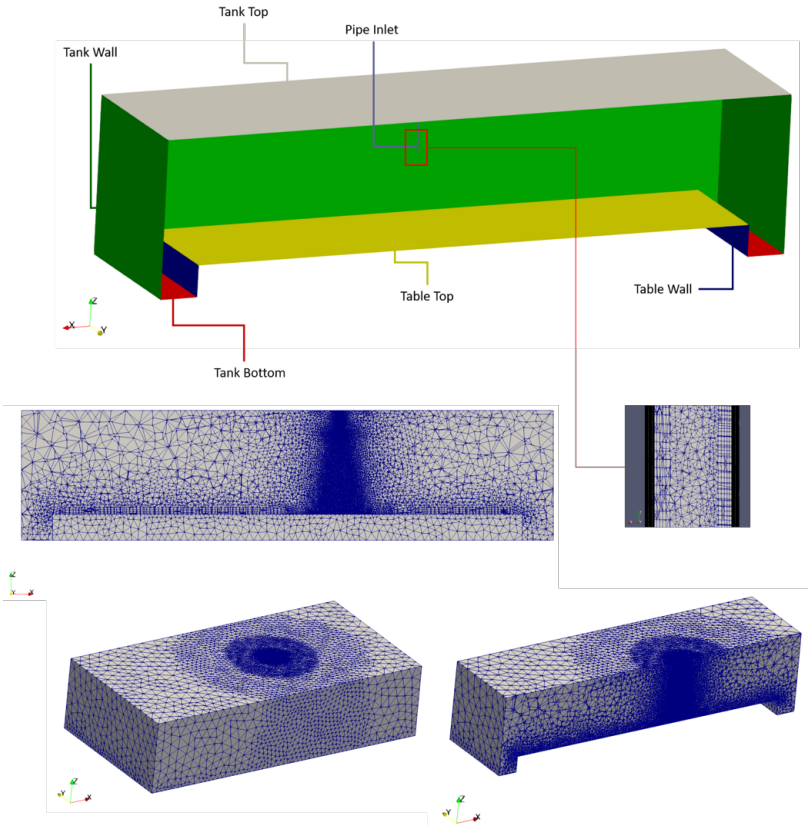

Figure 5.2: Boundaries of the original domain and its mesh construction

5.4. Domain Readjustment: Cutting Off The Domain

As described in the preliminary study, it is not feasible to simulate for the prepared cases using the original domain due to the extensive simulation time and lack of necessary computational performance. Thus the simulation domain is reconstructed in this research. The reconstruction is done by cutting off the domain vertically, getting rid of half of the domain in the vertical direction, which requires very fine mesh (especially for the constructed mesh around the discharging pipe). The resulting cutoff domain is illustrated in Figure 5.3. The resulting domain dimensions are summarised in Table 5.4.

Table 5.4: Comparison between the dimensions of the original domain and the reconstructed cutoff domain

	Original domain	Cutoff domain	Unit
Tank:			
Length	5	5	$[m]$
Width	2.25	2.25	$[m]$
Height	2	1.5	$[m]$
Table:			
Length	4.5	4.5	$[m]$
Width	1.75	1.75	$[m]$
Height	1	1	$[m]$
Round pipe:			
Diameter	0.01	-	$[m]$
Height (from table surface)	1	-	$[m]$

By implementing this domain reconstruction, an adaptation needs to be done as well to the inlet boundary of the domain. In the original domain, the inlet is assigned as a pipe. This inlet pipe is replaced by an inlet patch using buoyant-jet theory in the new domain, as described in Chapter 2. The steps for readjusting the inlet condition are as follow:

1. Determine the initial parameters of the momentum and buoyancy flux of the buoyant-jet.
2. Determine the transition length-scale of the buoyant-jet from behaving jet-like to plume-like.
3. Determine the properties of the develope jet or plume at the desired distance of the new inlet patch.

First, the length-scale (l_s) of which the jet-plume transition occurs is calculated. To calculate this, the mass, momentum, and buoyancy fluxes of the original buoyant-jet are calculated. Using Equation 2.1, 2.2, and 2.3, and also the original condition of the buoyant-jet source ($D = 0.01m$, $\mathbf{v}_o = 0.71m/s$), the mass, momentum, and buoyancy fluxes of the buoyant-jet are obtained as follow:

$$Q_o = 5.6 \cdot 10^{-5} m^3/s$$

$$M_o = 3.93 \cdot 10^{-5} m^4/s^2$$
$$g' = 0.1128 m/s^2$$
$$F_o = 6.3 \cdot 10^{-6} m^4/s^3$$

The length-scale is then calculated using above values and Equation 2.8, which is approximately $0.2m$. Thus the buoyant-jet can be considered to behave as a pure jet at a vertical distance below $0.2m$ from the discharging source ($z < 0.2m$). On the other hand, it is considered as a pure plume at a vertical distance five times the

length-scale ($z = 1m$) (Lee and Chu, 2012). Hence at vertical distance z of 0.5m from the discharging source, the buoyant-jet is considered to be in a transition regime. The contribution for each pure-jet and pure-plume needs to be determined first for calculating the flow condition at a transition regime.

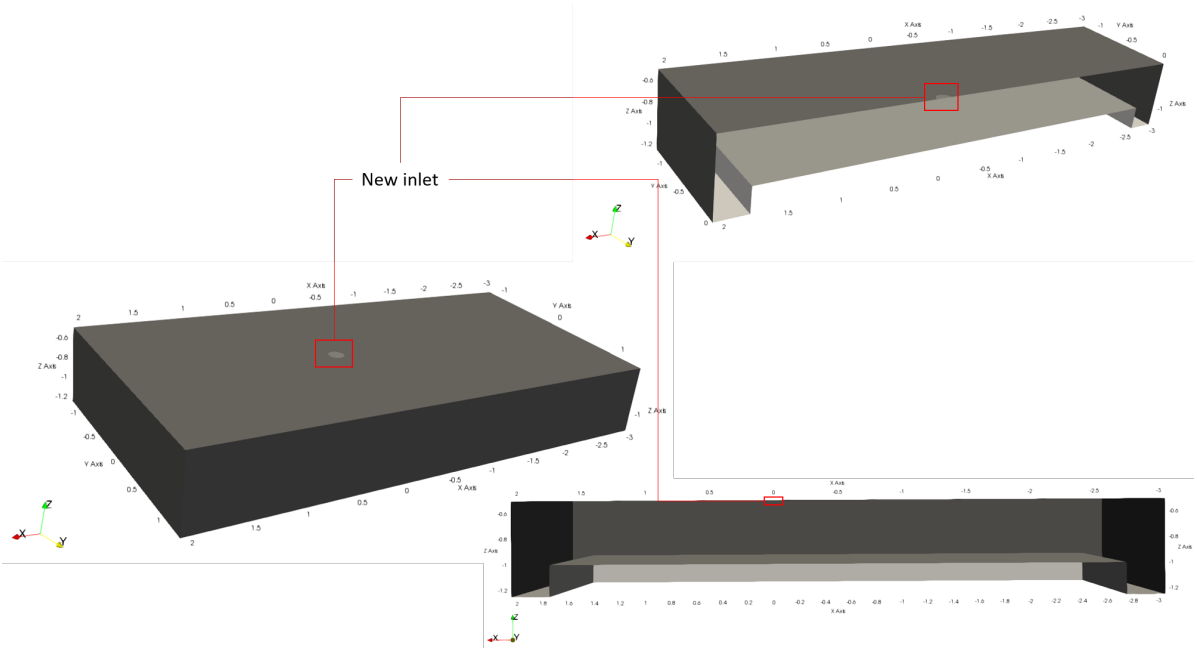

Figure 5.3: The new reconstructed simulation domain

For a pure round-jet originating from a nozzle with a certain diameter D and initial velocity $\mathbf{v}_o$, the jet width b_j, centerline velocity $\mathbf{v}_{max,j}$ and its average dilution $\bar{\mathbf{S}}_j$ can be calculated using the following equations (Lee and Chu, 2012):

$$b_j = 0.114z \tag{5.1}$$

$$\mathbf{v}_{max,j} = 7 \cdot M_o^{1/2} z^{-1} \tag{5.2}$$

$$\bar{S} = 0.32 \frac{z}{D} \tag{5.3}$$

Then assigning a value of z of $0.5m$ and pipe diameter D of $0.1m$, the obtained jet-width b_j, centerline velocity $\mathbf{v}_{max,j}$, and average dilution $\bar{S}_j$ are:

$$b_j = 0.06m$$
$$\mathbf{v}_{max,j} = 0.088m/s$$
$$\bar{S} = 16$$

For a pure plume, the plume-width b_p, centerline velocity $\mathbf{v}_{max,p}$, and average dilution $\mathbf{S}_p$ are calculated using the following equations (Lee and Chu, 2012):

$$b_p = 0.105z \tag{5.4}$$

$$\mathbf{v}_{max,p} = 4.7 \cdot F_o^{1/3} \cdot z^{-1/3} \tag{5.5}$$

$$\bar{S}_p = 0.163 \cdot F_o^{1/3} \cdot z^{5/3} \cdot Q_o^{-1} \tag{5.6}$$

Again using the value of z of $0.5m$ and pipe diameter of $0.1m$, the calculated plume width, centerline velocity,

and average dilution are:

$$b_p = 0.053m$$
$$\mathbf{v}_{max,p} = 0.109m/s$$
$$\bar{S}_p = 17$$

Then linear interpolation is assumed for calculating the values at the distance z of $0.5m$ from the discharging pipe. Hence, the obtained conditions at vertical distance of $0.5m$ are:

$$b_p = 0.056m$$
$$\mathbf{v}_{max,p} = 0.096m/s$$
$$\bar{S}_p = 16.4$$

The above-obtained conditions are the Gaussian profile of the inlet at the distance of 0.5m. Although the required Gaussian profile for the inlet patch is obtained already, its implementation requires further computational skills. To overcome this, top-hat approximation is implemented to the obtained inlet condition in this research. Using Equation in Chapter 2 for top-hat approximation, the resulting inlet conditions are as follow:

$$B = 0.078m$$
$$\mathbf{v}_{max} = 0.048m/s$$
$$\bar{c} = 1.22g/L$$
$$\alpha_s = 0.0005$$

These are the implemented inlet condition representing the new buoyant-jet inlet patch.

5.4.1. Mesh Construction

As in the original domain, an arbitrary non-orthogonal mesh is also implemented in the new simulation domain. The mesh construction is also in assistance and help of Ir. Frans van Grunsven. Cell sizes are varying, with a total of 3,014,508 numbers of cells. The advantages of arbitrary, non-orthogonal mesh are the ability to construct finer cells (CV) on the area where the expected main flow stream to occur. The coarser cells are then constructed in the area, which less detailed of the flows needed. A proper gradient profile of the cell sizes is still required to prevent high hydraulic jumps due to the drastic velocity change between cells. The construction of the mesh for this domain can be seen in Figure **??**. The summary of the mesh construction is summarised in Table 5.5.

To achieve the proper simulation result, care to the construction of the domain mesh is needed, especially in the area where high velocities, high velocity-gradient, and shear layer are expected to occur. The inability to properly estimate a proper cell size would lead to instability of the simulation. In this research, the maximum cell-size on the mentioned areas is calculated based on the maximum allowable Courant number of the simulation. Courant number is a variable which is assigned as the stability requirement of the simulation and is defined as:

$$Co = \frac{\mathbf{v}\Delta t}{\Delta x} \tag{5.7}$$

Where Δt is the simulation timestep, $\mathbf{v}$ is the expected maximum flow-velocity, and Δx is the maximum cell size. To ensure stability is sustained throughout the simulation, the allowable maximum Courant number should not be bigger than 1. Moreover, to further ensure the stability, the picked maximum Courant number in this research is 0.5. Using an expected maximum flow velocity of $0.109m/s$ or approximately $0.11m/s$, and Δt of $8 \cdot 10^{-3}$ s, the maximum cell size is:

$$\Delta x = \frac{\mathbf{v} \cdot \Delta t}{Co}$$
$$\Delta x = 0.0018m \approx 0.002m$$

Therefore the maximum allowed cell size is approximately $0.002m$. Besides the non-orthogonal mesh, cell layers are also constructed near the tabletop. The construction of the cell layers is following the required resolution to be compared to the laboratory measurement data. Although the accuracy priority, the cell layers should be constructed so the computational time still within the limit. Thus the constructed cell layers are as summarised in Table 5.6, where the constructed cell layers should fulfill y^+ of 12, as in the original mesh construction. These cell layers contain 15 layers to create an acceptable transition from the plume to the tabletop. The first cell layer size is $1mm$ which follows the resolution of the laboratory measurement. For the next cell layer, the cell size is increasing by 10 percent. Thus the next cell-layer size is $1.1mm$. This construction creates cell layers with accumulative height of $31.8mm$. The simulated flow is expected to reach its maximum magnitude at the height of $10mm$ from the tabletop. Therefore the assigned cell layer at this height is around $2mm$, which is the requirement from the calculation using Courant number above.

Table 5.5: Mesh construction of the simulation domain

Number of CVs (cells) [-]	3,014,508
Non-orthogonality degree [o]**:** **(a) Average** **(b) Maximum**	(a) 14.67^o (b) 81.27^o
CV face: **(a) minimum area** [m^2] **(b) maximum area** [m^2]	(a) $1.64 \cdot 10^{-6} m^2$ (b) $0.00803 m^2$

Table 5.6: Layers implementation on top of the tabletop boundary

Layer (from tabletop)	Cell size [mm]	Accumulative layers height (mm)
1	1	1
2	1.1	2.1
3	1.2	3.3
4	1.3	4.6
5	1.5	6.1
6	1.6	7.7
7	1.8	9.5
8	1.9	11.4
9	2.1	13.6
10	2.4	15.9
11	2.6	18.5
12	2.9	21.4
13	3.1	24.5
14	3.5	28.0
15	3.8	31.8

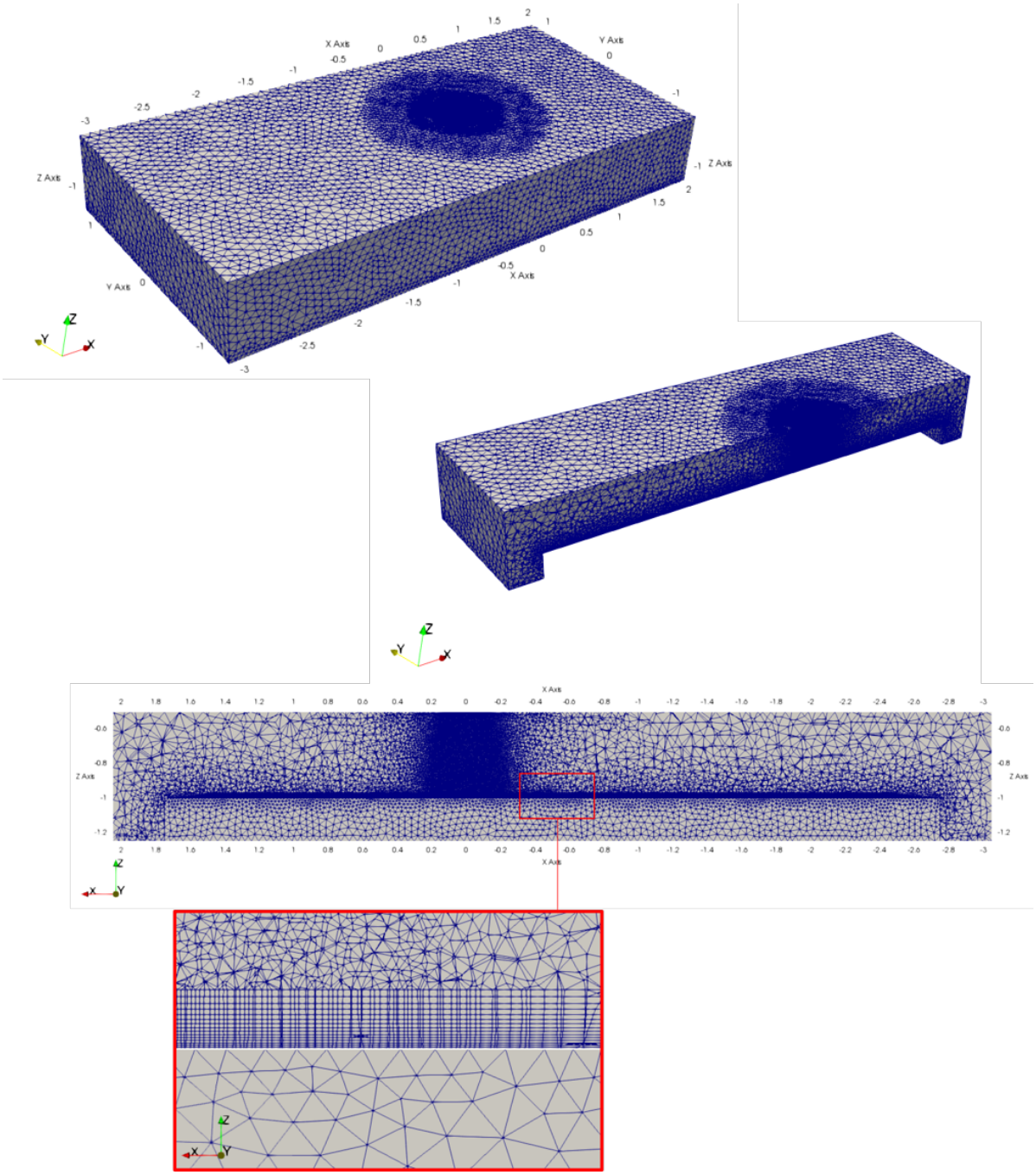

Figure 5.4: Mesh construction of the reconstructed domain, and the cell layers implemented in the area near tabletop boundary

5.4.2. Boundary Conditions

As in the original domain, boundary conditions of the field variables should also be defined. For this research, the boundary conditions for the following field variables must be specified: velocity, the volumetric concentration of each phase, and pressure. The boundaries of the simulation domain are illustrated in Figure 5.5. The assigned boundary conditions are summarised in Table 5.7.

Table 5.7: Boundaries conditions of the simulation field variables

Boundary	U (velocity)	α_{solid}	α_{water}	P
Tank Top	Inlet-Outlet	Inlet-Outlet	Inlet-Outlet	Fixed value of 0
Tank Wall	Wall (no slip)	Zero gradient	Zero gradient	Zero gradient
Tank Bottom	Wall (no slip)	Zero gradient	Zero gradient	Zero gradient
Jet Inlet	Fixed value of $0.048 m/s$	Fixed value	Fixed value	Zero gradient
Table Top	Wall (no slip)	Zero gradient	Zero gradient	Zero gradient
Table Wall	Wall (no slip)	Zero gradient	Zero gradient	Zero gradient

For velocity, the following conditions apply. At the inlet and top of the tank, the velocity is specified. For the other boundaries, the no-slip condition is implemented. This means that it is assumed that the fluid is attached to the wall. As the walls are not moving, a velocity of zero in all directions is then implemented. At the inlet boundary, a fixed inlet velocity of $0.048 m/s$, as calculated from the previous section is implemented. At tank-top boundary, inlet-outlet condition is applied. This means that the fluids can flow out of the domain from this boundary to preserve the continuity within the domain, and when specified, inlet of the fluid with a certain velocity can also occur as well through this boundary.

The pressure is zero-gradient boundary condition everywhere except the tank-top boundary. In this boundary, the pressure is assigned as a fixed value of 0.

For the volumetric concentration of both tailings and water phases, zero-gradient conditions are implemented in all boundaries except the tank-top and inlet boundary. Since the simulated cases assume a constant inlet of tailings mixture with a constant volumetric concentration, the inlet boundary condition of volumetric concentrations is thus assigned as a fixed value. At the tan-top boundary, inlet-outlet condition is imposed for both phases volumetric concentration.

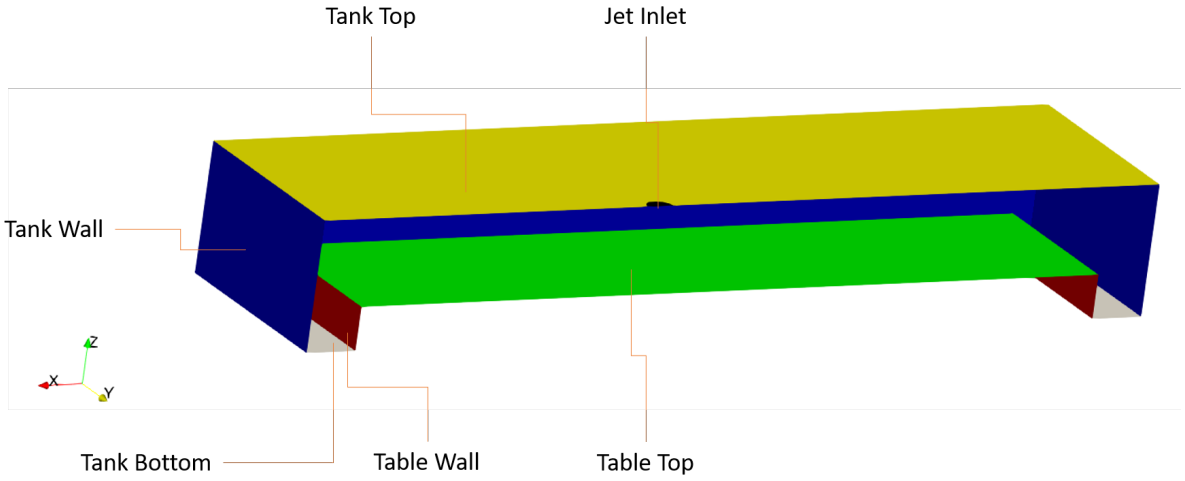

Figure 5.5: Boundaries of the reconstructed domain

5.5. Decomposition Method

In this research, the simulation runs in parallel using the Reynolds cluster. To simulate in parallel, the domain is decomposed into parts which each part will be run by one core. The domain is decomposed using cylindrical decomposition method, where the doamin can be decomposed in axial, radial, and azimuthal directions. In this research, the domain is decomposed in azimuthal direction, where the coordinate of the inlet patch is picked as the origin point of the decomposition. This decomposition is illustrated in Figure 5.6.

Before running the full simulation, the performance of the decomposition is observed first to analyze the optimal number of core for running the simulation. To observe this, the simulation using the reconstructed domain is run for one hour (3600 seconds), and then the simulated time and resulting maximum Courant number are compared for each decomposition case. This decomposition observation is summarised in Table 5.8. As the decomposition number becomes higher, the simulated time becomes longer for the same amount of real-time. Hence, the domain is then decomposed into twenty-seven (27) parts, following the maximum allowable core to be used in Reynolds cluster. By decomposing the domain into 27 parts, each core now only needs to simulate 111649 CVs. Moreover 27 cores also observed to result in the longest simulated time for the same period of realtime, as summarised in Table 5.8.

Table 5.8: Observation of the decomposition performance

Decomposing Cases (Radial, Azimuthal, Axial)	**RealTime [s]**	**Simulated Time [s]**	**Max. Courant number**
No decomposing	3600	0.027022	0.48182
(1 3 1)	3600	0.10956	0.5035
(1 4 1)	3600	0.157833	0.50688
(1 8 1)	3600	0.215431	0.516277
(1 16 1)	3600	0.222639	0.527
(1 20 1)	3600	0.222639	0.527
(1 27 1)	3600	0.222983	0.511

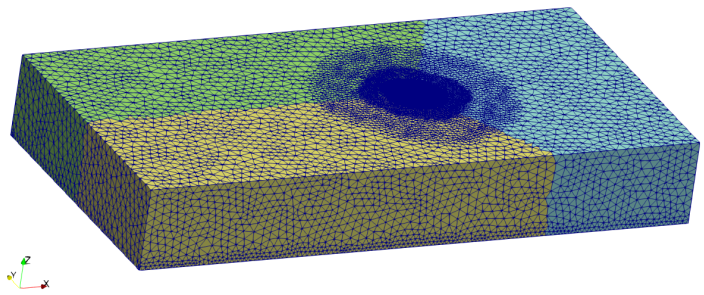

Figure 5.6: Illustration of domain decomposition of the reconstructed domain using radial decomposition-method with Axial, Azymuth, and Radial values of 1, 3, 1

6

Simulation Cases and Results

In this chapter, the simulation results with reconstructed domain are presented. Before the simulation results are presented, validation method of the simulation is described first.

6.1. Validation Method

For validating the simulation, the simulated field variables are compared to the laboratory measurement done by Byishimo (2018). In this section, the methodology of the laboratory measurement is briefly explained. For more detailed explanations and descriptions regarding the laboratory measurements, see Byishimo (2018).

In this research, the validated variables are the simulated flow velocities and Suspended Solid Concentration (SSC). In the laboratory experiments, the measurements were done in 8 points on the tabletop, with nine vertical heights for each point (see Figure 6.1). The measurements of these flow velocities and SSC were done as the tailings flow reached steady-state. To measure the flow velocity, each vertical elevation for each measurement point was measured for 60 seconds using a sensor at 15 Hz frequency. Thus the sensor obtains 1000 samples per each height of measurement point for every minute. Then the samples were averaged for sixty seconds to obtain the time-averaged velocity at each vertical elevation z. By using this method, at least 48 data are available for each measurement point, consisting of both lateral and axial flow velocities. For SSC, the measurement was done using direct turbidity measurement of local, near-bed SSC. Valves were installed on the tabletop, which can be opened for collecting the fluids near the tabletop. After the experiment started and reached steady-state, tube's end valves were opened for 30 seconds to flush the tube clean. Then 100 ml samples were taken at each measurement point. It was noticed during the measurement that water from a column of about 20mm above the measurement point was sucked as well into the tubes. Hence the measured SSC turned out giving the value of 20-mm averaged SSC (local-averaged SSC).

In summary, the available laboratory data for validation are 60-seconds averaged flow velocities for each vertical height of each measurement point, and 20-mm local-averaged SSC of each measurement points. These data are obtained by taking a 60-seconds measurement after the tailings flow reached steady-state. Then, the measurement data are compared to the simulation data to get insight on how the results of each simulation cases representing the actual flow phenomena.

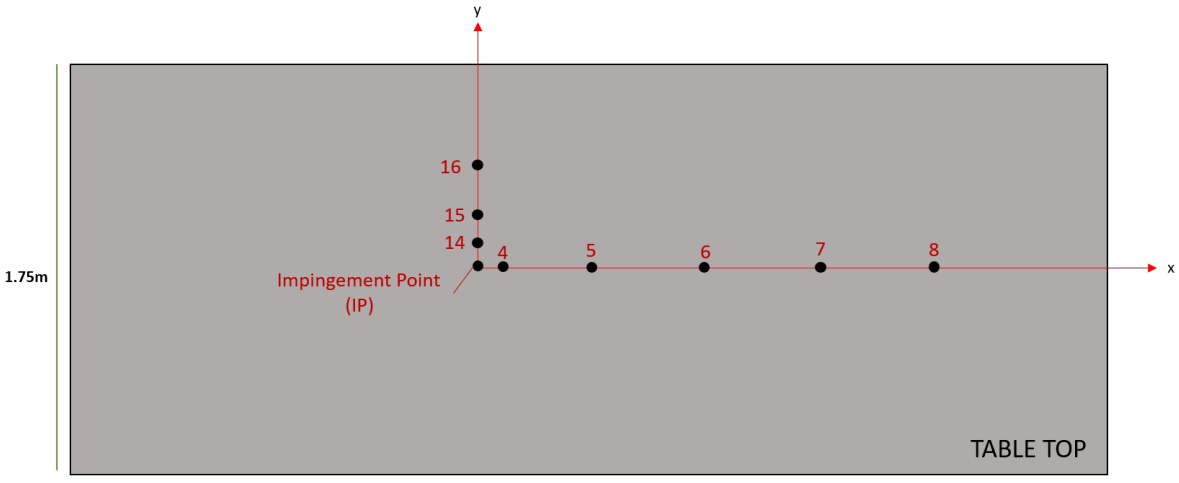

Measurement Points	P4	P5	P6	P7	P8	P14	P15	P16
x-distance from IP [m]	0.1	0.5	1.0	1.5	2.0	0	0	0
y-distance from IP [m]	0	0	0	0	0	0.1	0.25	0.5

Measured z-axis (from table top)[mm]	1; 3; 5; 7; 9; 10; 15; 20; 25; 30; 35; 40; 50; 60;

Figure 6.1: Measurement points, its coordinates from the Impingement Point (IP), and the measured vertical distances from the table top

6.2. Simulation Results

6.2.1. Numerical Performance

In this research, the simulation is done using fixed timestep of $2.5 \cdot 10^{-3}\ s$. Using this timestep, the simulation runs with maximum Courant number of around 0.3, and the mean Courant number around $4 \cdot 10^{-4}$. Hence the assigned timestep should fulfill the stability requirement. By using this timestep, each timestep should take around realtime of 7 - 10 seconds. Consequently, running a 1-minute simulation requires realtime of approximately $162.942s \approx 45.3$ hours. This numerical performance is summarised in Table 6.1.

Table 6.1: Numerical performance of the simulations using the constructed grids, domains, and boundary conditions

Δt **[s]**	$2.5 \cdot 10^{-3} s$
Resulting max. Co [-]	0.3
Average Co. [-]	$4 \cdot 10^{-4} s$
Real-time per time-step [s]	$7 - 10$
Required real-time for $60s$ **simulation time [s]**	$162,942s \approx 45.3 hours$

6.2.2. Steady-State Identification

As stated in the validation method, the simulation should be ensured to reach a steady-state condition first before being validated. The steady-state condition is identified by calculating 1-minute averaged of simulated flow velocities for every one minute simulation time, at each designated measurement points.

It is observed that the flow does not reach steady-state conditions at the same time due to the various distance of each measurement point. After running the simulations for around 9 minutes of simulation time, only measurement points 4, 5, 6, 14, 15, and 16 that are seen to approximately reach steady-state condition

(see Figure 6.2, 6.3, 6.4, 6.5, and 6.6). For reaching steady-state at points 7 and 8 would require longer computational time, which is restricted due to the time limit of the research project. Hence, it is decided that the observation and validation are done for Point 4, 5, 6, 14, 15, and 16 only. The validation is then done for each simulated case at these measurement points.

After the simulation is finished, the simulated field variables are plotted spatially. Hence the spatial spreading and variation of the field variables can be observed. The domain is then cut halfwidth when observing the spatial plot to observe the area near the mainstream of the tailings jet. Since the tailings mixture is expected to spread radially after impingement, the observation between spatial plotting at the x-axis and y-axis as the normal axis should give similar results. As mentioned in the validation section, the observed field variables are the flow velocities and SSC. To convert the simulated solids volumetric concentration (α_{solids}) into SSC, the following equation is used:

$$SSC\,[mg/l] = 2.65 \cdot 10^6 \cdot \alpha_{solids} \tag{6.1}$$

Where α_{solids} denotes the simulated solids volumetric concentration. The SSC unit of mg/l is used following the unit of the laboratory measurement data. Thus the resulting spatial plot and validation of the flow velocities and SSC of each simulation cases are presented in the following section.

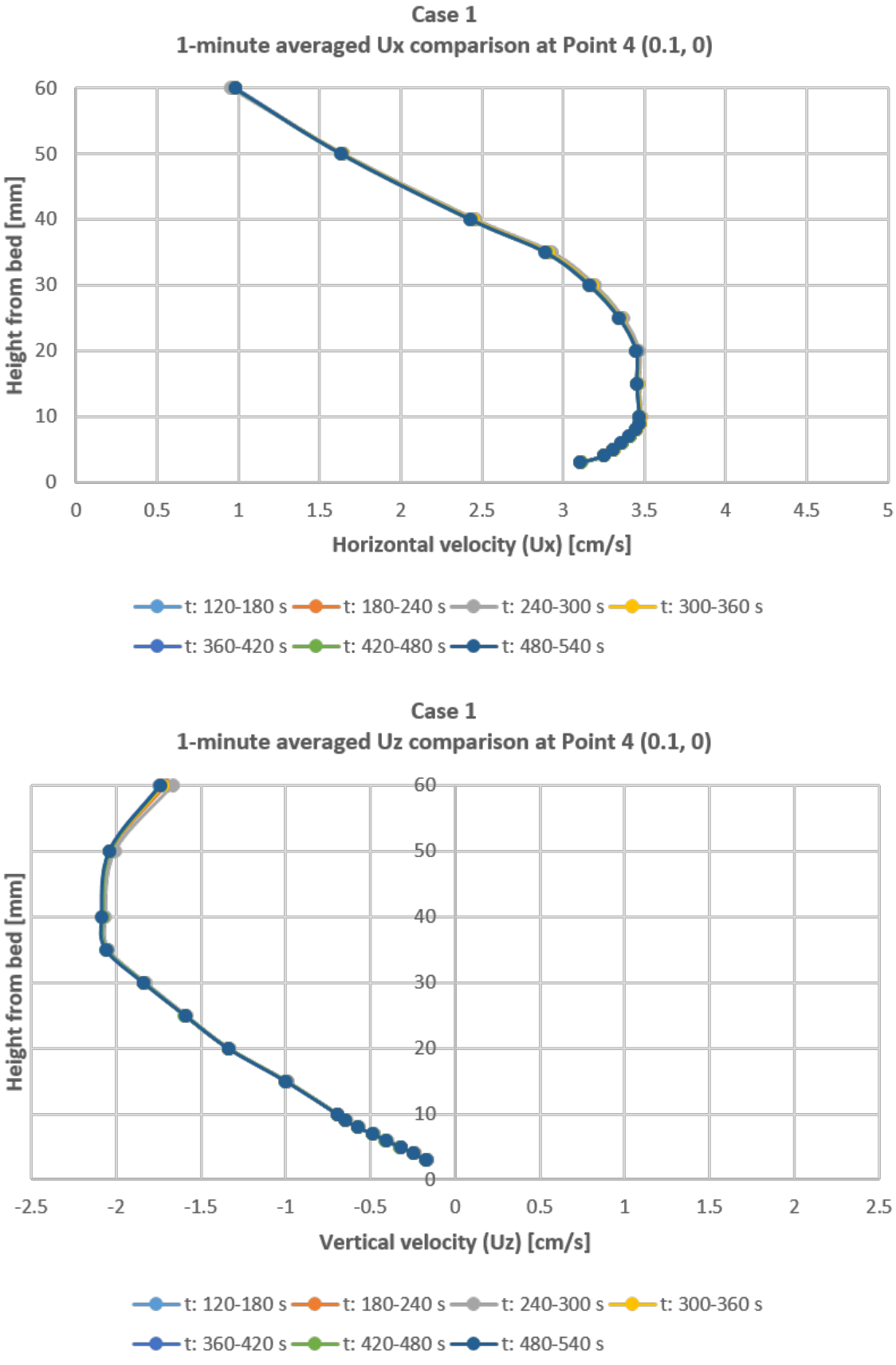

Figure 6.2: Identifying steady-state condition of the simulated flow at Point 4

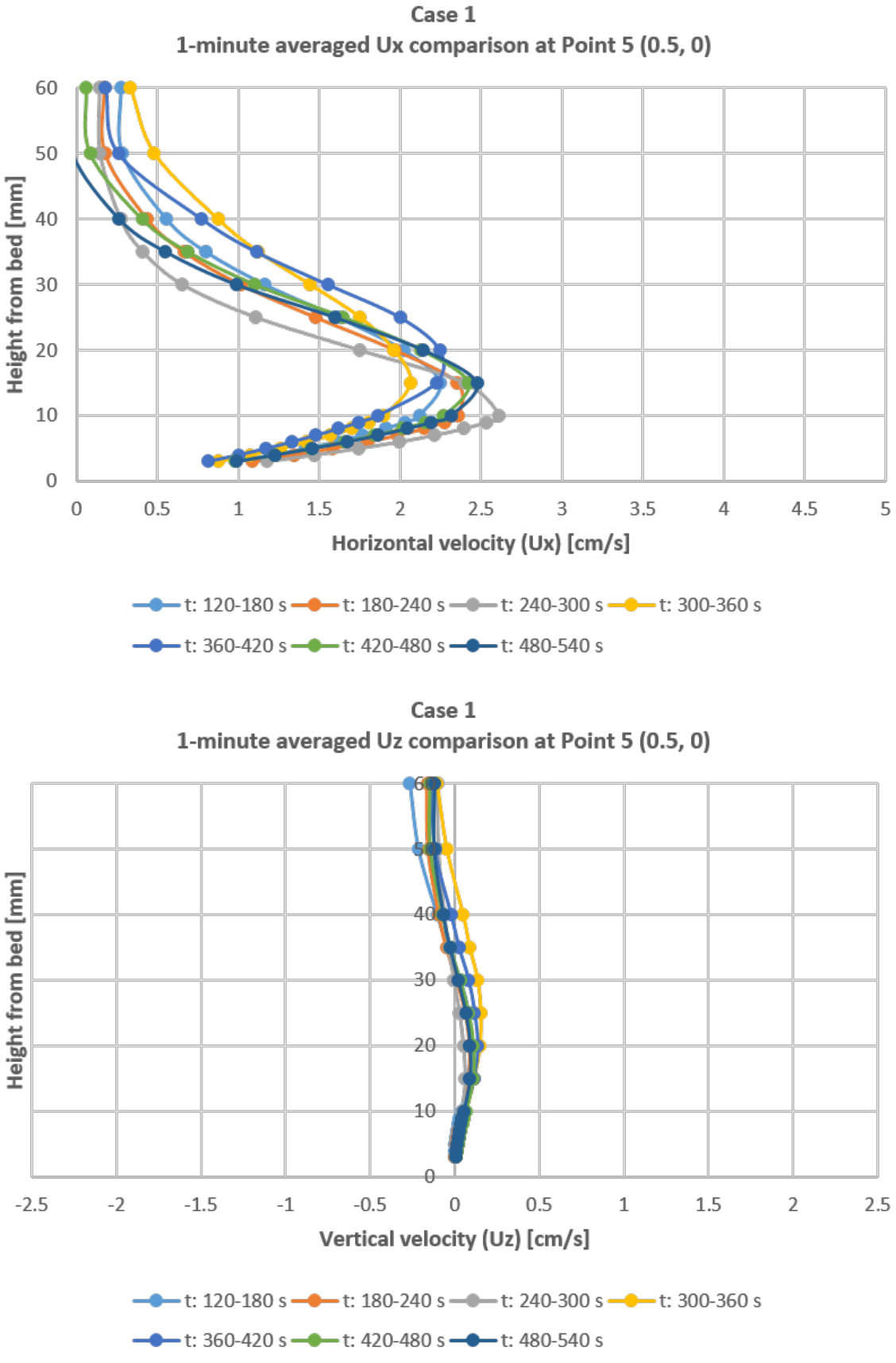

Figure 6.3: Identifying steady-state condition of the simulated flow at Point 5

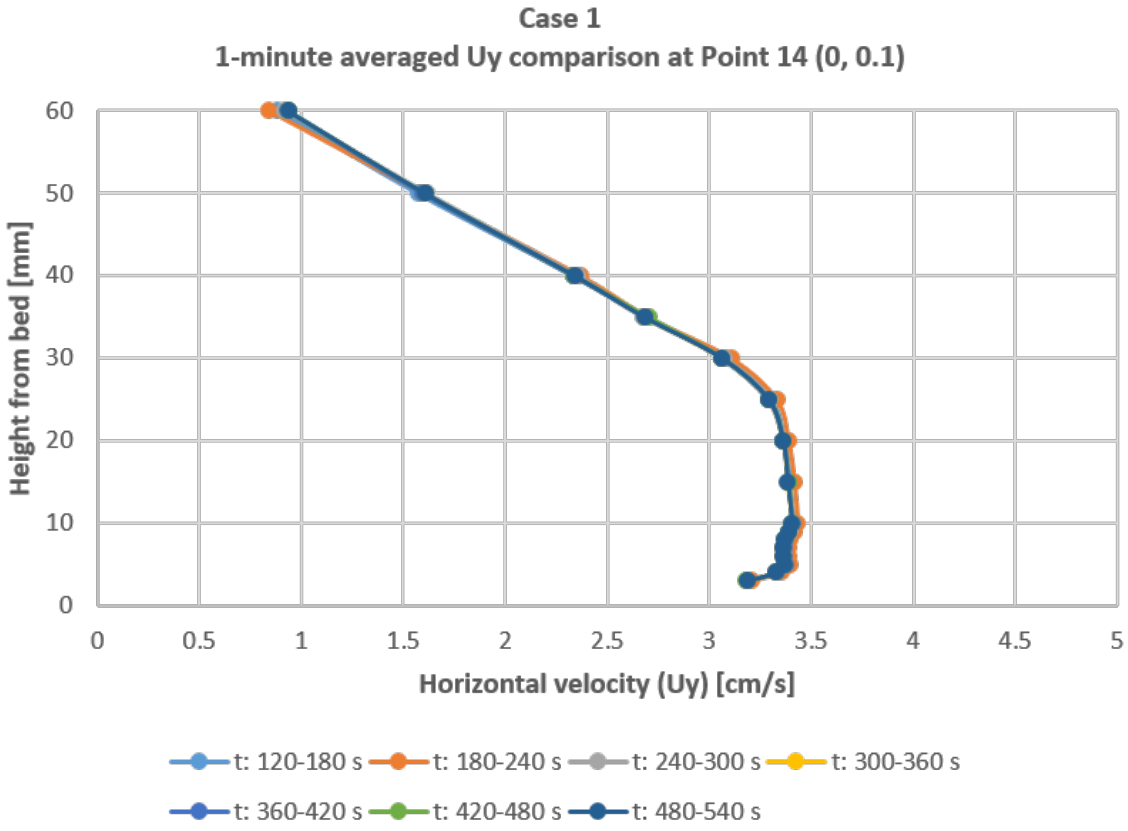

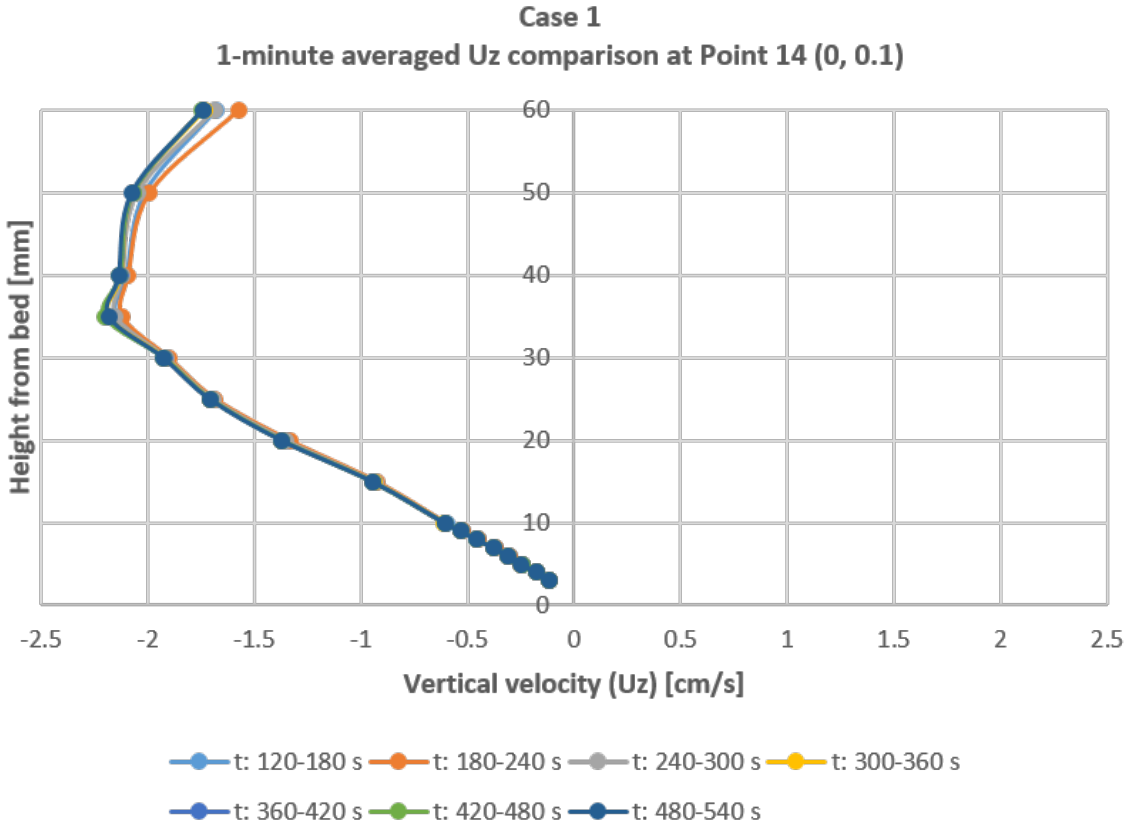

Figure 6.4: Identifying steady-state condition of the simulated flow at Point 14

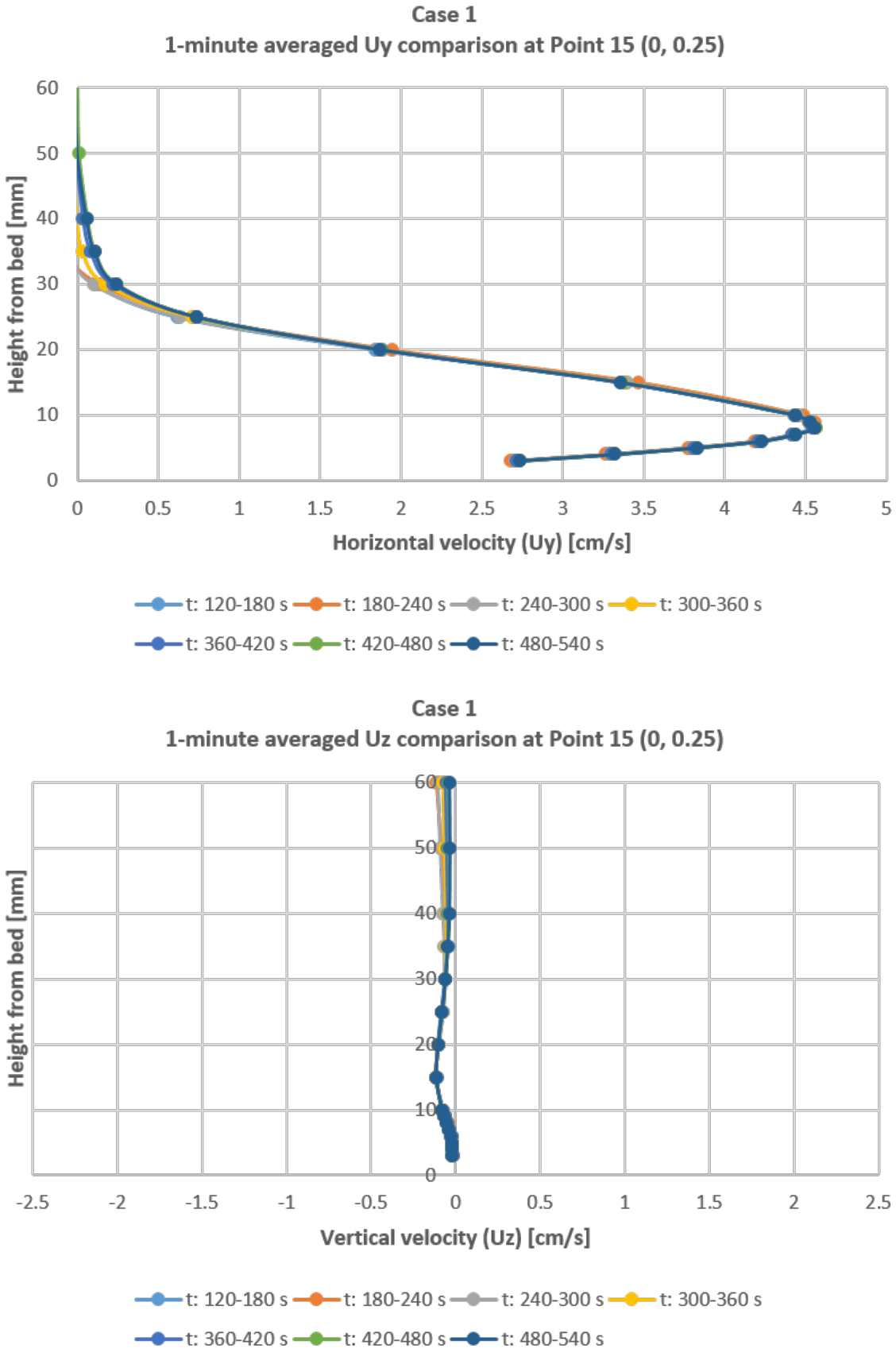

Figure 6.5: Identifying steady-state condition of the simulated flow at Point 15

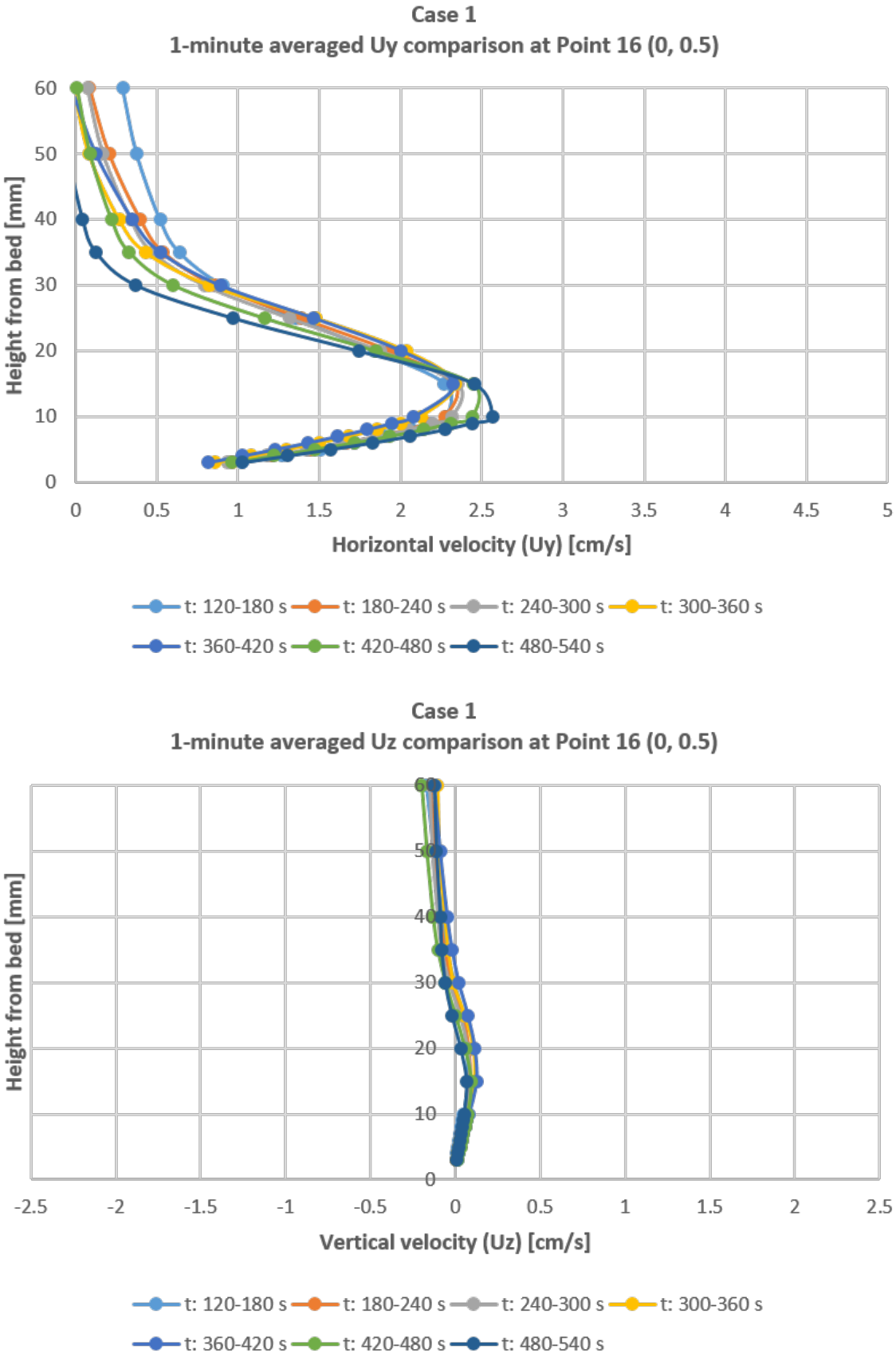

Figure 6.6: Identifying steady-state condition of the simulated flow at Point 16

6.2.3. Case 1: Minimum Solids Settling ($\mathbf{v}_{ts} = 0$)

The spatial plot of the SSC from simulation cases 1A and 1B can be seen in Figure 6.7 and 6.8. Although the constructed simulation setup is expected to generate stable result in Gauss Gamma differencing scheme, it turns out to also shows a stable result using Gauss Linear differencing scheme. At the initial phase of discharging, it can be seen that the interaction between the jet and the ambient water creates large eddies structure besides the main jetstream. These eddy structures can be seen in both cases 1A and 1B. Then the impingement of the buoyant-jet to the tabletop results in a radial spreading of the mixture. Since there is no hindered settling velocity assigned as the relative velocity of the tailings phase, the spreading of the tailings mixture becomes wider as the simulation time goes. It can be seen that the eddies in the water column become larger as the simulation goes further. One thing to be noted is the simulation using Gauss Linear (case 1B) seems to result in more turbulent structures around the tabletop compared to the simulation using Gauss Gamma as the differencing scheme (case 1A). Thus it can be noticed that Gauss Gamma differencing scheme with γ value of 0.1 seems resulting in too bounded solutions for the sake of stability. This phenomenon can also be seen near the inlet patch boundary since entrainment and mixing should have occurred as well in this area. However, as can be seen in Figure 6.7, a smoother solution is observed, neglecting the expected eddies and vortices.

From the spatial plot of the flow velocities (see Figure 6.9 and 6.11), it can be seen that the resulting flow profile is jet-like. This is due to the assumption used, and the adaptation implemented which is required to maintain an acceptable computational time and performance. Hence top-hat profile implemented at the inlet patch seems to be well-conserved. This can be seen from the profile of the vertical velocity at the core of the jetstream, which shows a uniform top-hat profile. The upward velocity occurring on the tabletop is observed to follow the transport of the tailings mixture since both SSC and vertical velocity plots show a similar profile. After the impingement, the resulting horizontal flow velocity is seen to be developing in an approximately similar magnitude as the inlet jet velocity.

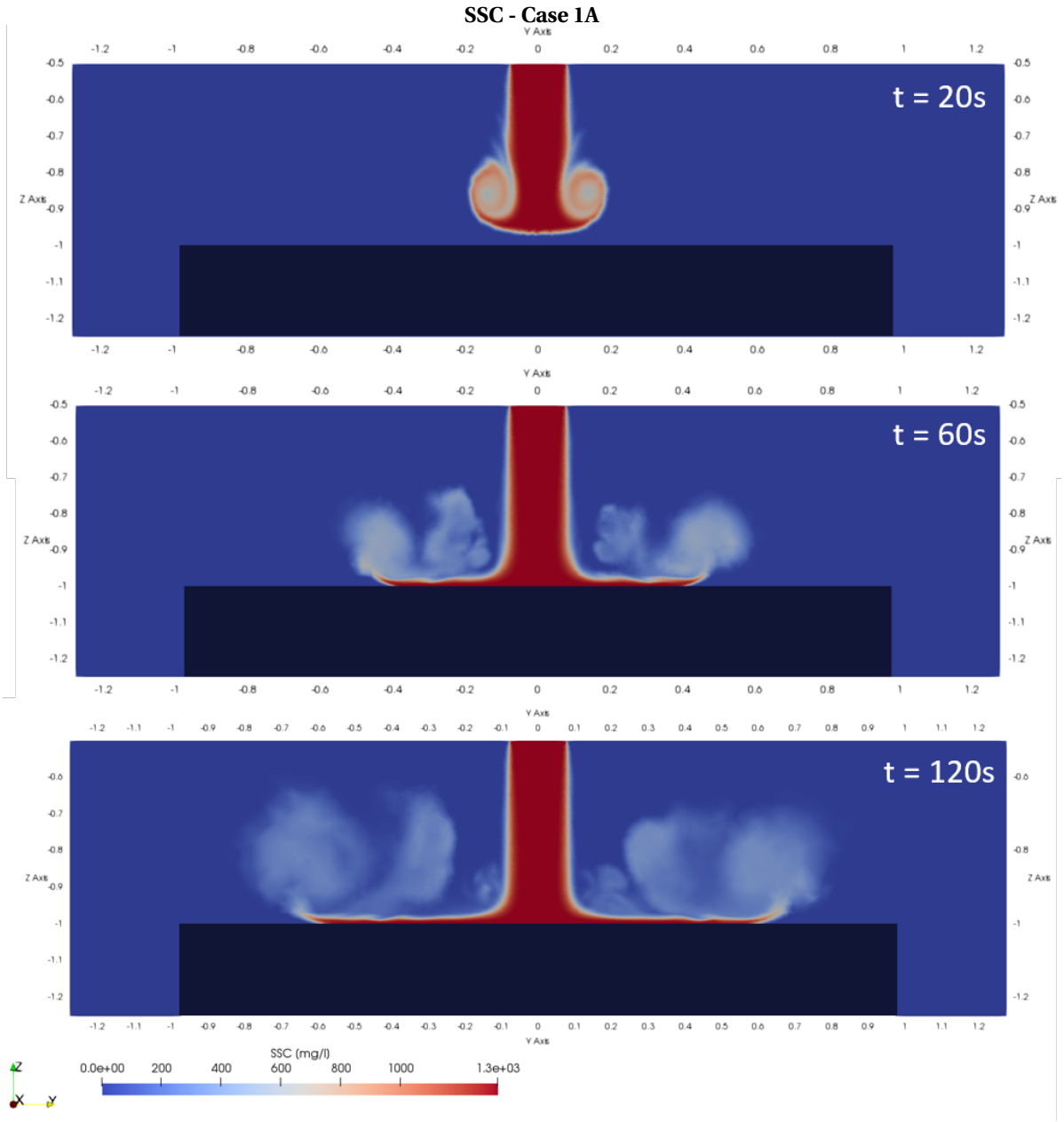

Figure 6.7: Spatial plotting of the simulated SSC of Case 1A, at halfwidth of domain with x-axis as the normal axis

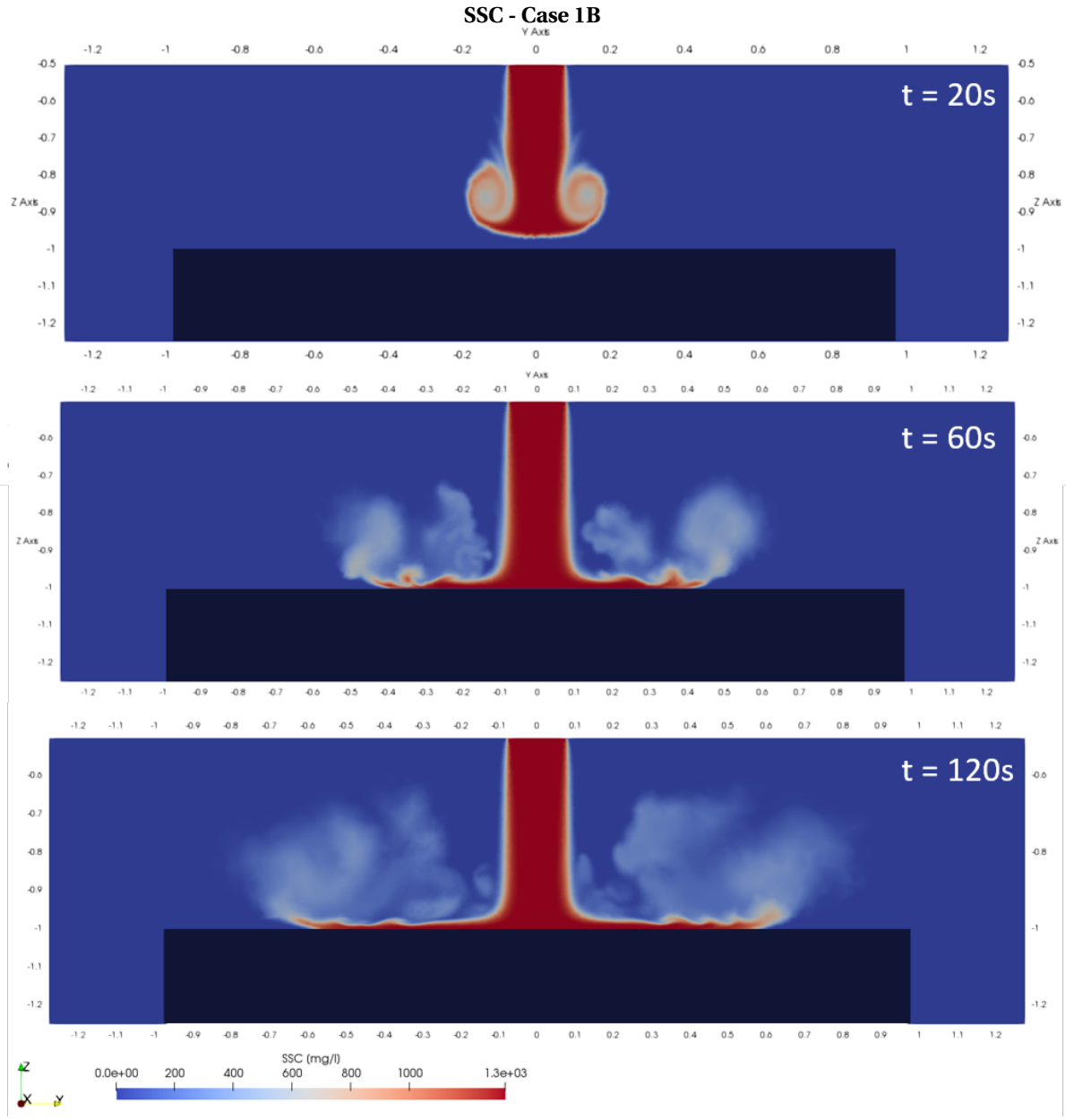

Figure 6.8: Spatial plotting of the simulated SSC of Case 1B, at halfwidth of domain with x-axis as the normal axis

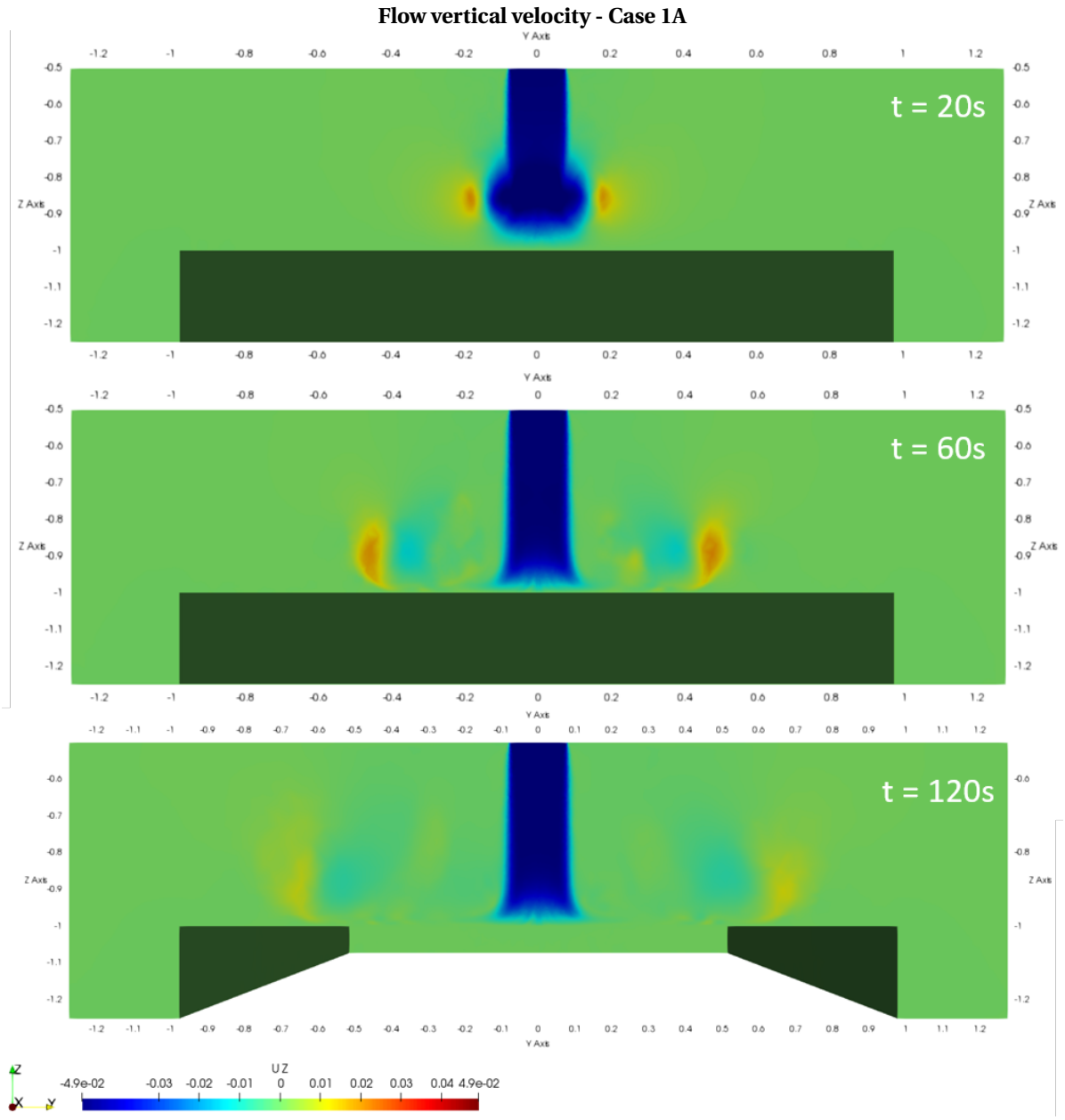

Figure 6.9: Spatial plotting of the simulated vertical velocity of Case 1A, at halfwidth of domain with x-axis as the normal axis

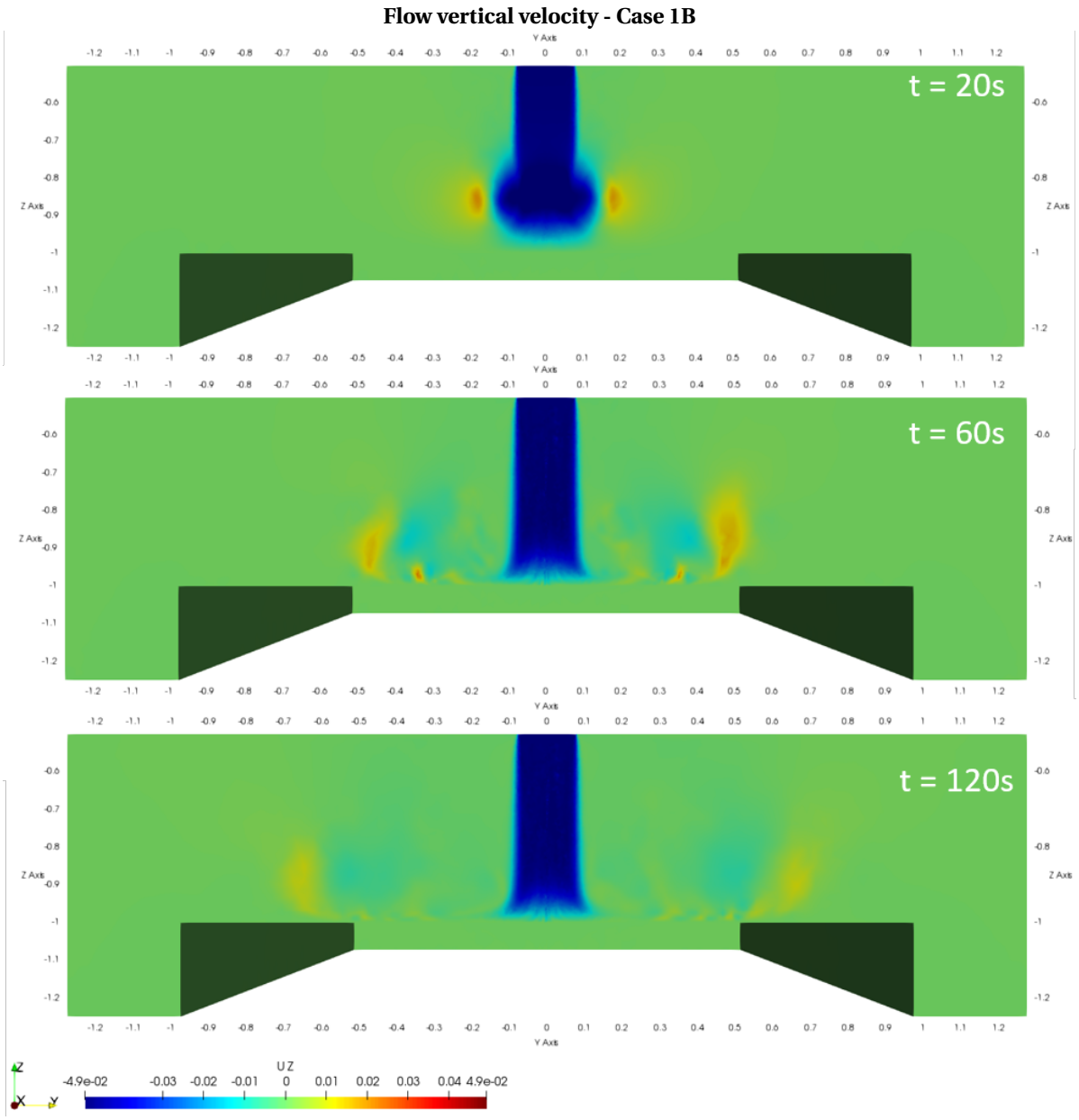

Figure 6.10: Spatial plotting of the simulated vertical velocity of Case 1B, at halfwidth of domain with x-axis as the normal axis

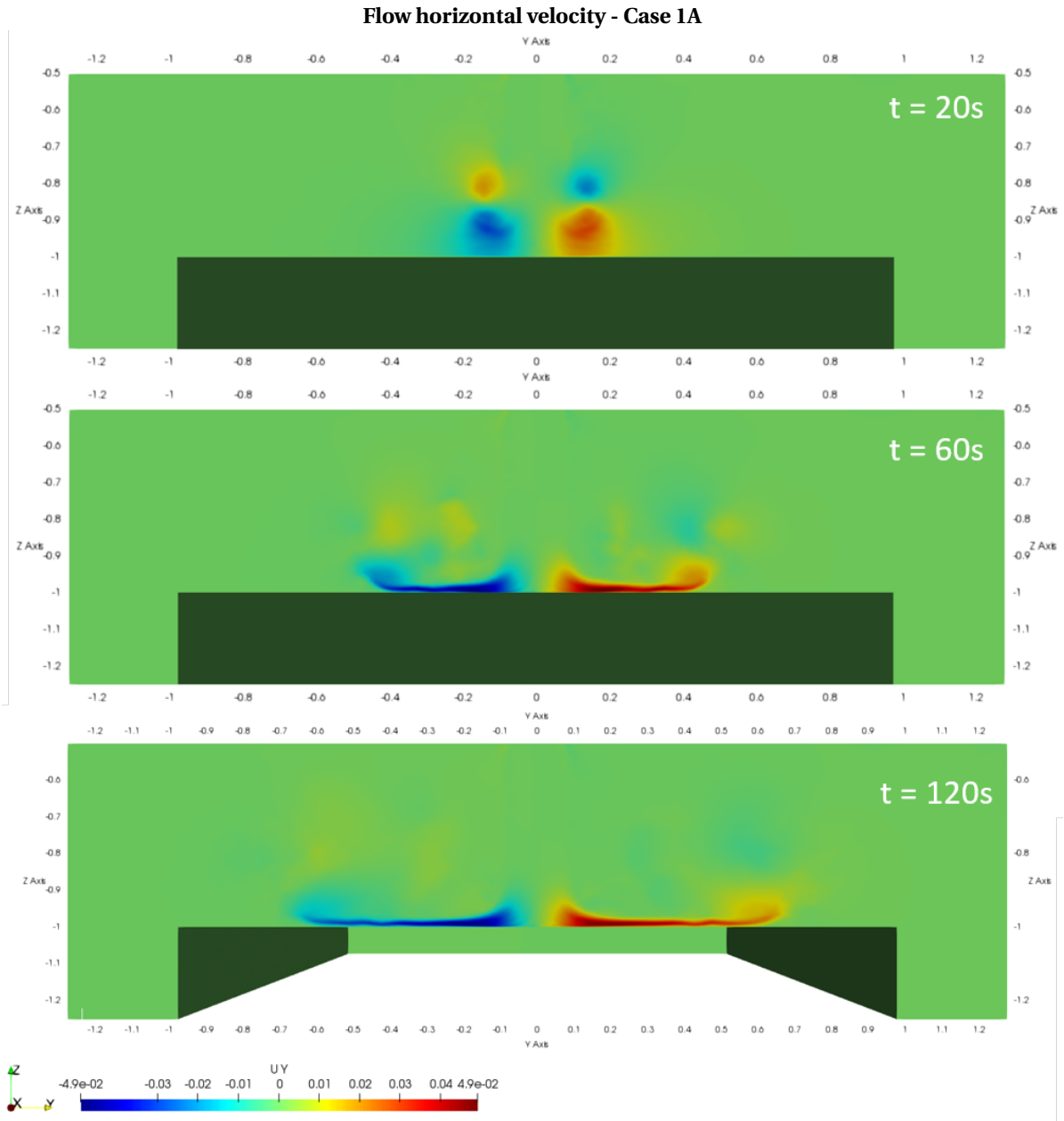

Figure 6.11: Spatial plotting of the simulated horizontal velocity of Case 1A, at halfwidth of domain with x-axis as the normal axis

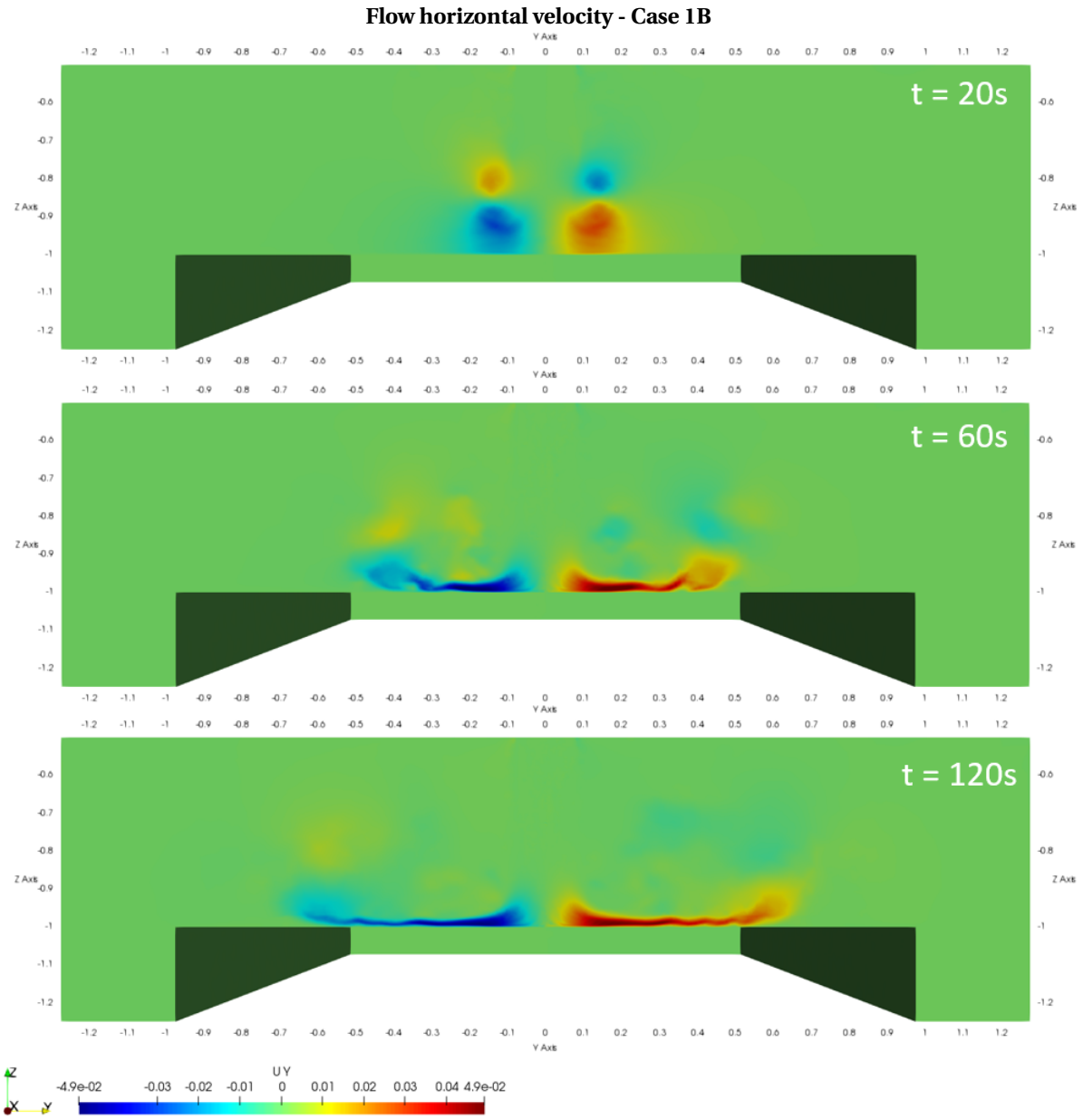

Figure 6.12: Spatial plotting of the simulated horizontal velocity of Case 1B, at halfwidth of domain with x-axis as the normal axis

6.2.4. Case 2: Extreme Solids Settling

A thing that can be directly noticed from the spatial plot of SSC of Case 2A and 2B is the absence of solids fraction in the water column after some simulation time (see Figure 6.13 and 6.14). The absence of the suspended solids is due to the high settling velocity that is implemented. To validate this hypothesis, the profile of the solids concentration in cells near the tabletop should be observed. As solids fraction usually has a higher density than water, the buoyancy, amplified by the implemented relative velocity, should lead to downward motion of the solids that still suspended in the water column. In Figure 6.13 and 6.14, there are layers near tabletop that can be observed with high concentration of solids, indicated with the bright red color. This can be observed clearer in Figure 6.15. The concentration of the solids in cells near the tabletop is kept on increasing as the simulation goes longer. It even results in hyper-concentration of the solids fraction in the first layer of the cells on the tabletop.

Another thing to be observed is during the comparison between the SSC plot (Figure 6.13 and 6.14) and flow vertical velocity plot (Figure 6.16). Observed in the vertical velocity plot, there are upward flow velocities occurring around the tabletop, with a magnitude of around $10mm/s$. This magnitude is higher than the implemented relative velocity from the terminal settling velocity of the solids fraction in these cases (around $6.8mm/s$). Thus the resulting motion of the mixture should be upward and thus re-suspend the solids fraction to the water column. However observing the SSC plot, the concentration of the suspended solids fraction is visually unobserved. The suspect of this inability of solids re-suspension is due to the absence of pick-up/erosion function in the numerical model. Thus although there are high buoyant-jet momentum impinges the solids particles in the cells on the tabletop, the expected erosion of the solids does not occur. Moreover the remaining solids that still suspending in the water column are going in a constant settling process due to the constant relative velocity — hence resulting in a high concentration of solids in the cell layers on the tabletop.

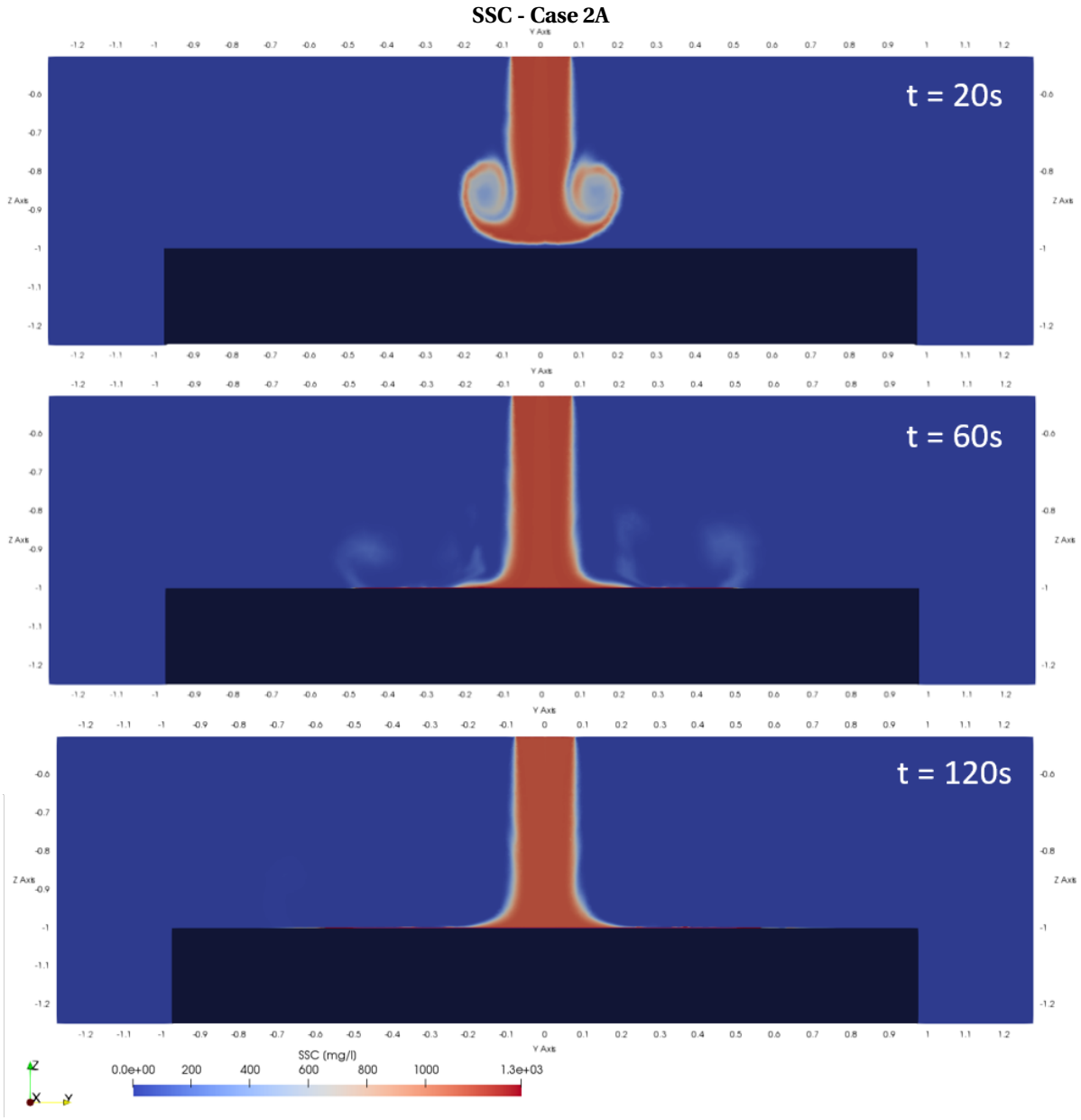

Figure 6.13: Spatial plotting of the simulated SSC of Case 2A, at halfwidth of domain with x-axis as the normal axis

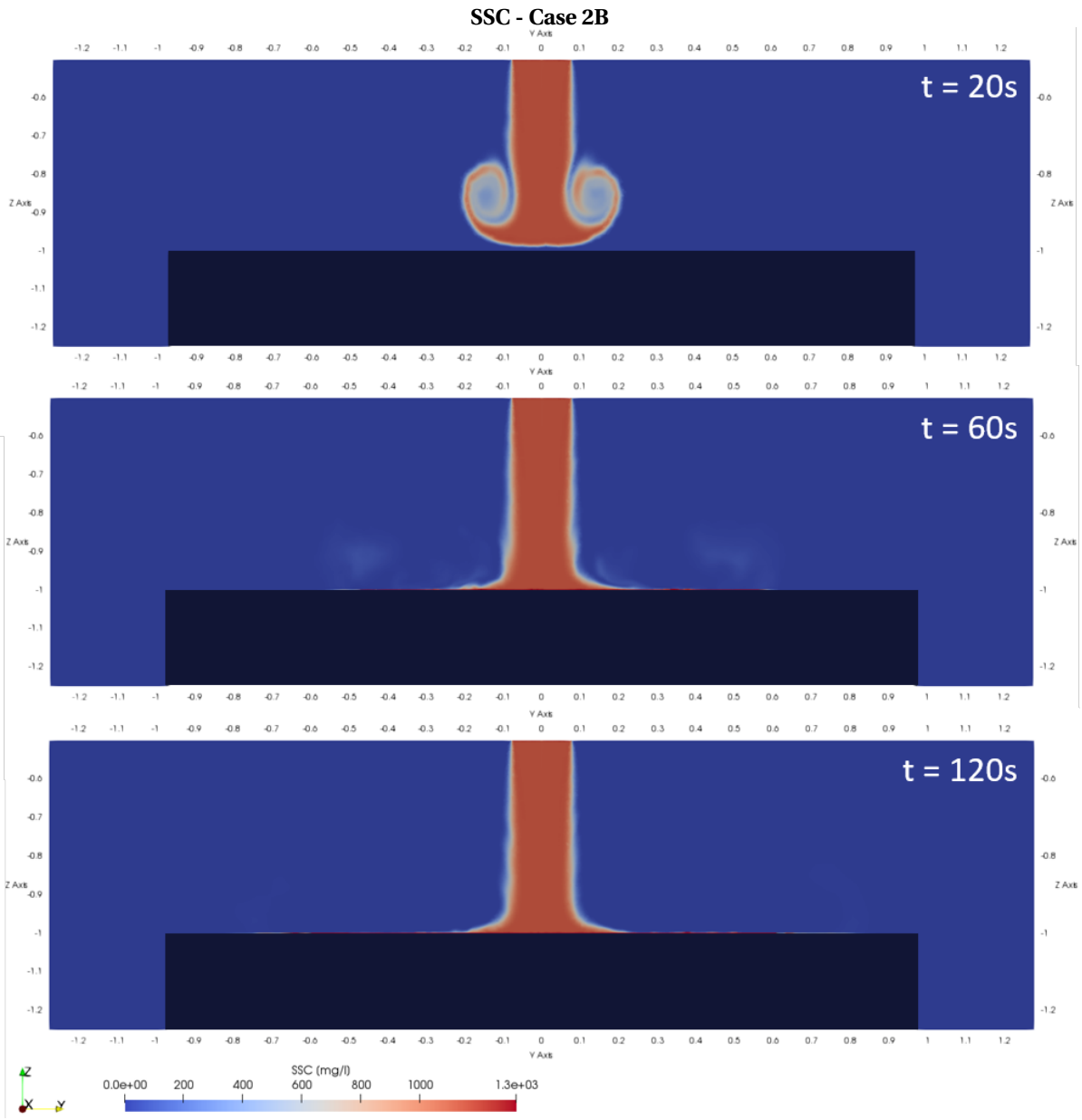

Figure 6.14: Spatial plotting of the simulated SSC of Case 2B, at halfwidth of domain with x-axis as the normal axis

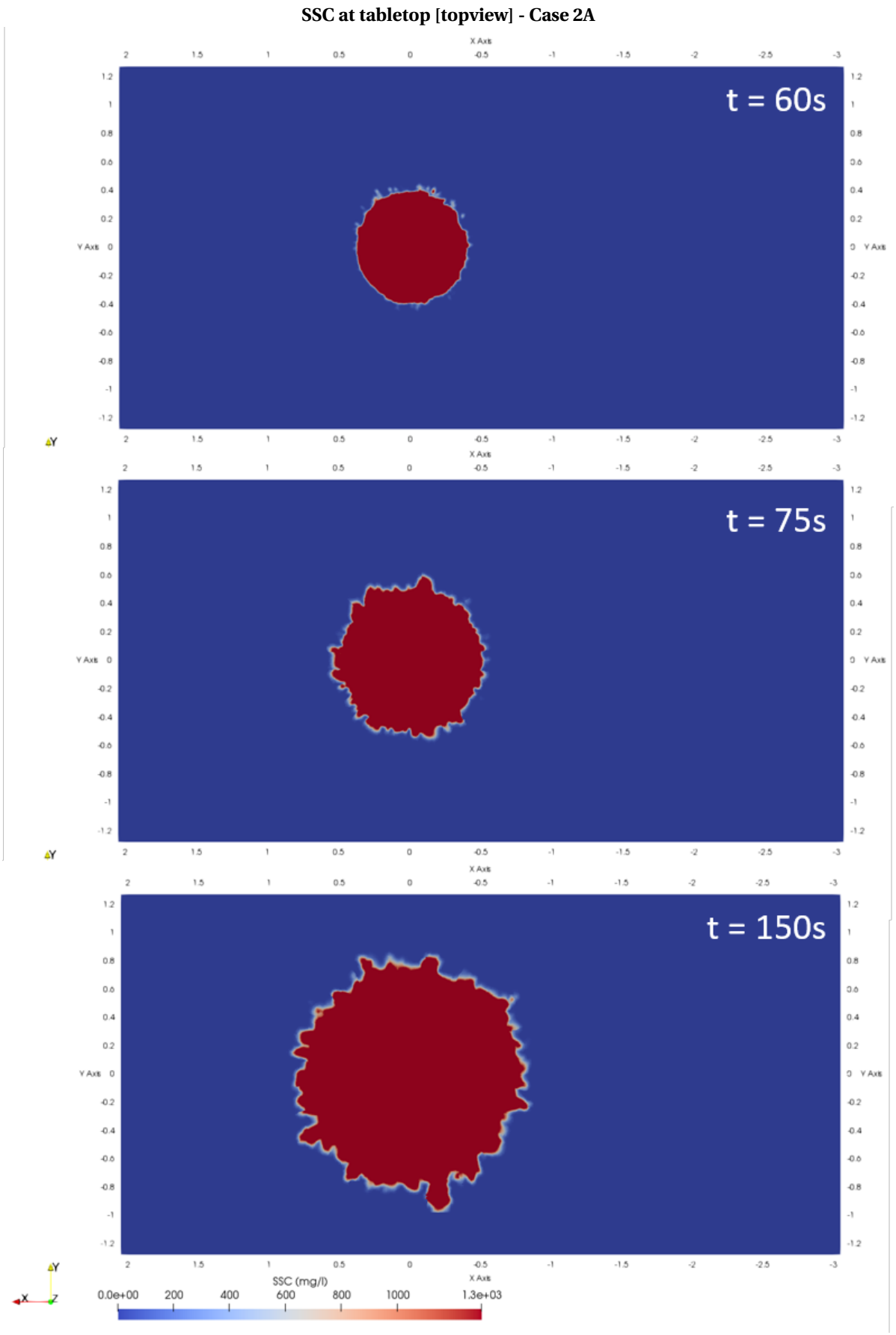

Figure 6.15: Spatial plotting of the simulated SSC of Case 2A, at topview of the tabletop

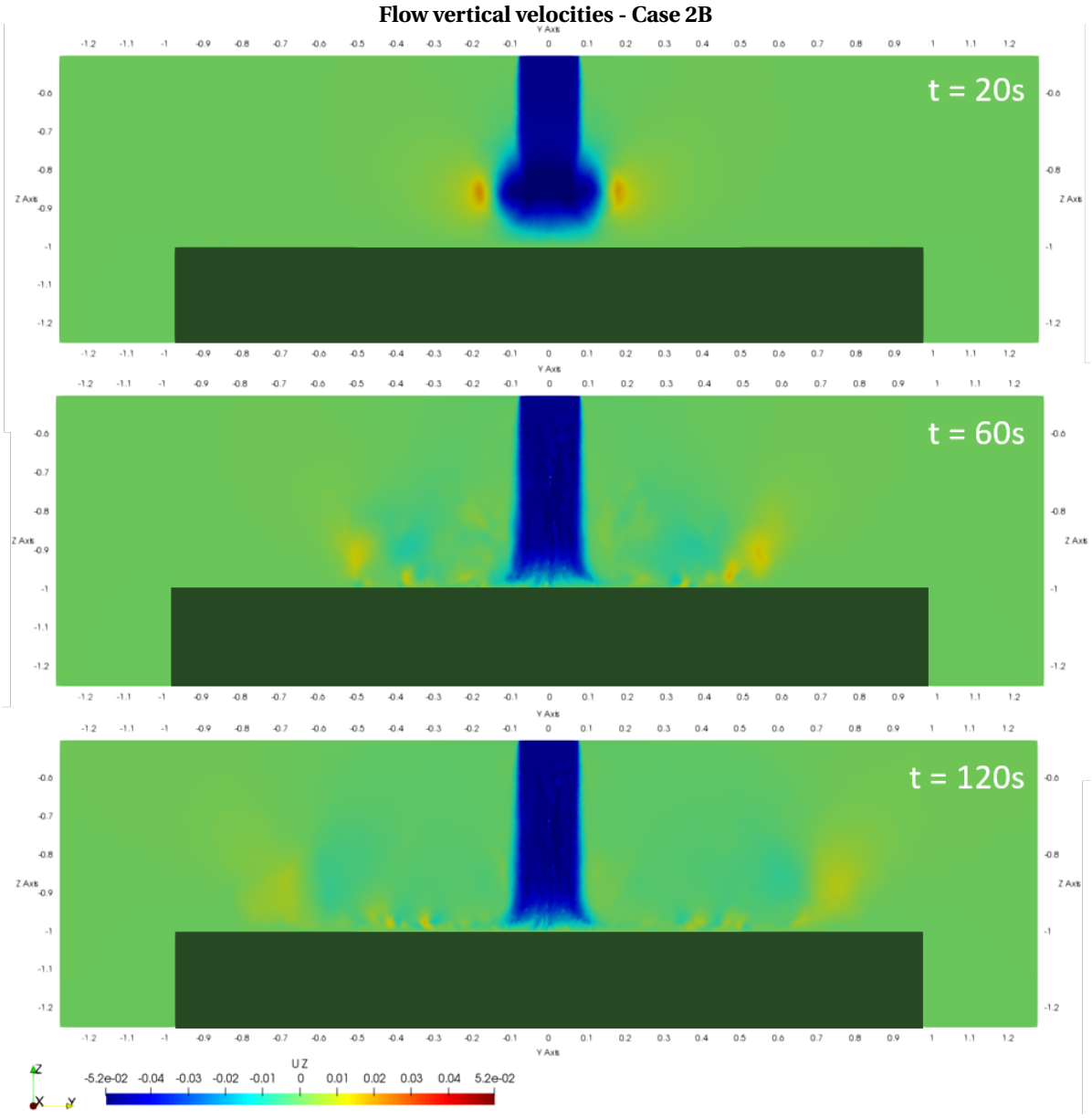

Figure 6.16: Spatial plotting of the simulated vertical velocity of Case 2B, at halfwidth of domain with x-axis as the normal axis

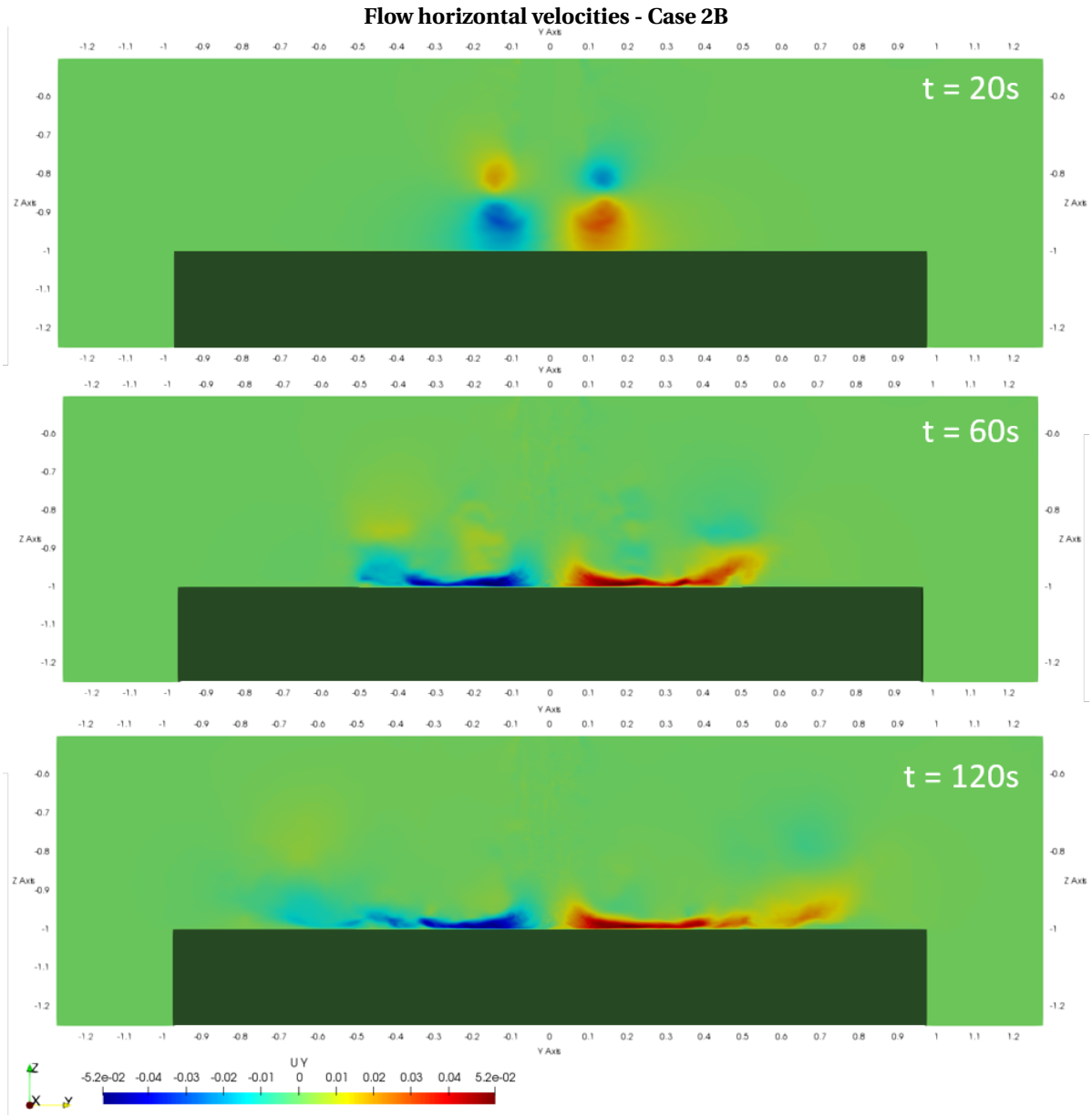

Figure 6.17: Spatial plotting of the simulated horizontal velocity of Case 2B, at halfwidth of domain with x-axis as the normal axis

6.2.5. Case 3: Realistic Solids Settling

Here the spatial plotting of the SSC of Case 3 simulations is presented. As mentioned before, Case 3 uses particle diameter of d_50 from the laboratory measurement. The picked diameter results in settling velocity six times smaller than resulting settling velocity in Case 2. Therefore more suspension of solids can be seen compared to Case 2. Comparing Case 3A and 3B, there are fewer solids suspending at $t = 60s$ for Case 3A compared to Case 3B.

Moreover, there are less turbulent structures around the jet in Case 3A, which uses Gauss Gamma differencing scheme. There are also more turbulent structures around the front of the underflow compared to Case 2, which identifies the mixing occurring between the underflow and the ambient water. As the simulation goes, settling of the suspended solids still occurs due to the constant settling velocity, which results in hyper-concentration of the cell layers near the tabletop. Hence it can be concluded that pick-up function is needed to be implemented along with the solids settling function.

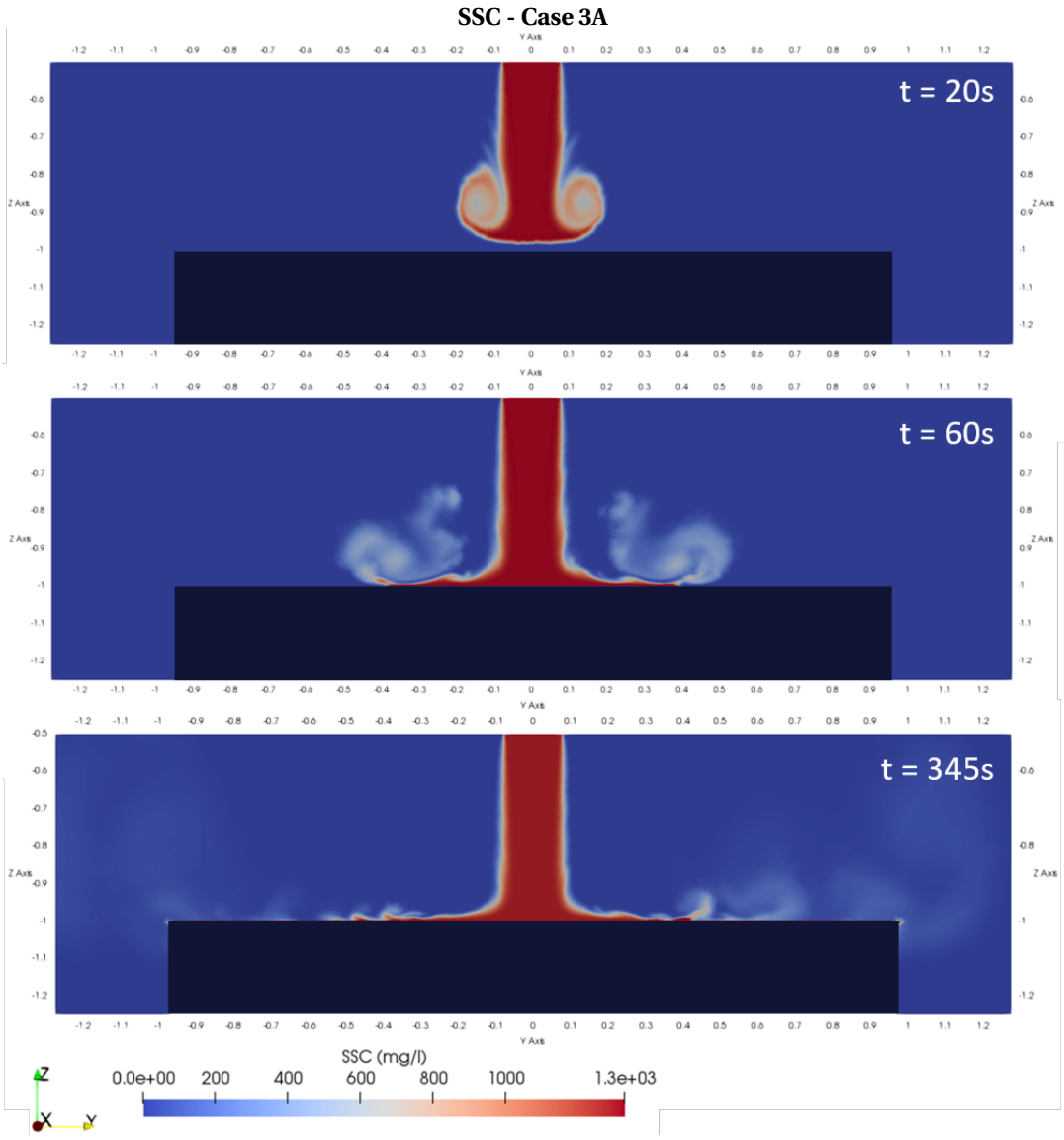

Figure 6.18: Spatial plotting of the simulated SSC of Case 3A, at halfwidth of domain with x-axis as the normal axis

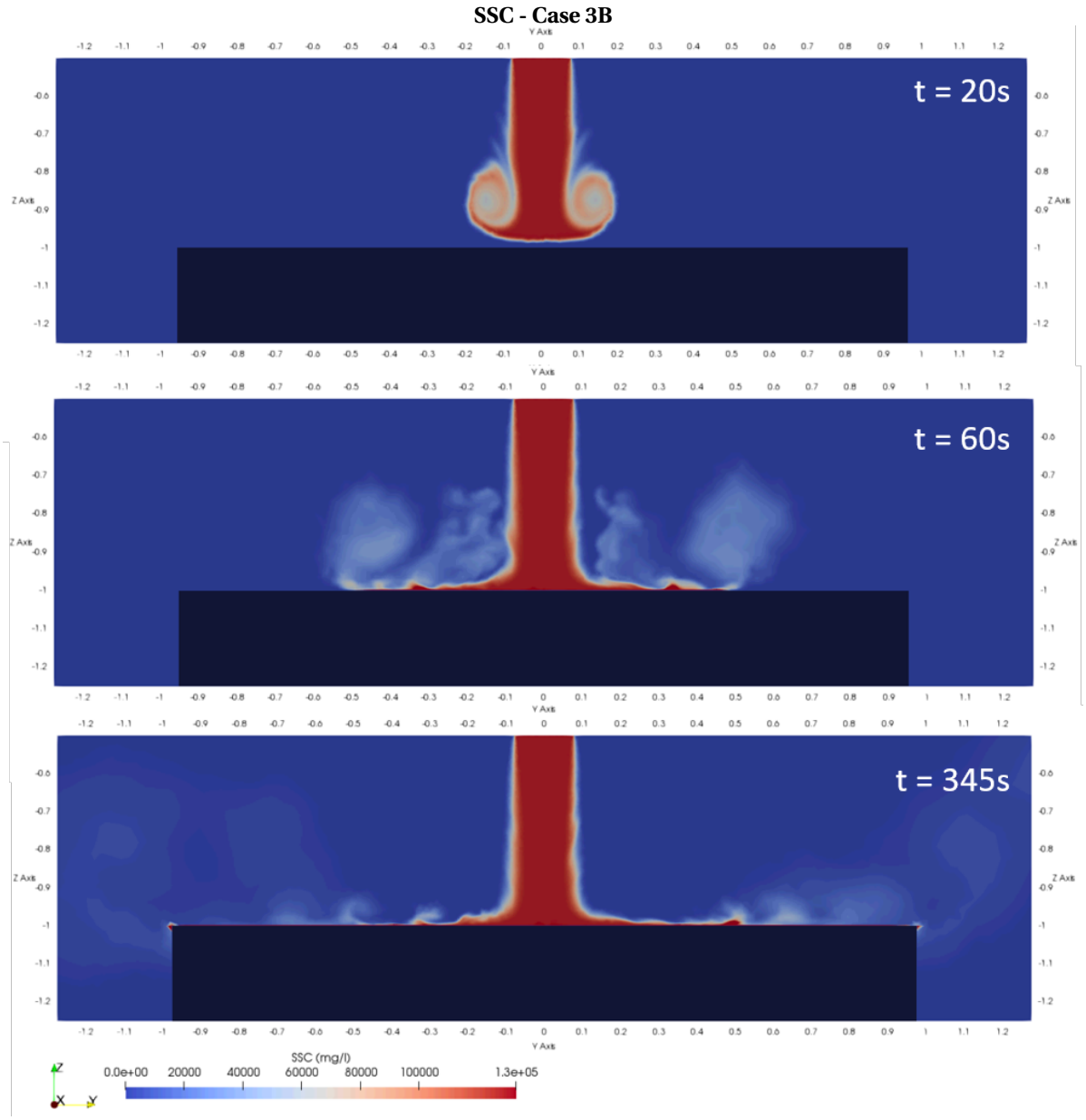

Figure 6.19: Spatial plotting of the simulated SSC of Case 3B, at halfwidth of domain with x-axis as the normal axis

6.2.6. Validation of Simulation Results

After observing the spatial plot and variation of the field variables, the simulated field variables are then validated with the laboratory measurement data to observe how the simulation can represent the actual laboratory experiments as mentioned before the validation is done at measurement points 4, 5, 14, 15, and 16, due to the steady-state condition.

Validation of Flow Velocities

The validation of the flow velocities is classified for each measurement point, where each main cases (Case 1, Case 2, and Case 3) are compared individually to the laboratory measurement. The validation of Case 1 (Case 1A and Case 1B) can be seen in Figure 6.20, 6.23, 6.26, 6.29, and 6.32. The validation of Case 2 (Case 2A and Case 2B) can be seen in Figure 6.21, 6.24, 6.27, 6.30, and 6.33. The validation of Case 3 (Case 3A and Case 3B) can be seen in Figure 6.22, 6.25, 6.28, 6.31, and 6.34. As can be seen, the simulated horizontal and vertical velocities at Point 4 are similar for all cases. This similarity is approximately due to the location of Point 4 which is very close to the Impingement Point (IP). Thus the momentum from the main jetstream is still dominant. Therefore the buoyancy does not give huge effect at this point. The simulated horizontal flow velocity at this point underestimates the laboratory measurement data, while the vertical velocity overestimates the laboratory measurement data.

The difference between cases starts to be recognizable at Point 5. As seen in Figure 6.23, simulation Case 1A results in a maximum horizontal velocity with the same magnitude as the laboratory measurement data. But the resulting horizontal velocity profile at the outer region has a steep gradient compared to the laboratory data. On the other hand, Case 1B, which uses Gauss Linear differencing scheme, does not result in a maximum velocity with the same magnitude as the laboratory measurement data but has less steep gradient in the outer region of the horizontal velocity profile. At the furthest vertical height (60mm height from bed), Case 1B even has a horizontal velocity magnitude similar to the laboratory measurement.

Since the buoyant-jet is expected to flow radially after the impingement, the resulting velocity profile of Point 14, 15, and 16 are expected to be identical with Point 4 and 5. Point 14 shows a similar result with Point 4 as the distance of both points to the impingement point is similar. Thus the jet momentum also still dominates at Point 14. Point 15 is located between Point 14 and 16, which is also in the same distance as in between Point 4 and 5. As can be seen in Figure 6.29, 6.30, and 6.31, the resulting horizontal flow velocities are similar for all cases. The resulting maximum velocity gives the same magnitude as the laboratory measurement data, yet with its vertical height lower than the laboratory data. For Case 1 and Case 2, Gauss Linear and Gauss Gamma are seen to result in a similar horizontal flow profile, and a steep gradient occurred as vertical height increases above the maximum-velocity height. A difference can be seen in Case 3 where Gauss Linear has a slightly higher horizontal velocity magnitude for vertical height of 30 - 40 mm from the bed. This condition can be seen as one of the footage of damping in Gauss Gamma differencing scheme. Clearer footage can be seen in the comparison of vertical velocity of Case 2 and Case 3 at the same measurement point. As seen in Figure 6.30 and 6.31, Case 2A and 3A which use Gauss Gamma differencing scheme show lower magnitude in overall compared to the simulation using Gauss Linear differencing scheme (Case 2B and 3B). At Point 16, simulations of Case 3 seem to result in horizontal velocity profiles similar to the laboratory measurement, yet with lower magnitude. For the vertical velocity, both simulations of Case 3 result in upward vertical velocity, while the laboratory measurement shows downward motion for almost all heights. For simulations of Case 1, there are huge differences between horizontal velocity profile of Case 1A and 1B. Case 1A, which uses Gauss Gamma differencing schemes, results in a horizontal velocity that has the same magnitude of maximum velocity but steep gradient. On the other hand, Case 1B, which uses Gauss Linear differencing schemes, results

in lower magnitude of maximum velocity but with lower gradient at the outer region.

Validation of Suspended Solids Concentration

As mentioned before, the considered SSC to be validated is the local-SSC, which is represented by the 20mm-averaged SSC. In this study, the value of simulated SSC starting at the height of 3mm - 20mm is used since the sampling starts from 3mm height from tabletop. The validation is done per each differencing scheme and axis. Thus the validation of SSC for Gauss Gamma differencing scheme can be seen in Figure 6.35. For SSC of cases with Gauss Linear differencing scheme, the validation result can be seen in Figure 6.36.

The SSC profiles for all cases are overestimating the laboratory measurement data at Point 4. At other measurement points, the resulting profile seems close to the expected result. For validation of both Gauss Gamma (Case 1A, 2A, and 3A) and Gauss Linear (Case 1B, 2B, and 3B) cases, SSC from Case 1 overestimates the laboratory-measured SSC since in this case no solids are settling implemented to the model. Meanwhile simulated SSC from Case 2 underestimates the laboratory-measured SSC. In Case 2, the tailings mixture is assumed to be filled by particles with diameter higher of $95 \cdot 10^{-6} m$, higher than the particle diameters used in the mixture during the laboratory measurement. Thus the resulting settling velocity of the solid particle is higher than the settling velocity of particles in the laboratory experiments.

Consequently, more solids are settling, creating less suspension of solids in the water column. Hence the simulated SSC of Case 2 should give the "extreme" low value of SSC compared to the laboratory data. For simulation of Case 3, there are more solids suspended in the water column compared to Case 2, but less than Case 1. This condition results in SSC value that close to the laboratory-measured SSC, as can be seen in Figure 6.35 and 6.36. At Point 5 and 16 of simulation Case 3B, even the simulated SSC gives value approximately equal to the laboratory-measured SSC.

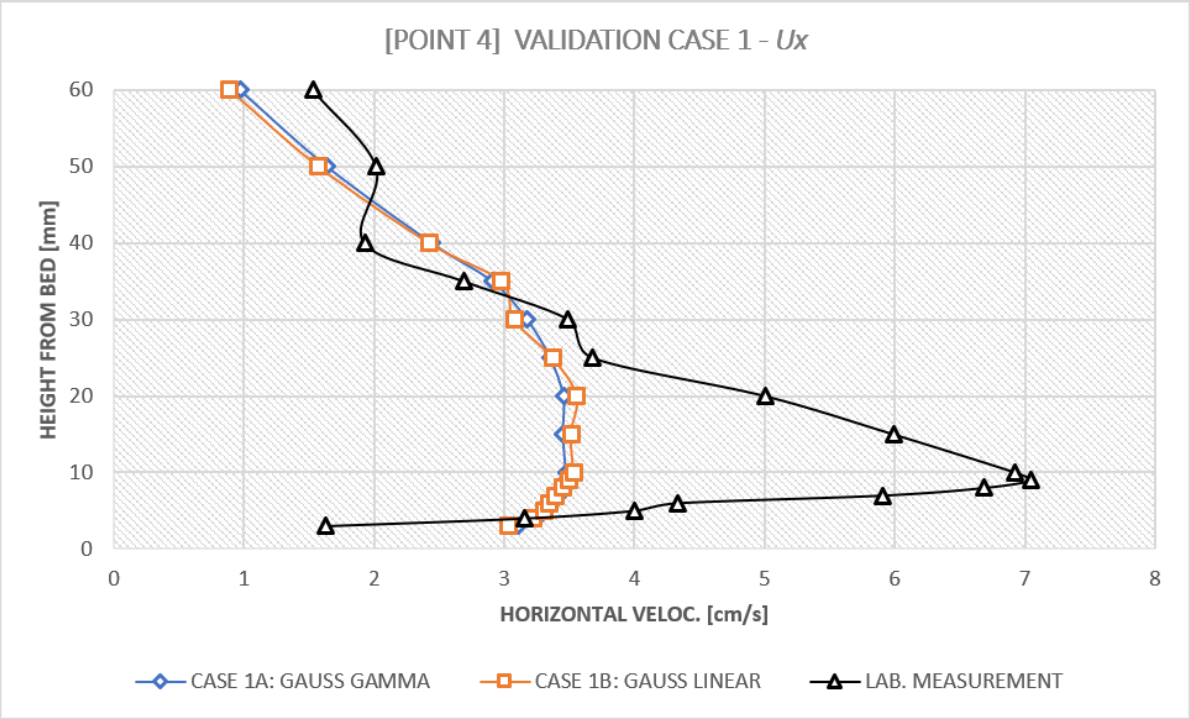

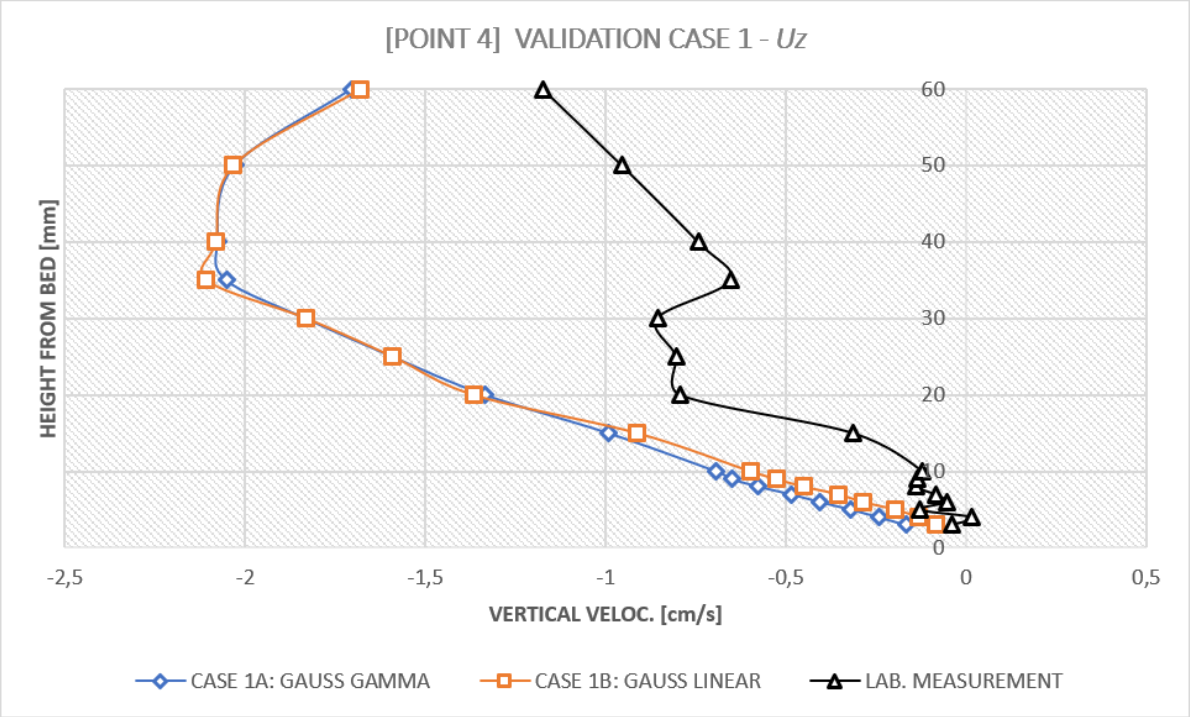

Figure 6.20: Flow velocities validation of simulation Case 1 at Point 4

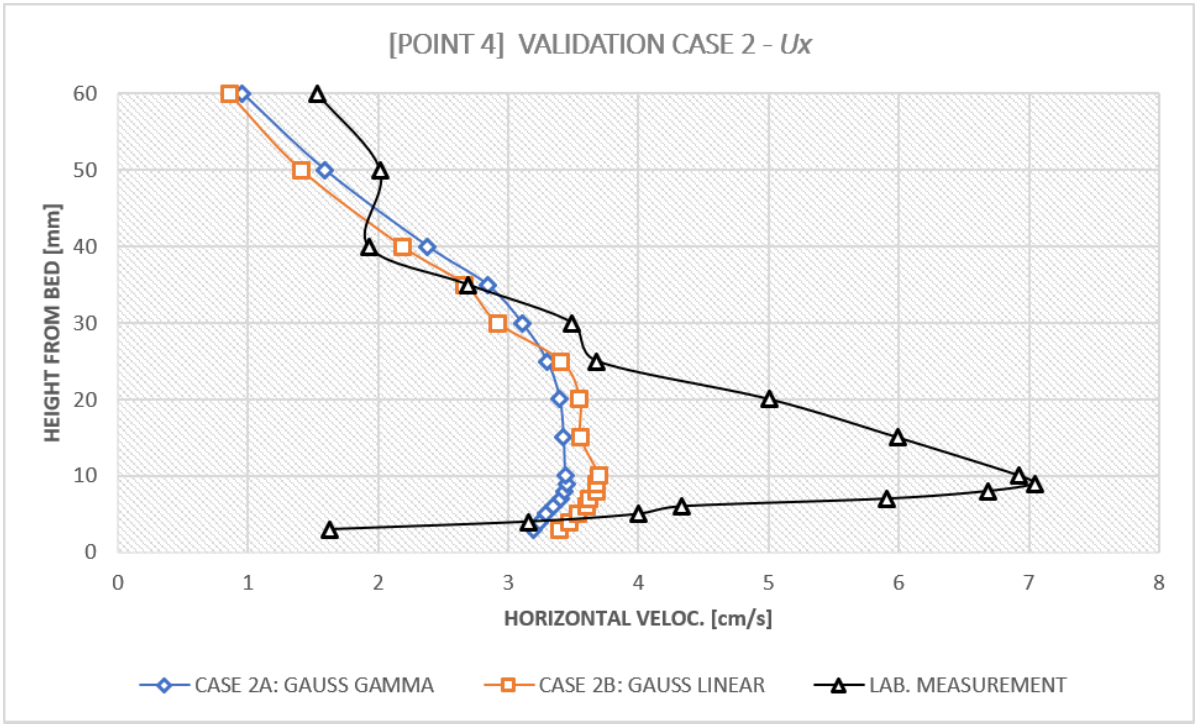

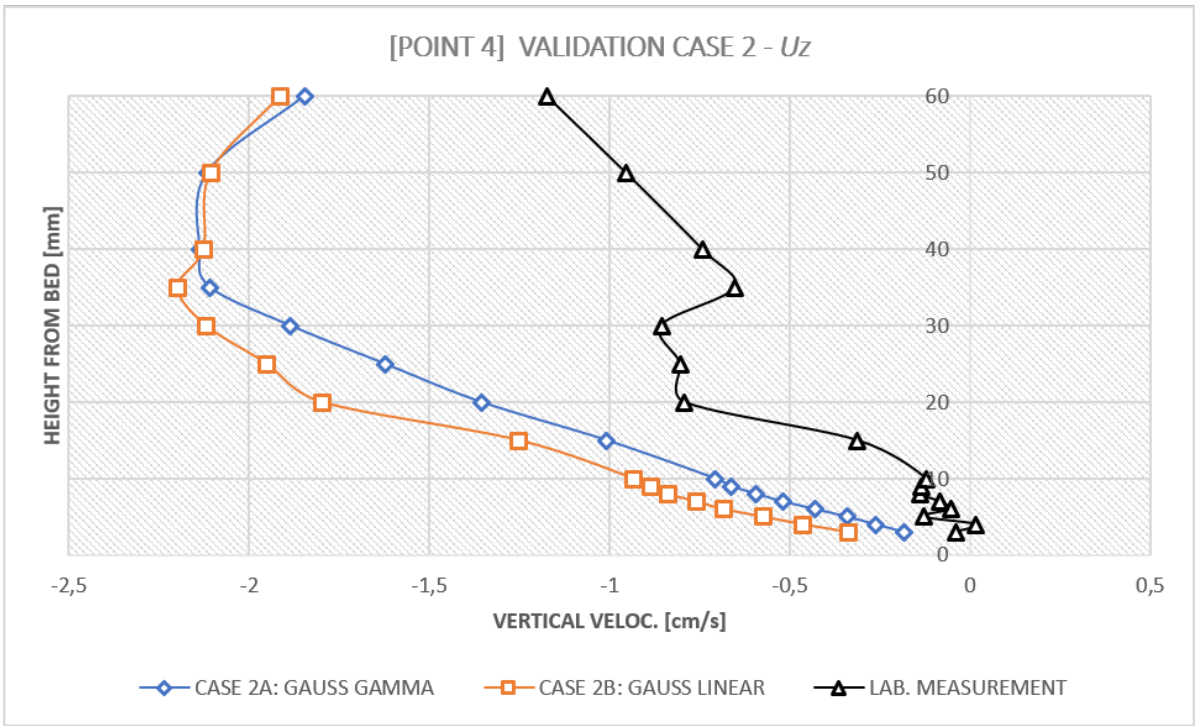

Figure 6.21: Flow velocities validation of simulation Case 2 at Point 4

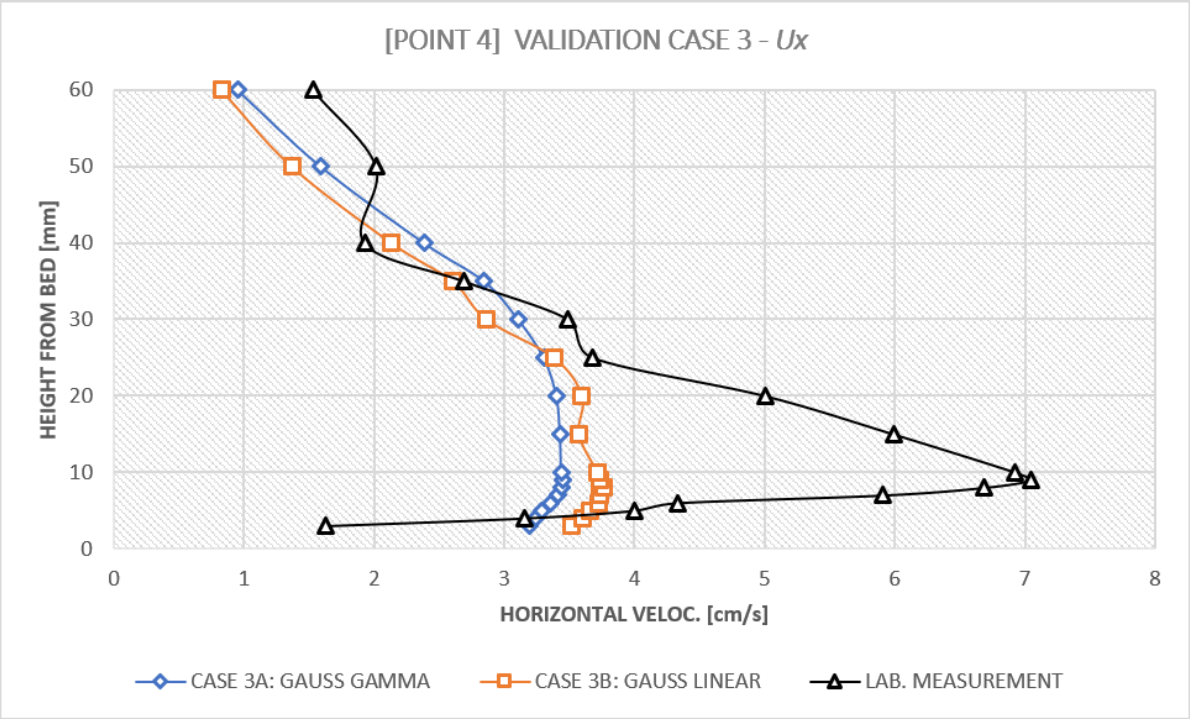

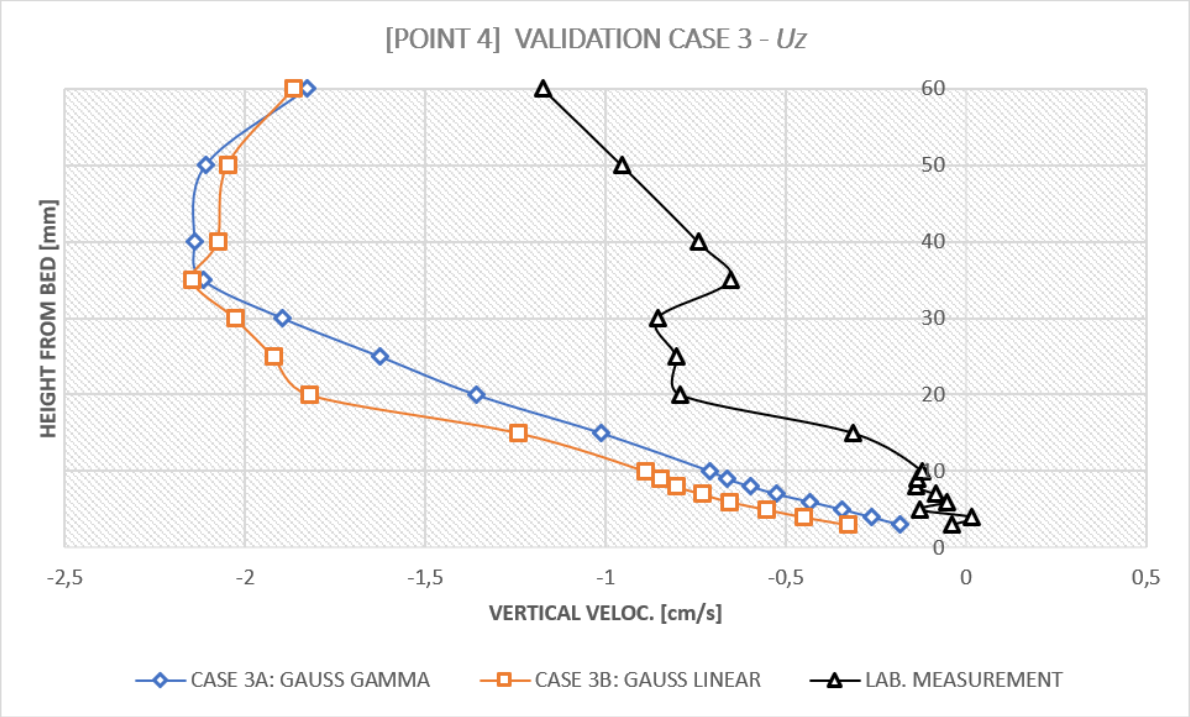

Figure 6.22: Flow velocities validation of simulation Case 3 at Point 4

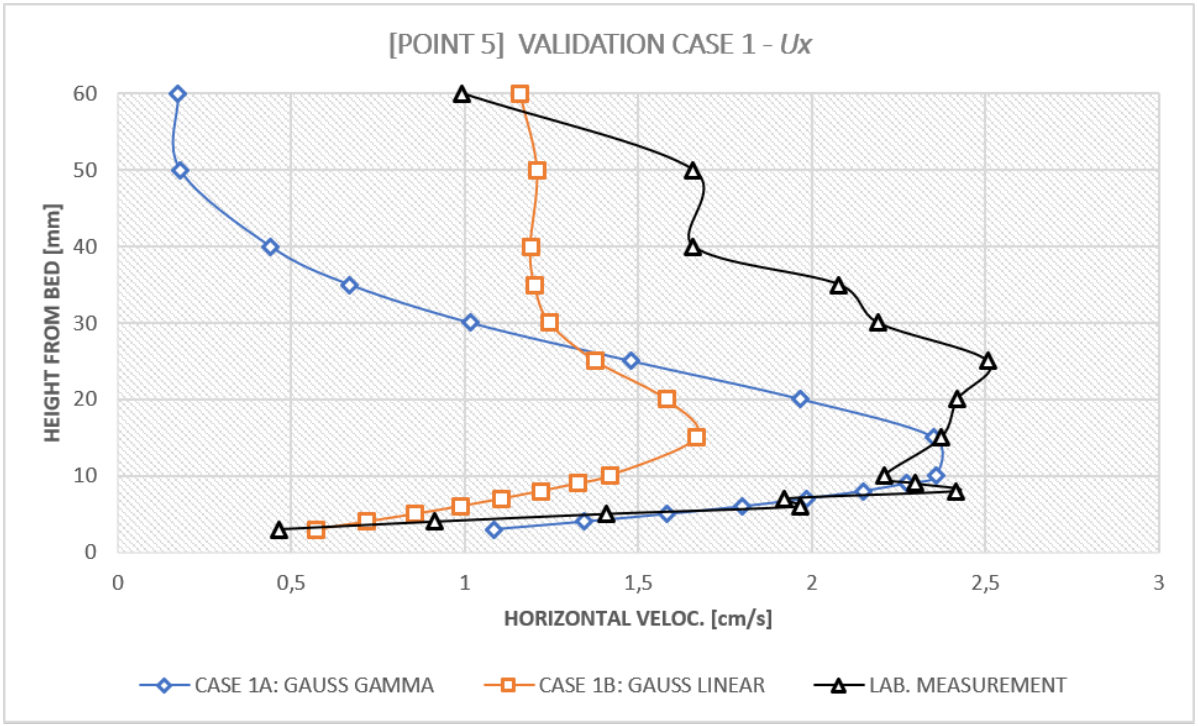

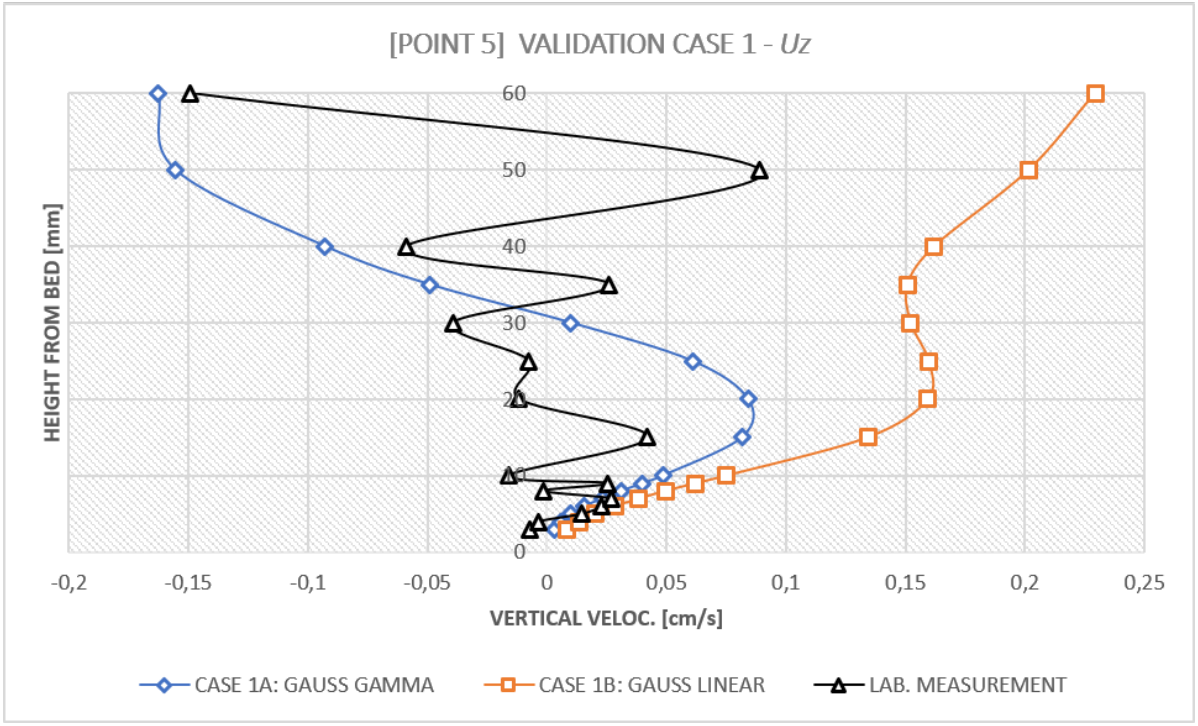

Figure 6.23: Flow velocities validation of simulation Case 1 at Point 5

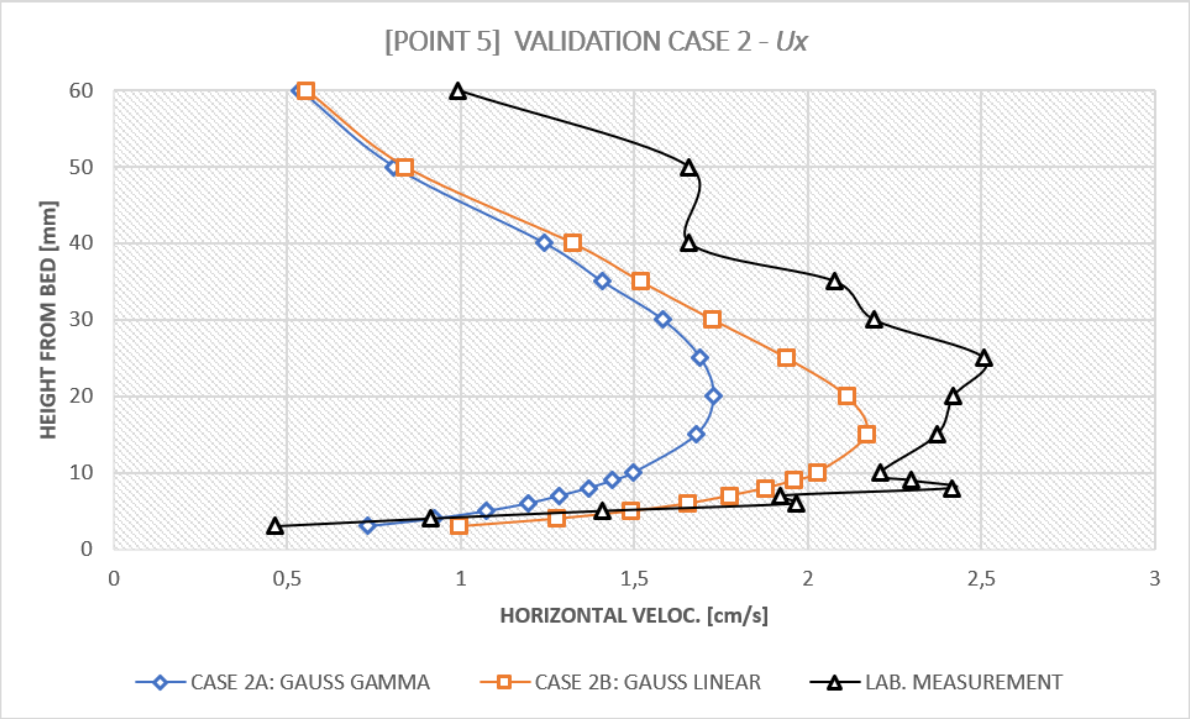

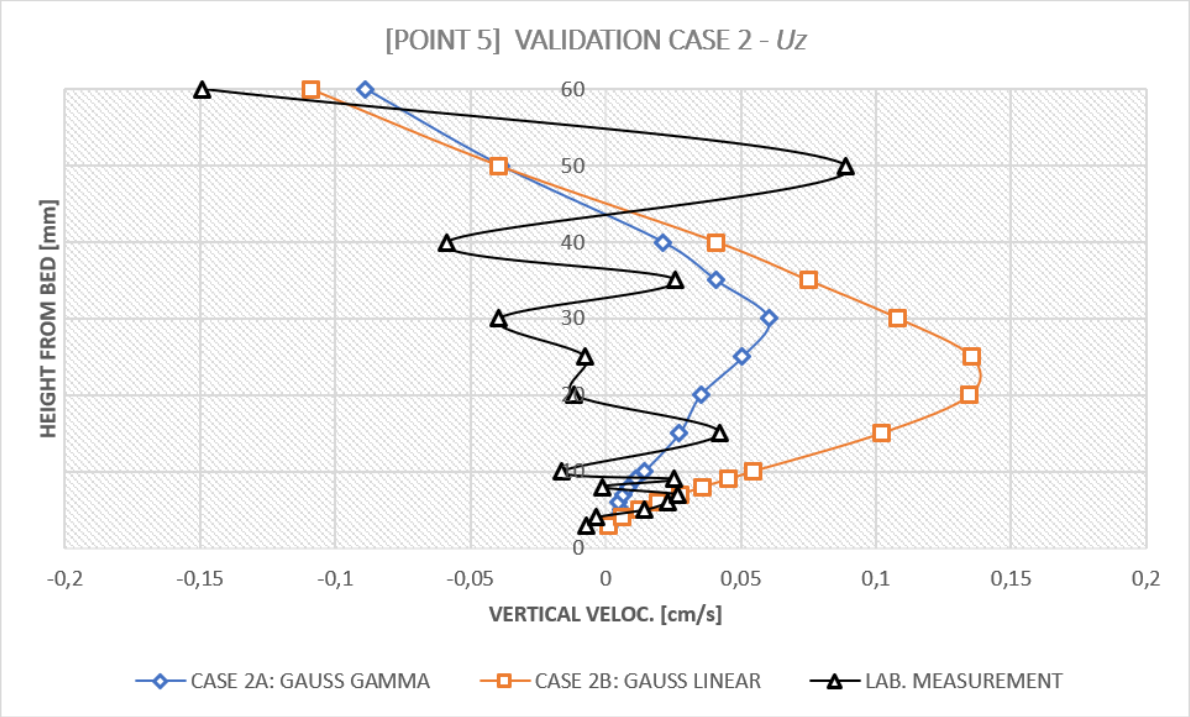

Figure 6.24: Flow velocities validation of simulation Case 2 at Point 5

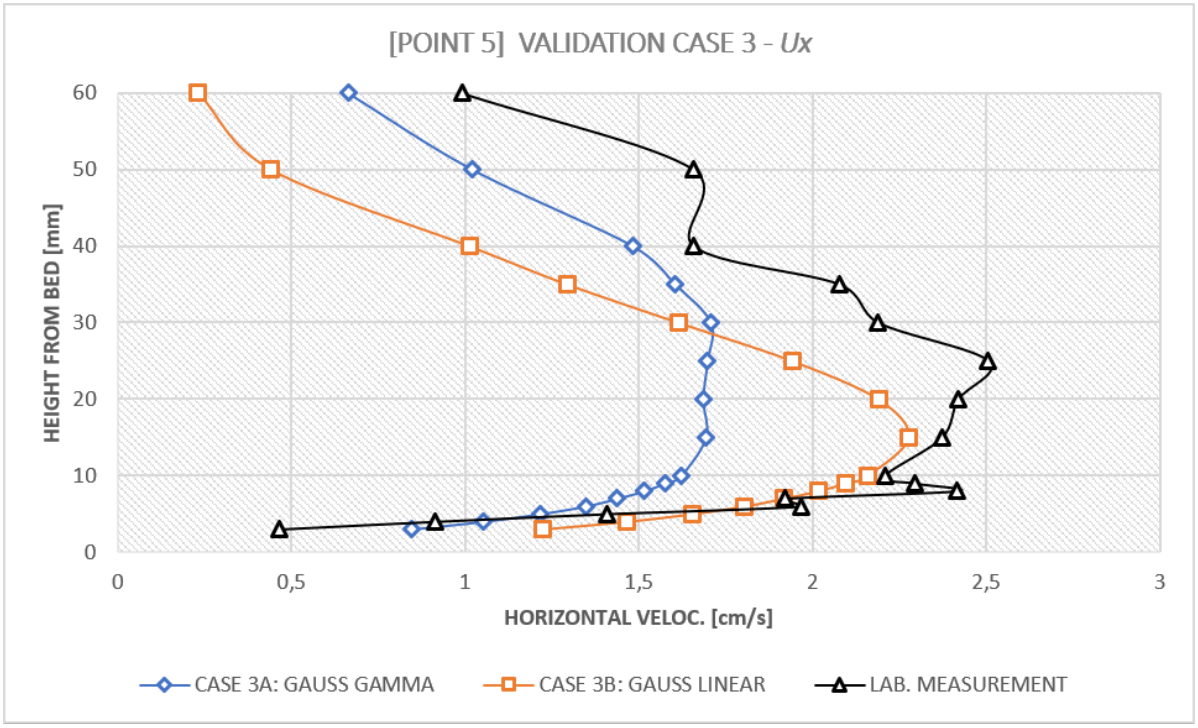

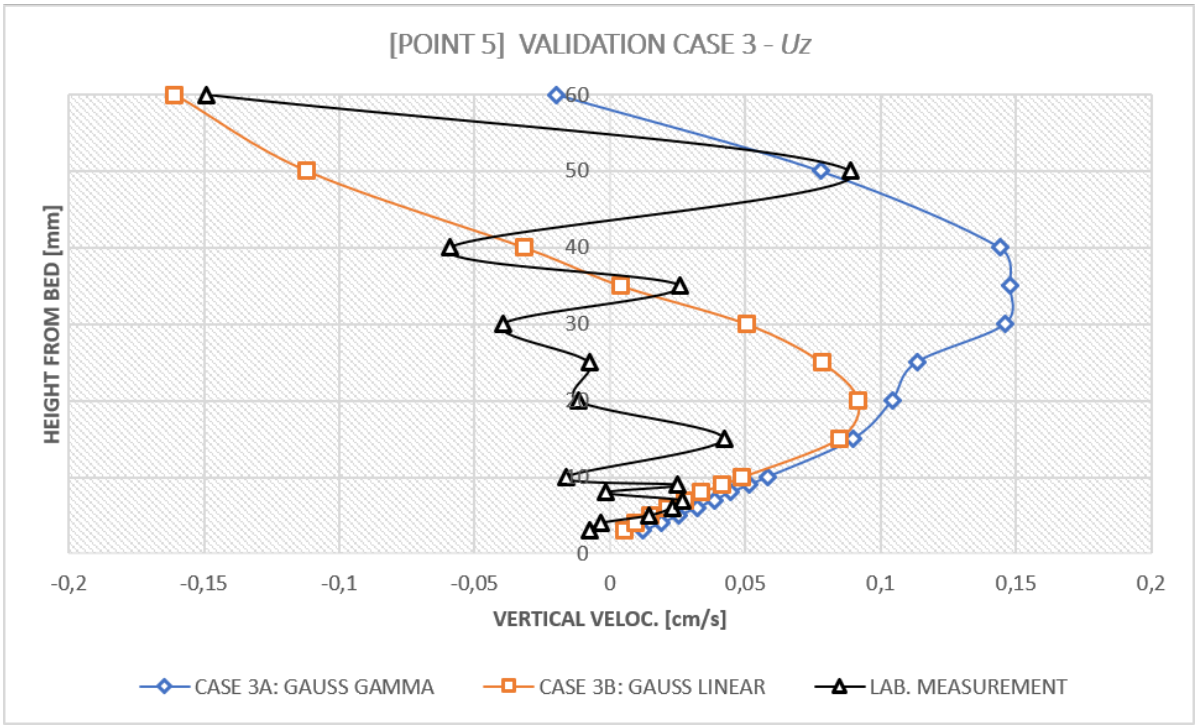

Figure 6.25: Flow velocities validation of simulation Case 3 at Point 5

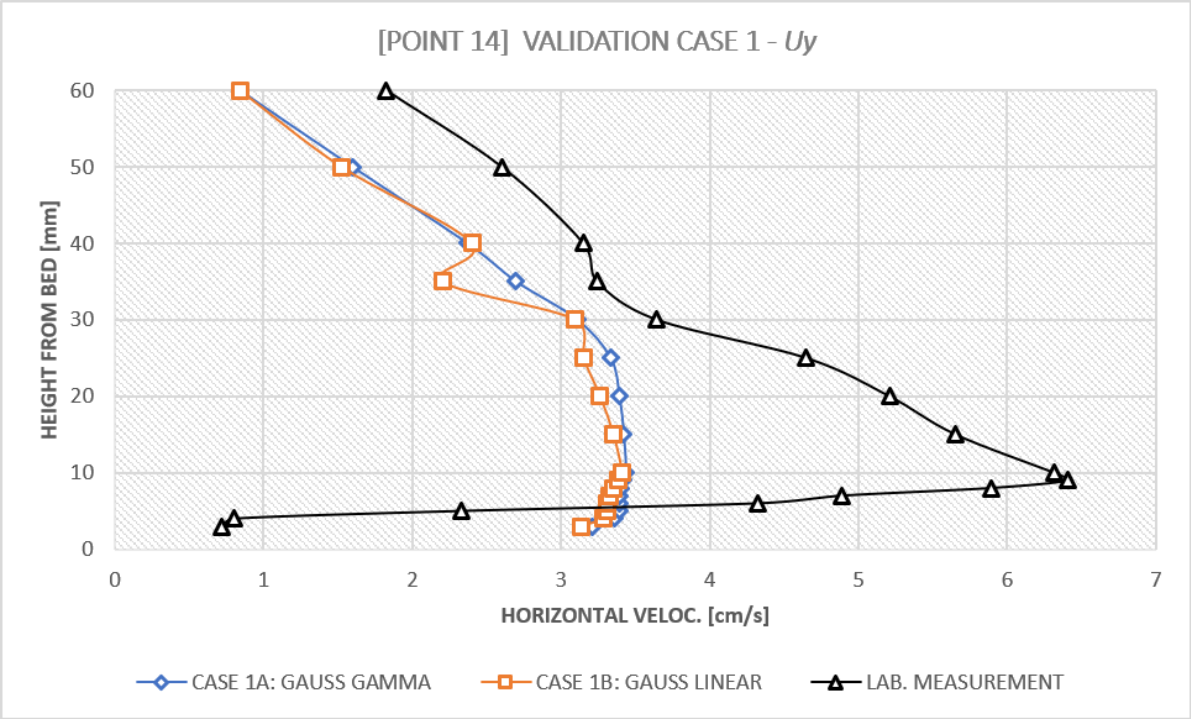

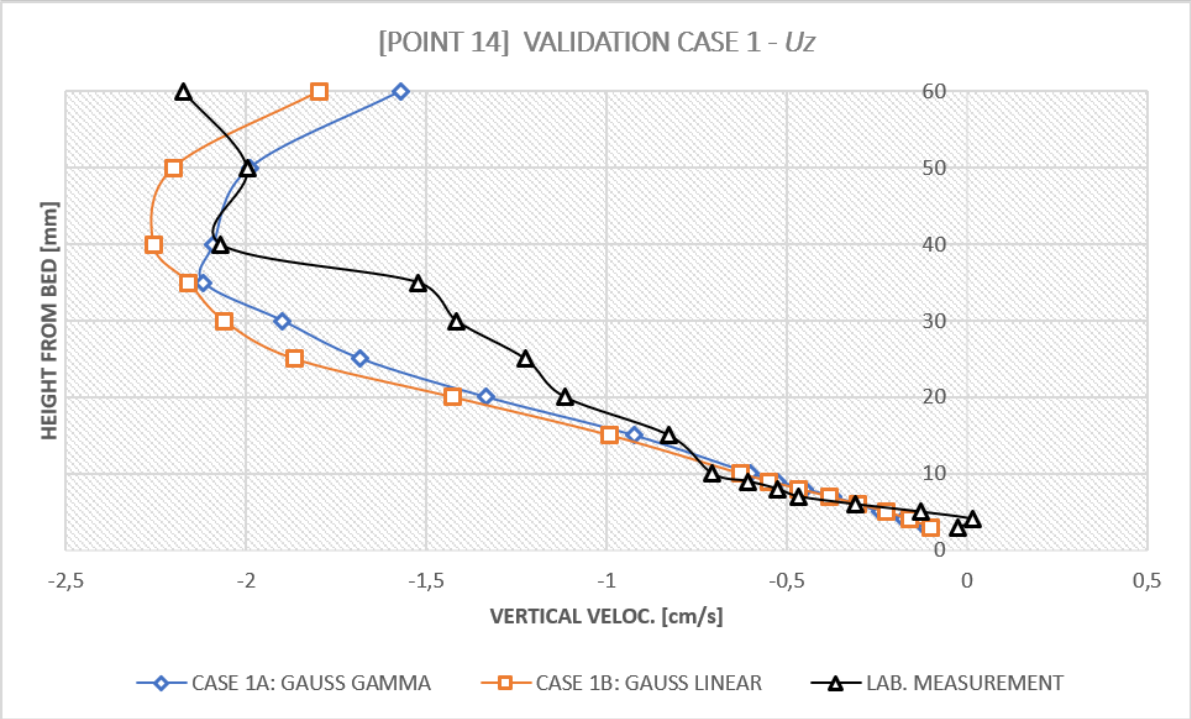

Figure 6.26: Flow velocities validation of simulation Case 1 at Point 14

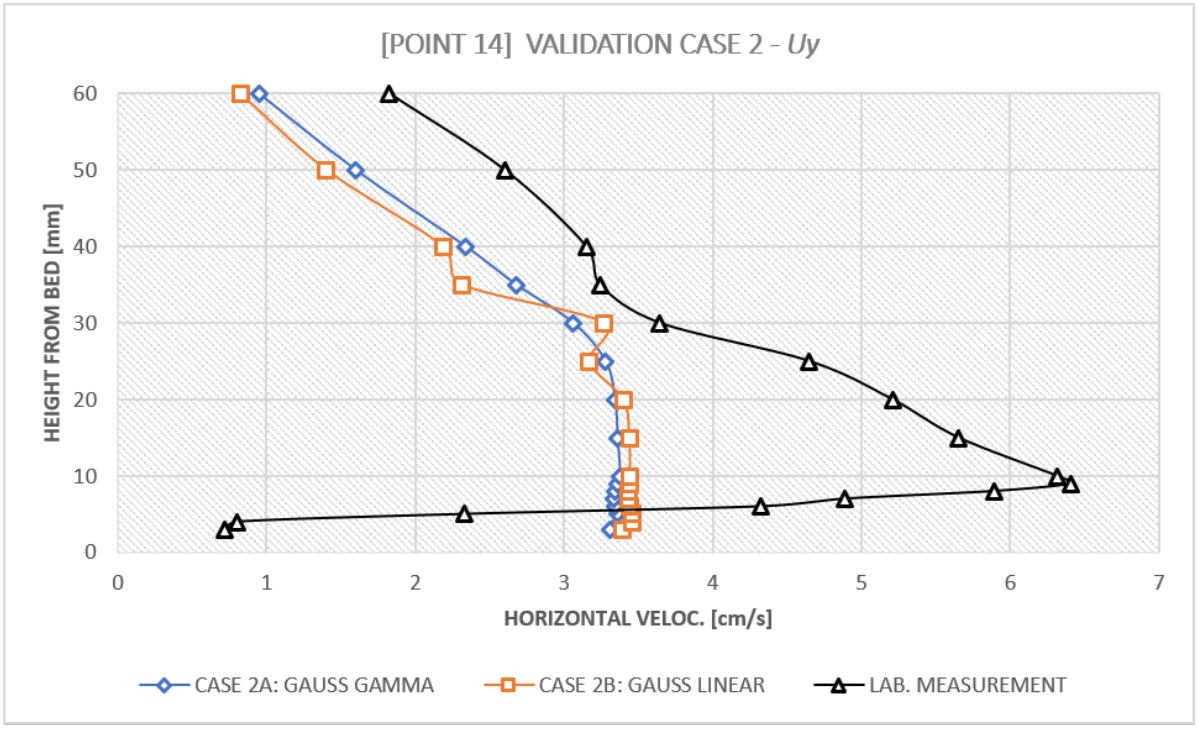

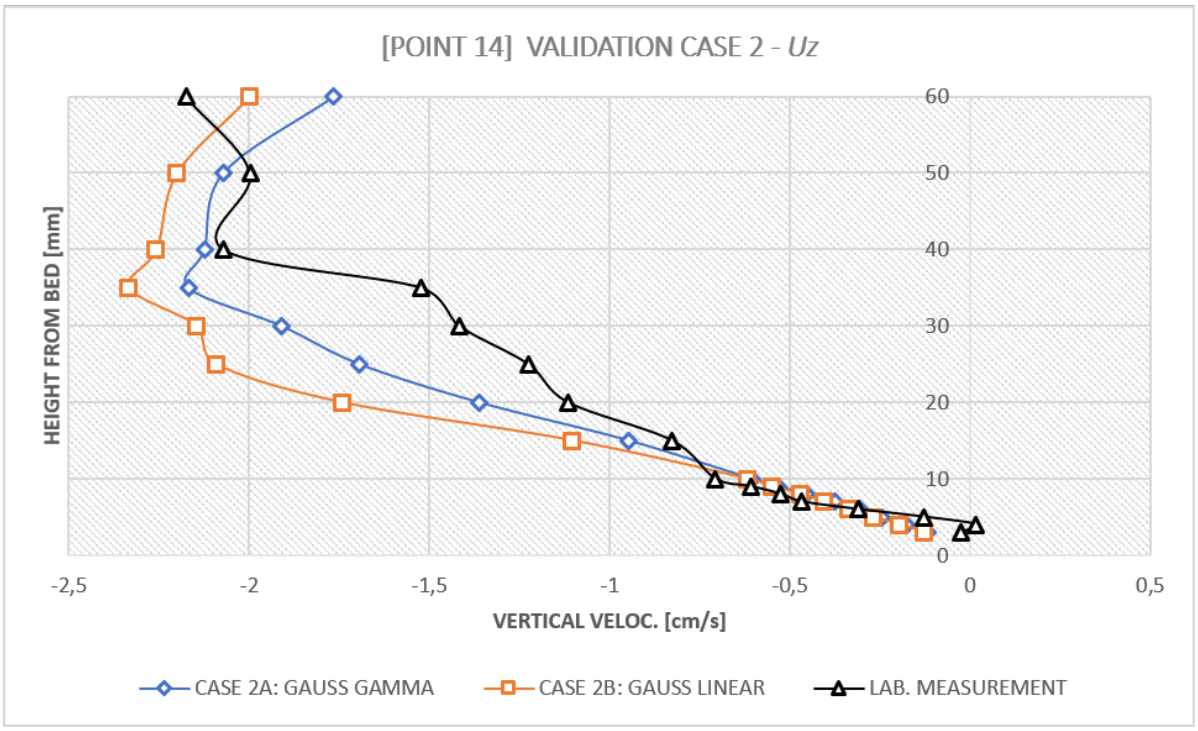

Figure 6.27: Flow velocities validation of simulation Case 2 at Point 14

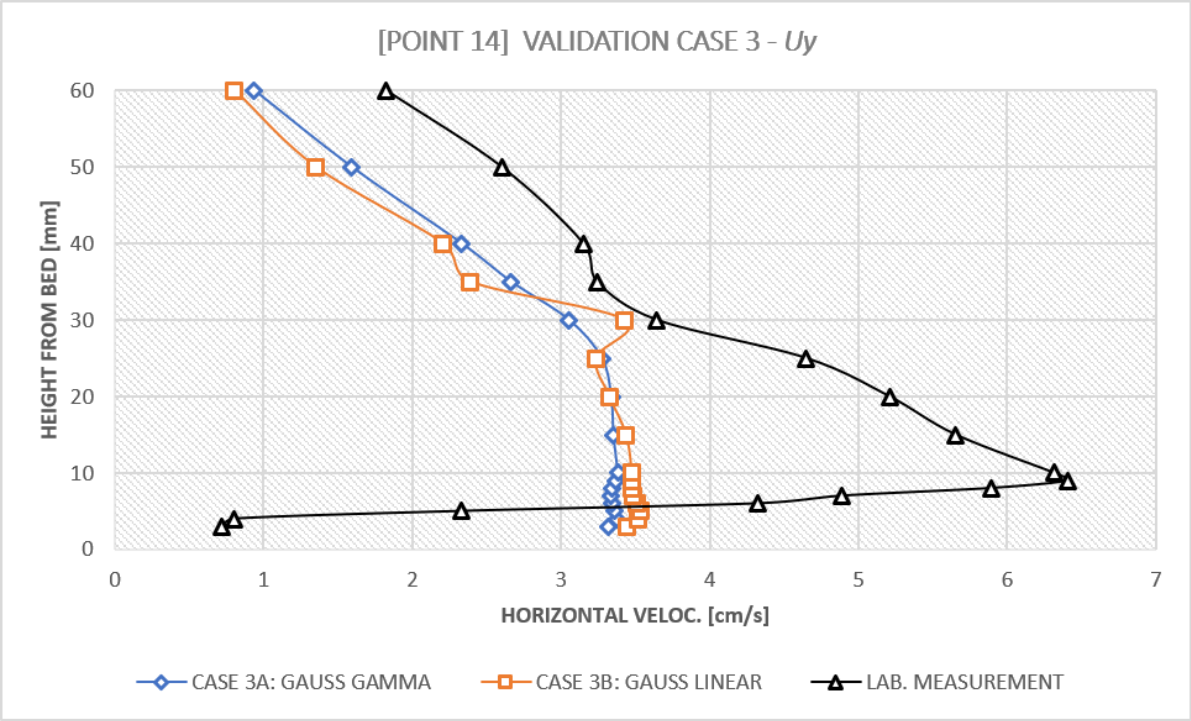

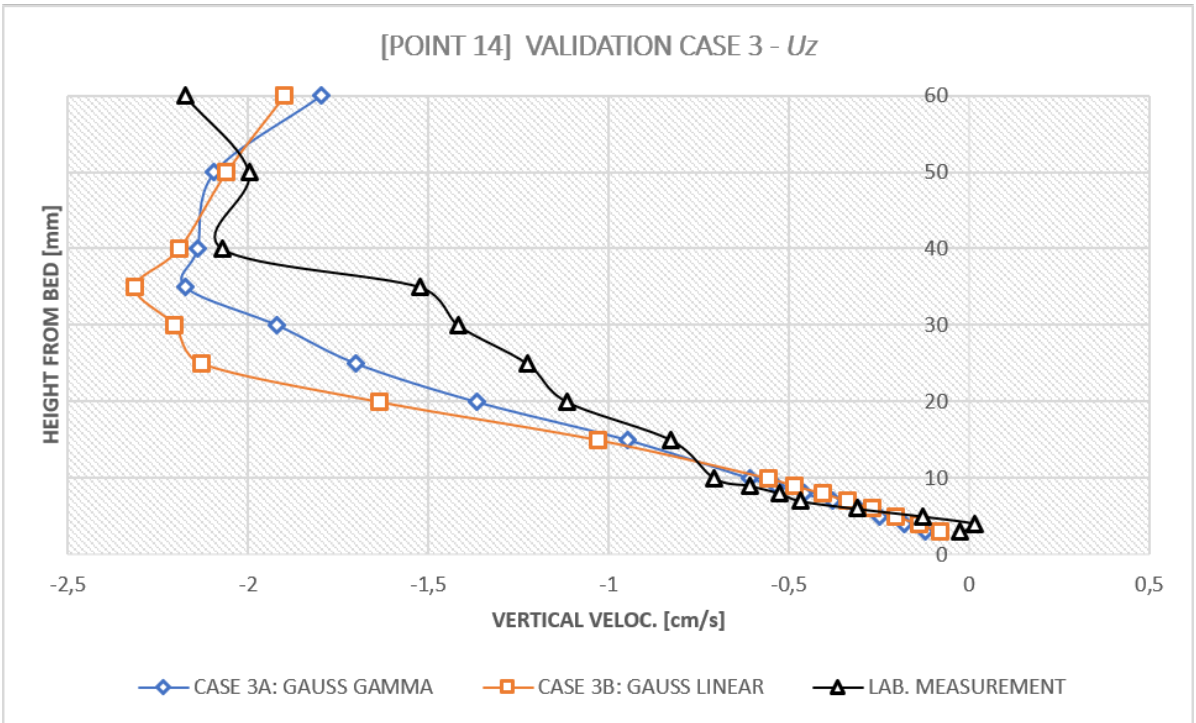

Figure 6.28: Flow velocities validation of simulation Case 3 at Point 14

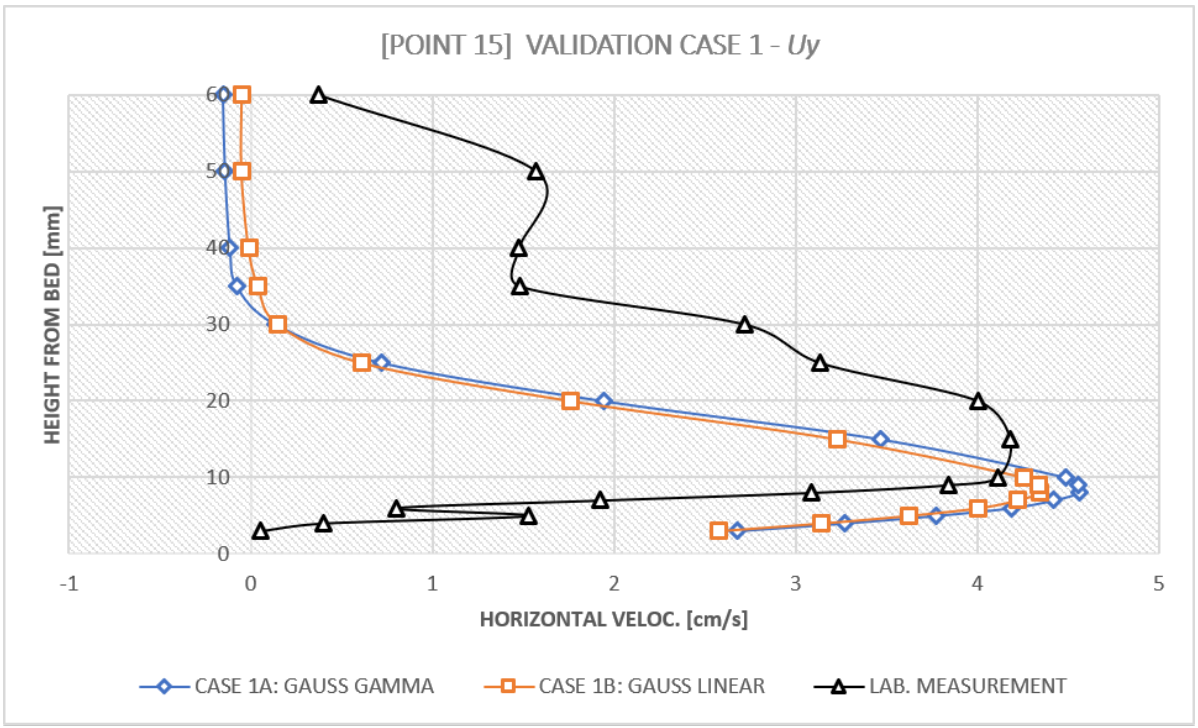

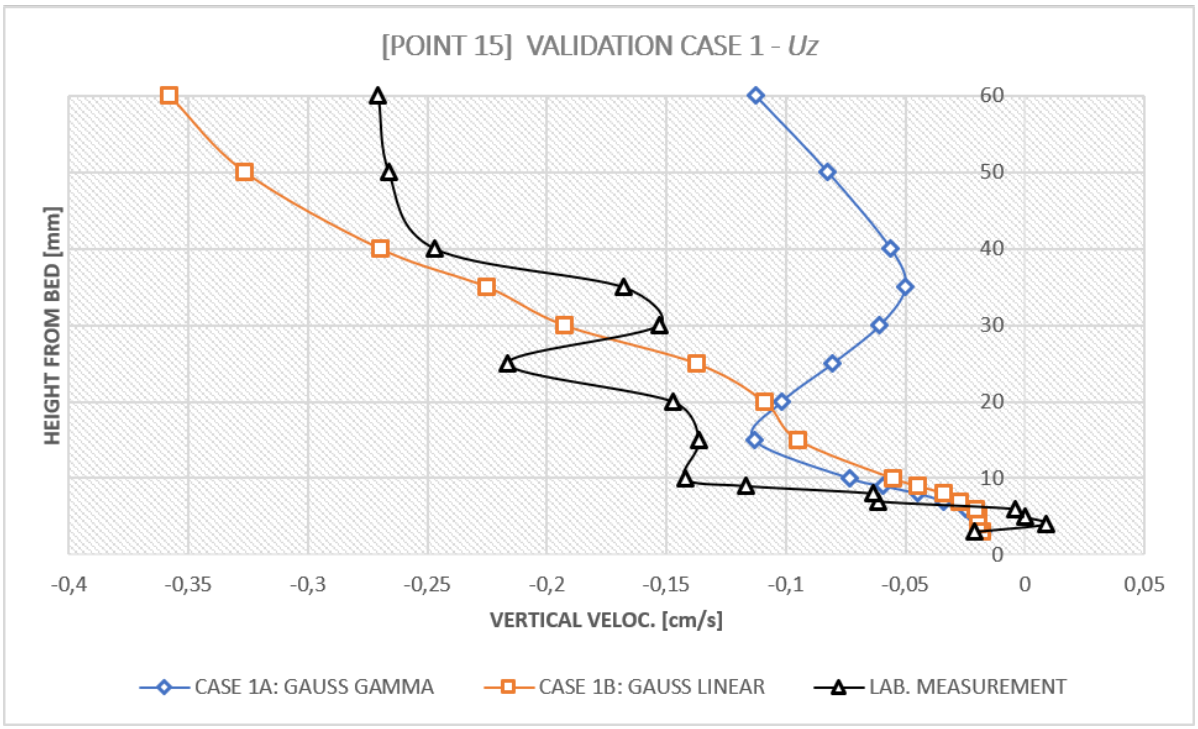

Figure 6.29: Flow velocities validation of simulation Case 1 at Point 15

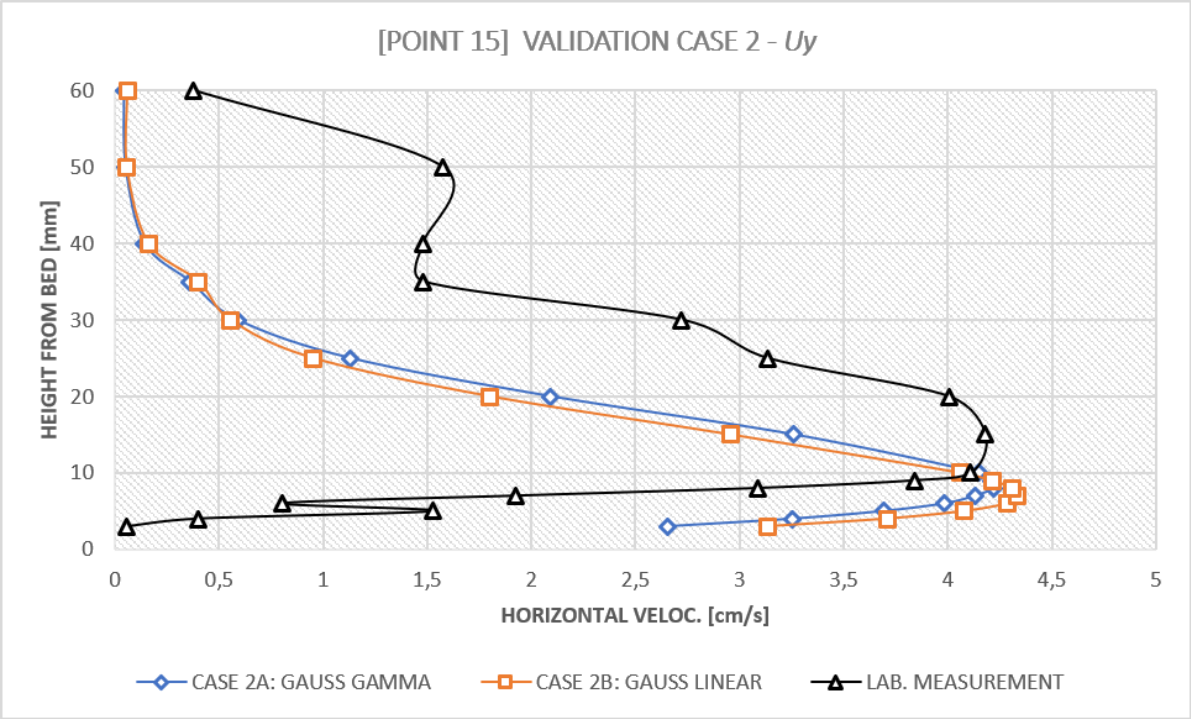

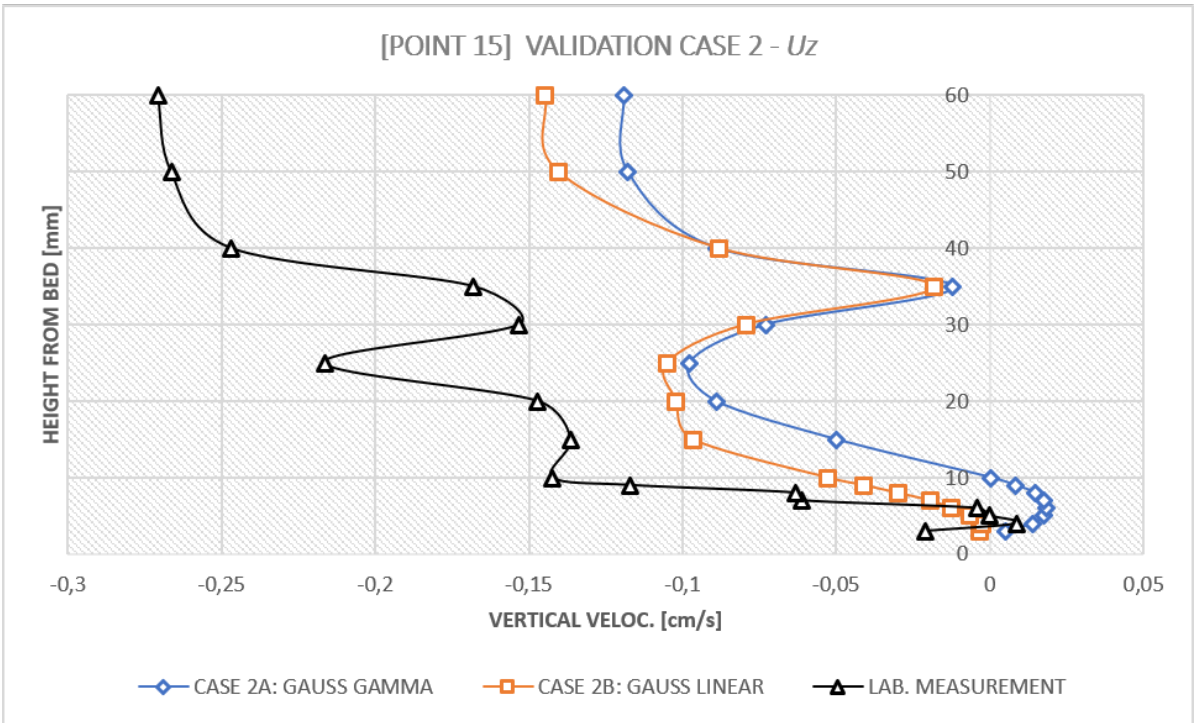

Figure 6.30: Flow velocities validation of simulation Case 2 at Point 15

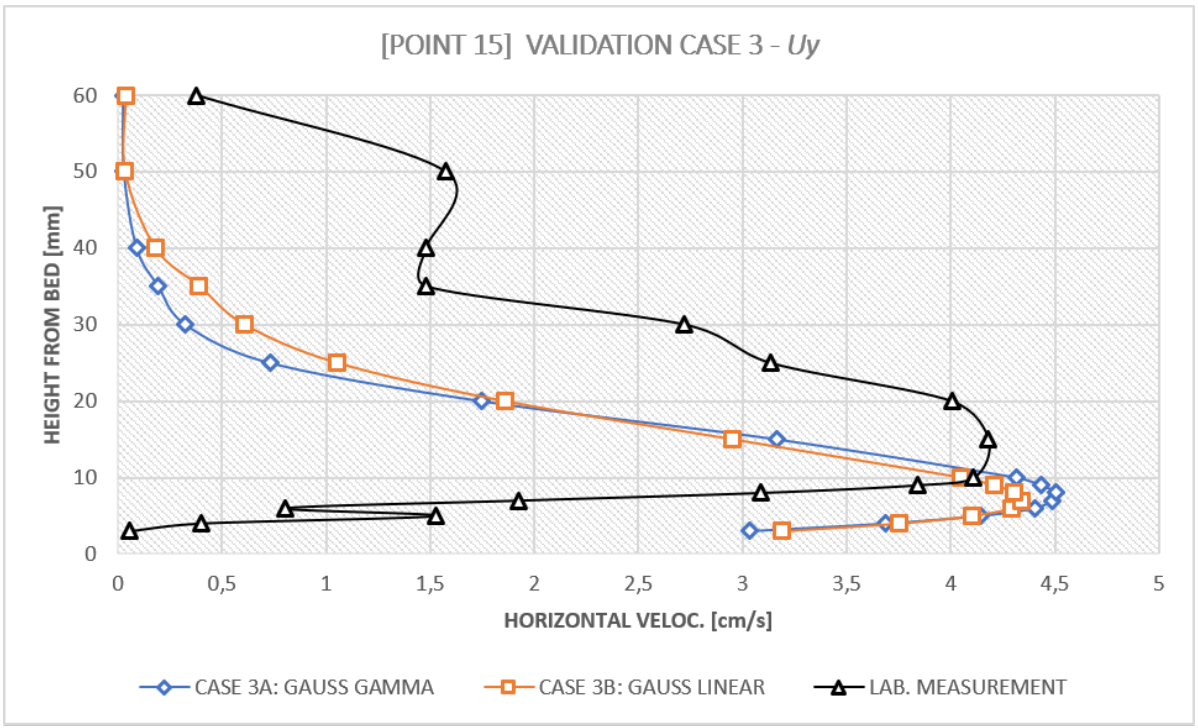

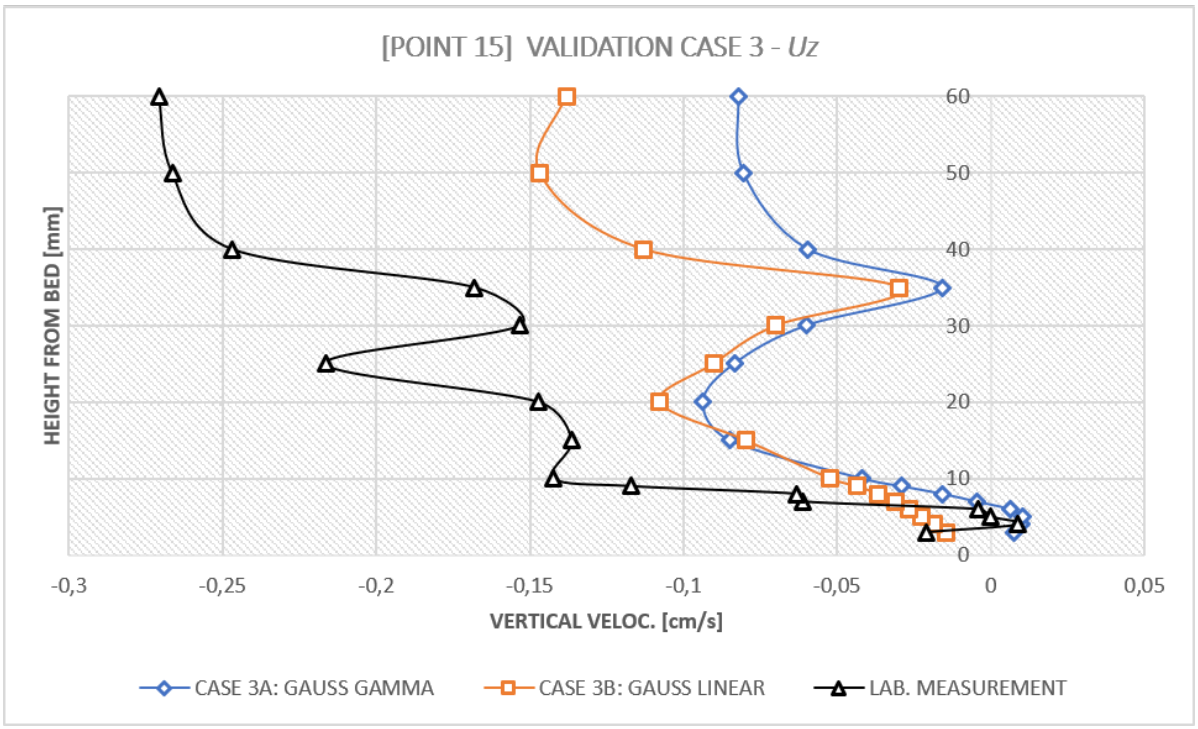

Figure 6.31: Flow velocities validation of simulation Case 3 at Point 15

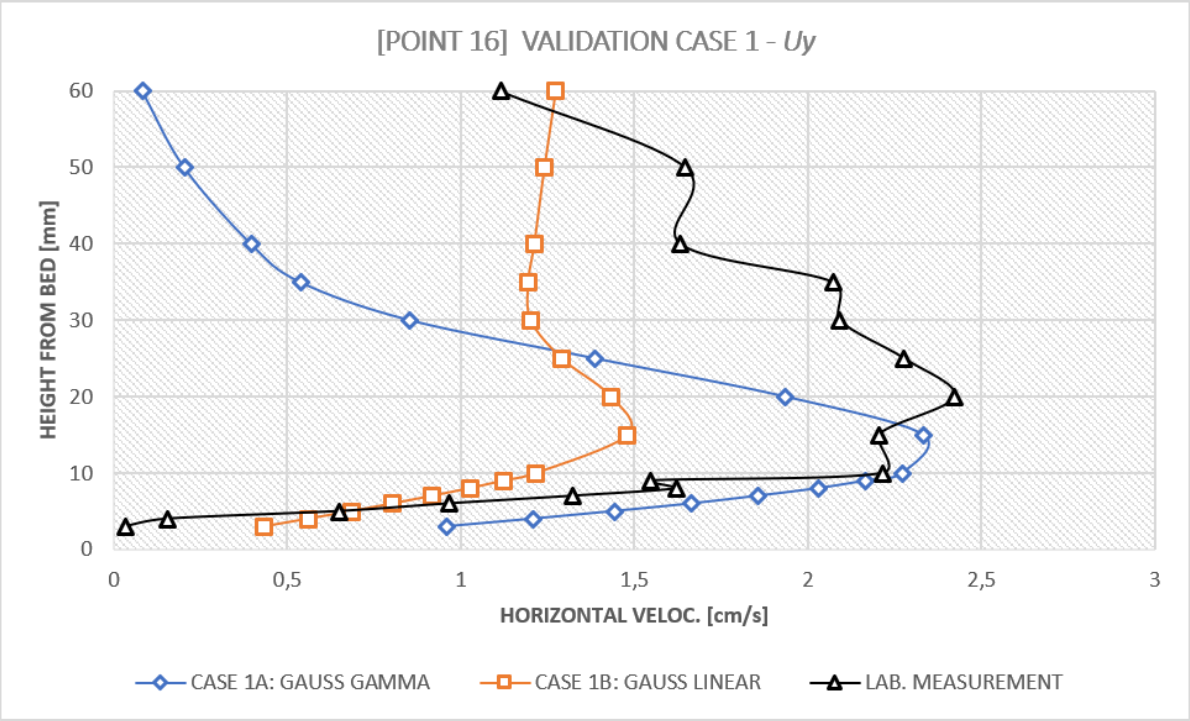

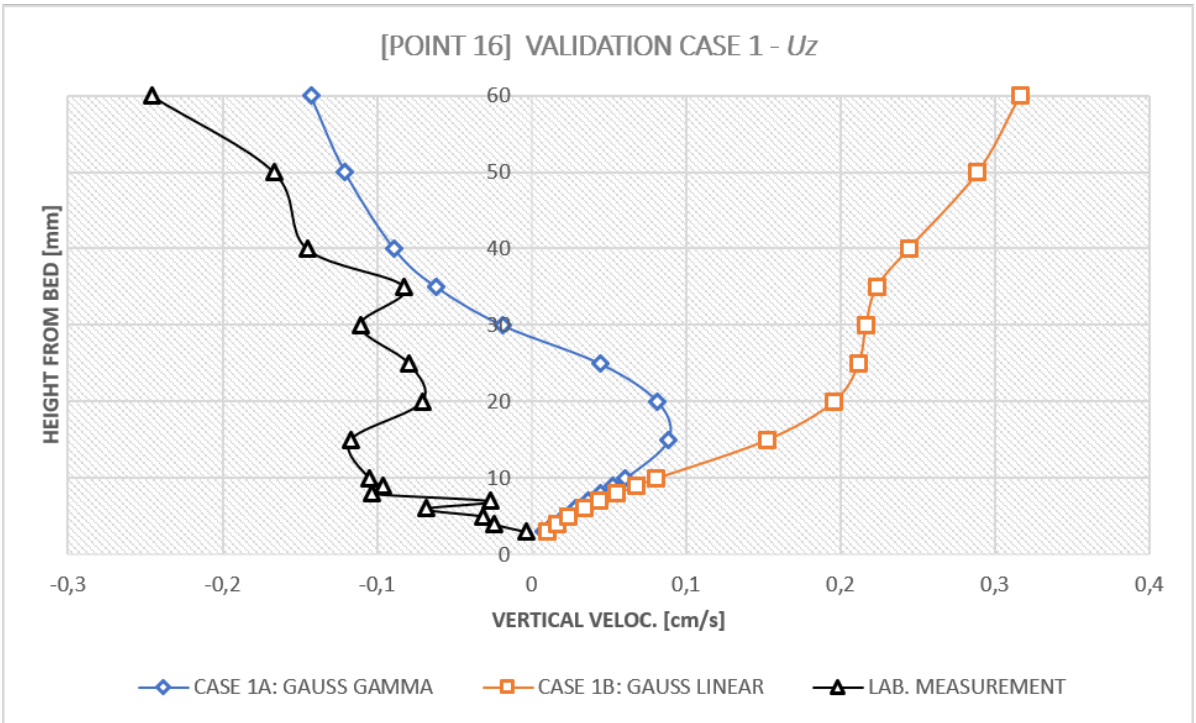

Figure 6.32: Flow velocities validation of simulation Case 1 at Point 16

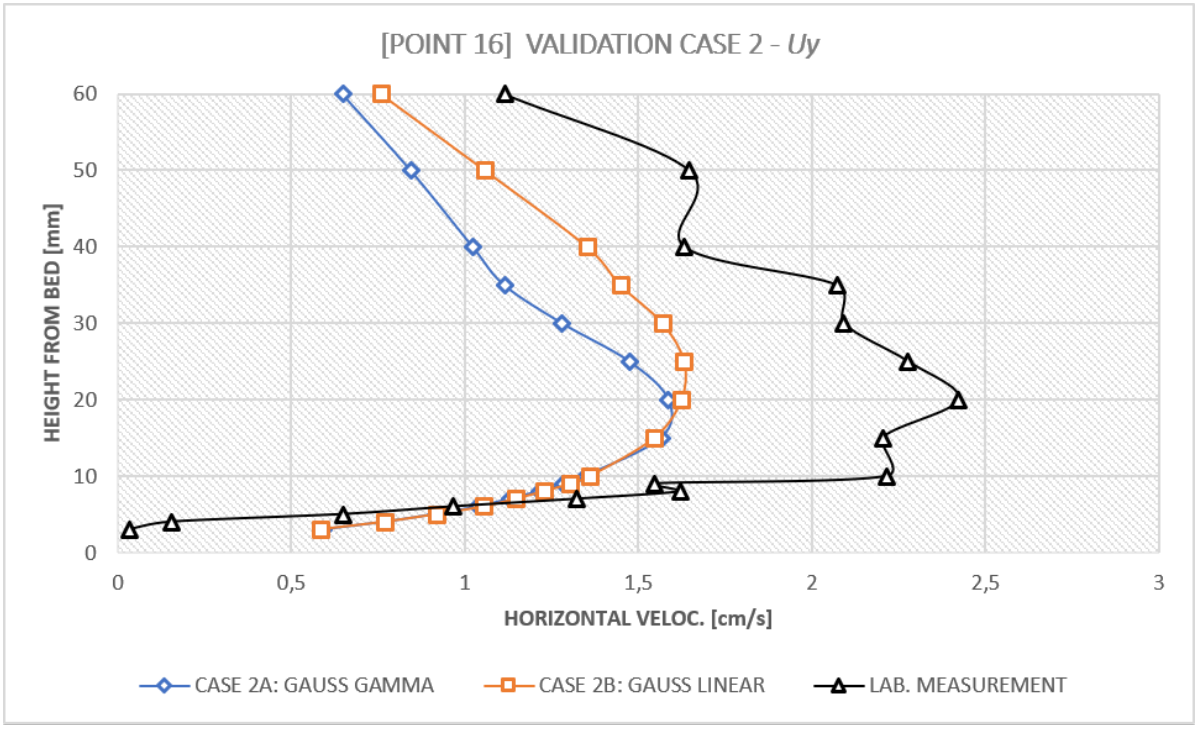

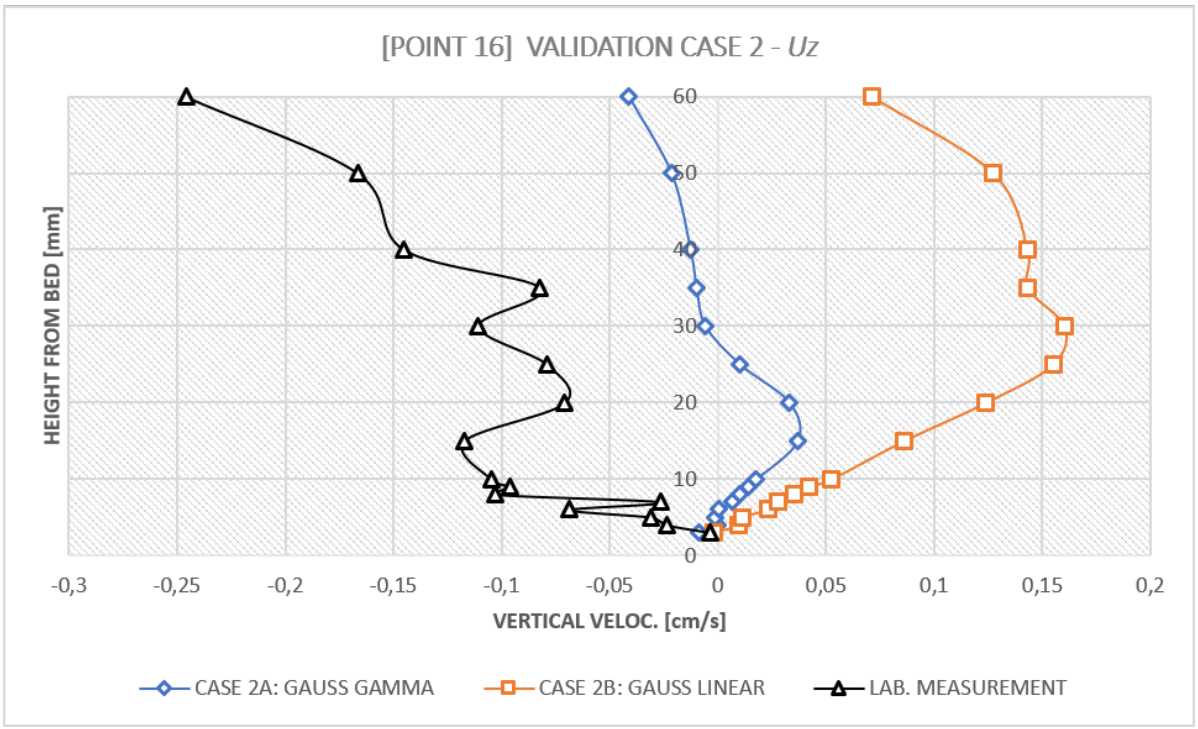

Figure 6.33: Flow velocities validation of simulation Case 2 at Point 16

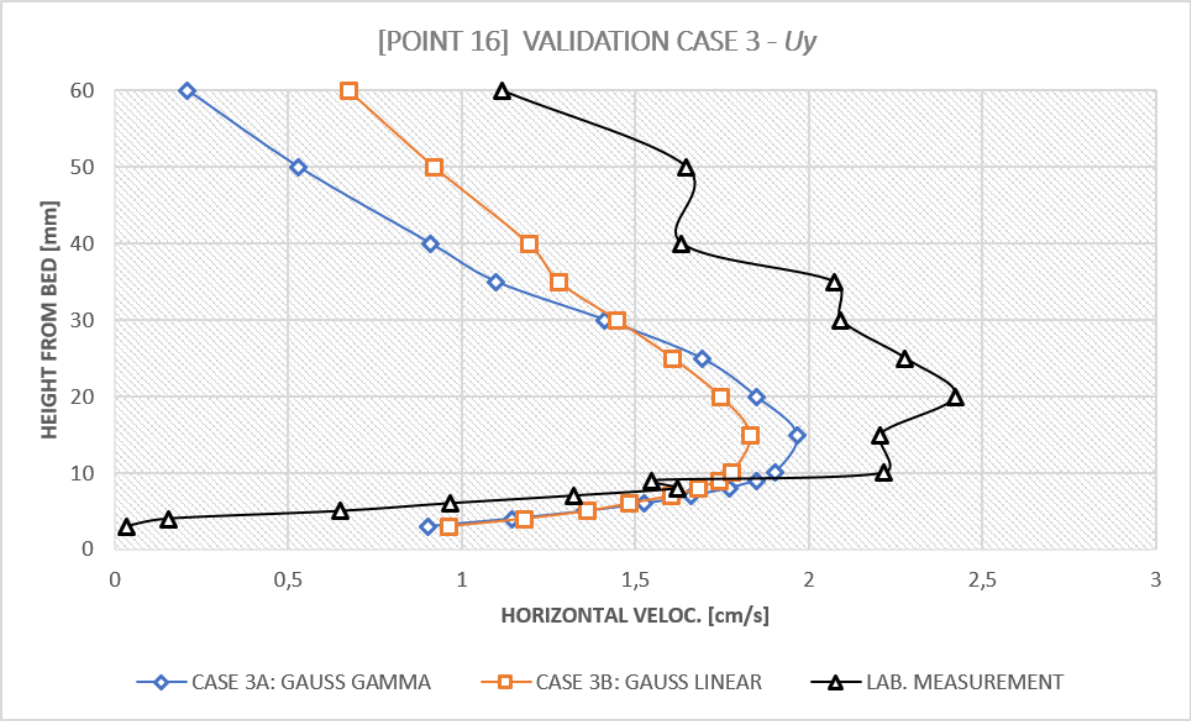

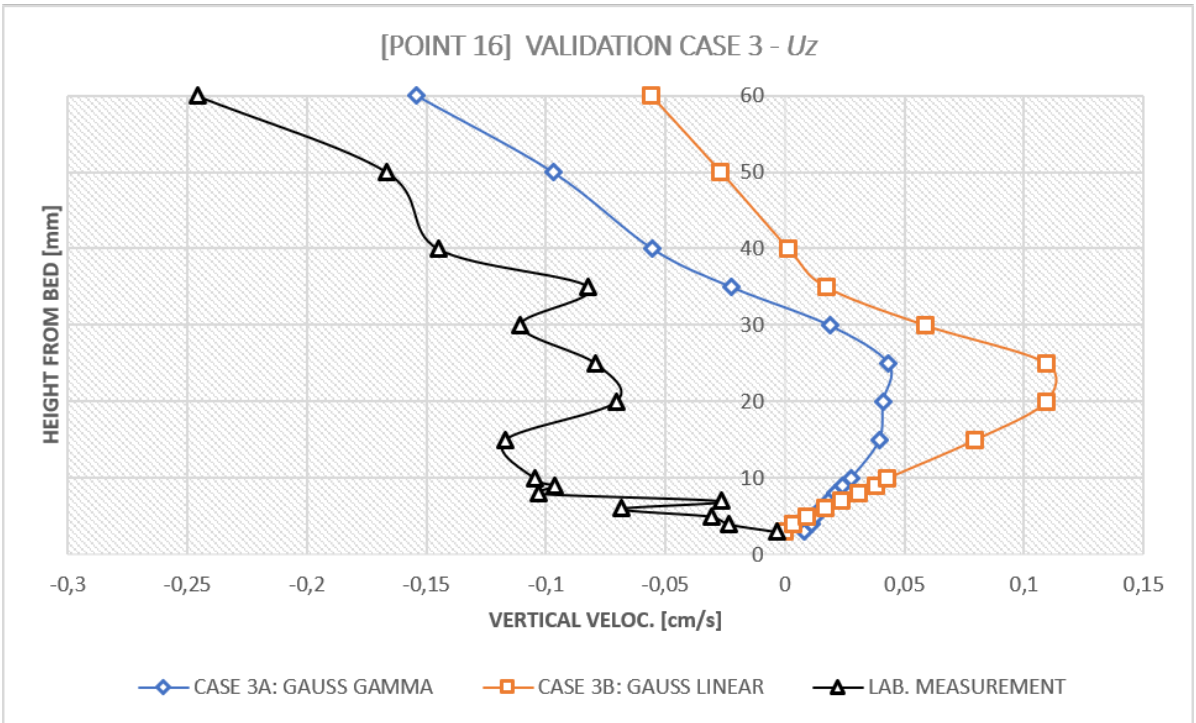

Figure 6.34: Flow velocities validation of simulation Case 3 at Point 16

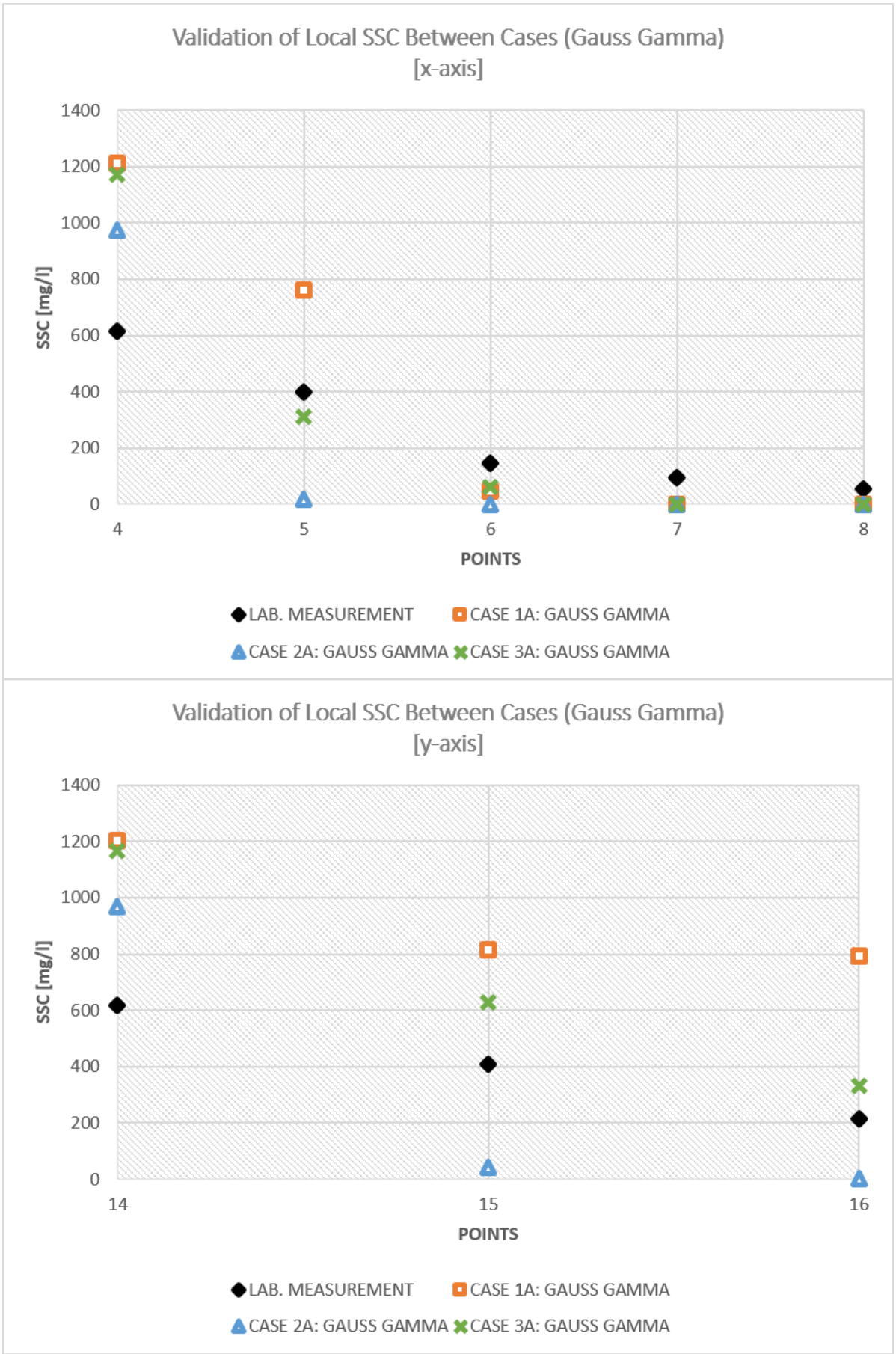

Figure 6.35: Validation of SSC for cases with Gauss Gamma differencing scheme

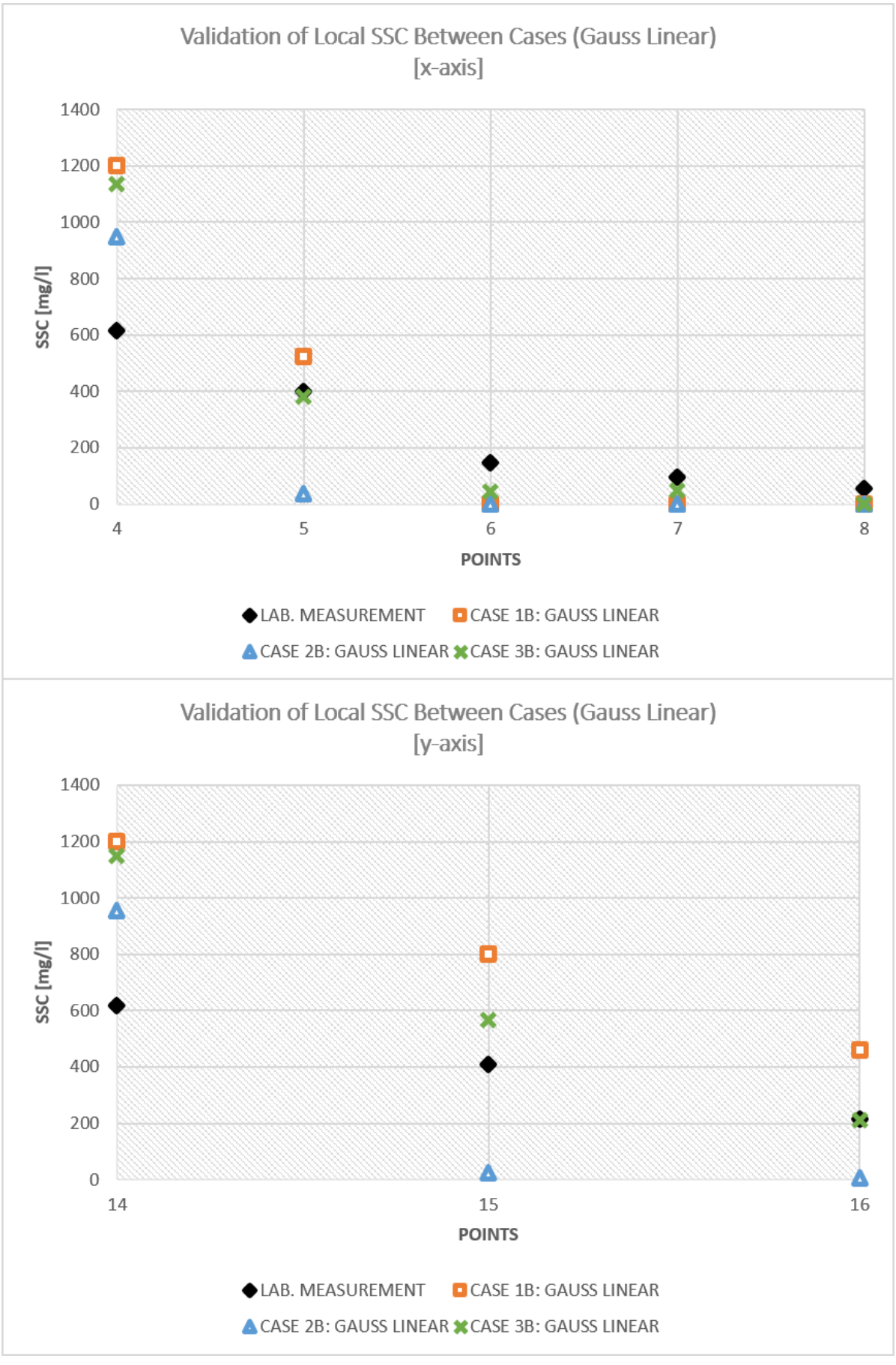

Figure 6.36: Validation of SSC for cases with Gauss Linear differencing scheme

7

Conclusions and Recommendations

7.1. Conclusions

Some conclusions can be taken in this study:

- Simulating tailings flow using the drift-flux model, LES turbulent model, non-orthogonal mesh, and particle diameter of d_{50} gives a proper estimation of the tailings SSC. Meanwhile, simulation without solids settling results in overestimation of the simulated SSC and simulation with extreme value of solids settling results in underestimation of the simulated SSC.
- Gauss Gamma differencing scheme with γ value of 0.1 turns out are giving too bounded solutions for the sake of stability. Hence, the expected resolution and physics of the simulated flow can not be seen when Gauss Gamma differencing scheme is implemented. Meanwhile more turbulent structures can be seen when Gauss Linear differencing scheme is implemented.
- Top-hat approach for the buoyant-jet inlet results in a simplification of the simulated tailings flow. Hence the expected entrainment and mixing throughout the jet stream does not occur, and uniform profile of the core of the tailings flow turns out to be observed.
- In this study, the solids settling is implemented by using monosize fraction assumption and assigning the settling velocity as the relative velocity of the phase. Thus a proper consideration of the implemented particle diameter is crucial in representing the wanted settling rate since the practical tailings mixture consists of multisize fractions.
- The simulated suspended-solids in the water column is not only affected by the implemented settling rate through settling-velocity, but also the differentiation schemes used for numerically solving the governing equations.
- Implementing solids settling function without pick-up or erosion function leads to hyper-concentration of solids in the cells near the tabletop boundary as the settled solids are not able to re-suspend into the water column. Hence with a constant influx of solids concentration and settling rate, more solids are settling and concentrating to the bottom.

7.2. Recommendations

For future research and developments, some recommendations can be formulated from this research, such as:

- It is recommended to further the research by simulating using the original domain and the original inlet pipe to include all the necessary physics, in case there is enough computational performance available.
- It is recommended to also simulate further by implementing higher resolutions near the tabletop, especially around Point 4, where the jet-momentum still dominates the flow.
- It is recommended to further the research by observing the implementation of the Gauss linear differencing scheme using non-orthogonal correction, especially since the non-orthogonality of the mesh is high.
- Since it is observed that the simulation domain gives stable results using Gauss linear differencing scheme, it is recommended to further the simulation using Gauss linear differencing scheme.
- As tailings mixtures practically consist of multisize solid fractions, it is recommended to further the research for enabling the implementation of multisize solid fractions in the simulated mixture. Thus resulting in a more proper physics interpretation in the numerical simulation.
- It is recommended to not only implementing solids settling function during the simulation of the tailings mixture, but also the pick-up function. Thus it is also recommended to further the research by investigating the effect of implementing pick-up function to the drift-flux model to observe whether the expected physics can be numerically simulated or not.
- It is recommended to investigate the effect of solids settling with a settling-velocity model other than the Richardson-Zaki relative-velocity model (e.g. see Brennan (2001)), as the Richardson-Zaki relative-velocity model is meant for calculating the settling rate of solids particle in a still fluid. Meanwhile the observed flow phenomena are transient.

A

Appendix

A.1. Derivation of Drift-Flux Governing Equations

By using drift-flux approach, the observed liquids are seen to be consisted of two phases: continuous-phase and dispersed-phase. Each of this phase is considered as continuum. Thus the obligation to describe each particle motion in the observed fluids is neglected. This condition includes as well if there are solids fraction in the mixture. The solids fraction is seen as continuum which particles are assumed to uniformly fill the whole fraction volume. By using drift-flux approach, the continuity equation for each phase are added together to yield a mixture continuity equation, and the momentum equations are added to yield a single mixture momentum equation (Brennan, 2001). In this section, the derivation of the flow governing equations follows the derivation of Brennan (2001).

A.1.1. Variable Definitions in Drift-Flux Model

In the derivation of flow governing equations using drift-flux approach, some variables need to be defined first.

Since all phases in the flow are seen as continuum in drift-flux approach, the average amount of volume filled by a certain phase k in the mixture (α_k) can be defined as the ratio between the volume occupied by the phase k and the total volume V_o.

$$\alpha_k = \frac{V_k}{V_o} \tag{A.1}$$

The identity of this volumetric concentration is that the summation of the volumetic concentration of all phases should equal as 1.

$$\alpha_1 + \alpha_2 = 1 \tag{A.2}$$

The mixture density is defined as the summation of each phase-density times its volumetric concentration.

$$\rho_m = \alpha_1 \rho_1 + \alpha_2 \rho_2 \tag{A.3}$$

The same approach is used as well for defining the mixture pressure:

$$P_m = \alpha_1 P_1 + \alpha_2 P_2 \tag{A.4}$$

Where $P_{1,2}$ represents the pressure of each phase in the mixture. The velocity of the mixture ($\mathbf{v}_m$) is defined by calculating the velocity at the center of the mass of the mixture.

$$\mathbf{v}_m = \frac{\alpha_1 \rho_1 \mathbf{v}_1 + \alpha_2 \rho_2 \mathbf{v}_2}{\rho_m} \tag{A.5}$$

Where $\mathbf{v}_{1,2}$ represents each phase-velocity. The relative velocity ($\mathbf{v}_r$) is defined as the difference between each phase velocity.

$$\mathbf{v}_r = \mathbf{v}_1 - \mathbf{v}_2 \tag{A.6}$$

Ishii and Hibiki (2010) then defined following identities:

$$\mathbf{v}_1 = \mathbf{v}_{1m} + \mathbf{v}_m \tag{A.7}$$

$$\alpha_1 \rho_1 \mathbf{v}_{1m} + \alpha_2 \rho_2 \mathbf{v}_{2m} = 0 \tag{A.8}$$

$$\alpha_1 \rho_1 \mathbf{v}_1 + \alpha_2 \rho_2 \mathbf{v}_2 = \rho_m \mathbf{v}_m \tag{A.9}$$

A.1.2. Mixture Continuity Equation

The derivation of the mixture continuity equation starts by defining the continuity constraint for each phase in the mixture. The continuity equations for each phase in the mixture are defined as:

$$\frac{\partial \alpha_1 \rho_1}{\partial t} + \nabla \cdot \alpha_1 \rho_1 \mathbf{v}_1 = 0 \tag{A.10}$$

$$\frac{\partial \alpha_2 \rho_2}{\partial t} + \nabla \cdot \alpha_2 \rho_2 \mathbf{v}_2 = 0 \tag{A.11}$$

Where subscripts $1,2$ denotes for each phase in the mixture. Summing both continuity constraints (Equation A.10 and A.11) results in:

$$\frac{\partial (\alpha_1 \rho_1 + \alpha_2 \rho_2)}{\partial t} + \nabla \cdot \left(\alpha_1 \rho_1 \mathbf{v}_1 + \alpha_2 \rho_2 \mathbf{v}_2\right) = 0 \tag{A.12}$$

Using the variable definitions in Equation A.3, A.7, and A.8, the second-term at Left-Hand Side (LHS) in Equation A.12 becomes:

$$\alpha_1 \rho_1 \mathbf{v}_1 + \alpha_2 \rho_2 \mathbf{v}_2 = \alpha_1 \rho_1 \mathbf{v}_m + \alpha_2 \rho_2 \mathbf{v}_m + \alpha_1 \rho_1 \mathbf{v}_{1m} + \alpha_2 \rho_2 \mathbf{v}_{2m} \tag{A.13}$$

Where $\mathbf{v}_{1m}$ and $\mathbf{v}_{2m}$ represents the velocity of phase 1,2 relative to the mixture center of mass velocity. Thus, using the identity in Equation A.9 , the following form is obtained:

$$\alpha_1 \rho_1 \mathbf{v}_1 + \alpha_2 \rho_2 \mathbf{v}_2 = \left(\alpha_1 \rho_1 + \alpha_2 \rho_2\right) \mathbf{v}_m \tag{A.14}$$

Therefore **the mixture continuity equation** is defined as:

$$\frac{\partial \rho_m}{\partial t} + \nabla \cdot (\rho_m . \mathbf{v}_m) = 0 \tag{A.15}$$

A.1.3. Mixture Momentum Equation

Since drift-flux uses continuum assumption, the motion of all phases in the mixture are consequently able to be described by Navier-Stokes equations. Therefore the momentum equation for each phase is:

$$\frac{\partial \alpha_k \rho_k \mathbf{v}_k}{\partial t} + \nabla \cdot (\alpha_k \rho_k \mathbf{v}_k \mathbf{v}_k) = -\nabla \alpha_k P_k + \nabla \cdot (\alpha_k \mathbf{T}_k + \alpha_k \mathbf{T}_k^t) + \alpha_k \rho_k \mathbf{g}_k + \alpha_k \mathbf{m}_k \tag{A.16}$$

Where $\mathbf{T}_k$ and $\mathbf{T}_k^t$ are tensors counting for viscous and turbulent stresses of the phase, $\mathbf{m}_k$ is the source term representing the interacting force between each phase, P_k is the phase pressure, and $\mathbf{g}_k$ is the gravitational-acceleration vector experienced by each phase. Since the number of the observed phases are 2, and using the definition of mixture density and velocity in Equation A.9, the following form for the mixture temporal derivative (first term on LHS of Equation A.16) is obtained:

$$\frac{\partial \alpha_1 \rho_1 \mathbf{v}_1}{\partial t} + \frac{\partial \alpha_2 \rho_2 \mathbf{v}_2}{\partial t} = \frac{\partial \rho_m \mathbf{v}_m}{\partial t} \tag{A.17}$$

For the pressure gradient (first term on RHS of Equation A.16), the mixture pressure gradient term is defined as:

$$\alpha_1 P_1 + \alpha_2 P_2 = P_m \tag{A.18}$$

For the mixture convective term, each phase convective-term is summed while using definition in Equation A.7 and A.8:

$$\alpha_1 \rho_1 \mathbf{v}_1 \mathbf{v}_1 + \alpha_2 \rho_2 \mathbf{v}_2 \mathbf{v}_2 = \alpha_1 \rho_1 \left[\mathbf{v}_{1m}^2 + 2\mathbf{v}_{1m}\mathbf{v}_m + \mathbf{v}_m^2\right] + \alpha_2 \rho_2 \left[\mathbf{v}_{2m}^2 + 2\mathbf{v}_{2m}\mathbf{v}_m + \mathbf{v}_m^2\right] \tag{A.19}$$

Rearranging gives:

$$\alpha_1 \rho_1 \mathbf{v}_1 \mathbf{v}_1 + \alpha_2 \rho_2 \mathbf{v}_2 \mathbf{v}_2 = \alpha_1 \rho_1 \mathbf{v}_{1m}^2 + \alpha_2 \rho_2 \mathbf{v}_{2m}^2 + 2\left[\alpha_1 \rho_1 \mathbf{v}_{1m} + \alpha_2 \rho_2 \mathbf{v}_{2m}\right]\mathbf{v}_m + \left[\alpha_1 \rho_1 + \alpha_2 \rho_2\right]\mathbf{v}_m^2 \tag{A.20}$$

Then, using the definition in Equation A.8, the following form is obtained for the mixture convective term:

$$\alpha_1 \rho_1 \mathbf{v}_1 \mathbf{v}_1 + \alpha_2 \rho_2 \mathbf{v}_2 \mathbf{v}_2 = \rho_m \mathbf{v}_m \mathbf{v}_m + \alpha_1 \rho_1 \mathbf{v}_{1m} \mathbf{v}_{1m} + \alpha_2 \rho_2 \mathbf{v}_{2m} \mathbf{v}_{2m} \tag{A.21}$$

$$= \rho_m \mathbf{v}_m \mathbf{v}_m + \sum_k \alpha_k \rho_k \mathbf{v}_{km} \mathbf{v}_{km} \tag{A.22}$$

Then, the mixture gravity term is obtained by summing as well each phase gravity term:

$$\alpha_1 \rho_1 \mathbf{g}_1 + \alpha_2 \rho_2 \mathbf{g}_2 = \rho_m \mathbf{g} \tag{A.23}$$

Arranging all the obtained terms results in **the mixture momentum equation**:

$$\frac{\partial \rho_m \mathbf{v}_m}{\partial t} + \nabla \cdot \left(\rho_m \mathbf{v}_m \mathbf{v}_m\right) = -\nabla P_m + \nabla \cdot \left[\mathbf{T} + \mathbf{T}^t - \sum_k \alpha_k \rho_k \mathbf{v}_{km} \mathbf{v}_{km}\right] + \rho_m \mathbf{g} \tag{A.24}$$

In drift-flux model, the mixture momentum equation can also be stated in the form of volumetric flux. Using the previous relation in Equation A.21 and the definitions in Equation A.8 and A.9 results in the following form:

$$\alpha_1 \rho_1 \mathbf{v}_{1m} \mathbf{v}_{1m} + \alpha_2 \rho_2 \mathbf{v}_{2m} \mathbf{v}_{2m} = \alpha_1 \rho_1 \left(\frac{\alpha_2}{\alpha_1} \frac{\rho_2}{\rho_m} \mathbf{v}_{2j}\right)^2 + \alpha_2 \rho_2 \left(\frac{\rho_1}{\rho_m} \mathbf{v}_{2j}\right)^2 \tag{A.25}$$

Rearranging results in the following form:

$$\alpha_1\rho_1\mathbf{v}_{1m}\mathbf{v}_{1m}+\alpha_2\rho_2\mathbf{v}_{2m}\mathbf{v}_{2m}=\frac{\alpha_2\rho_1\rho_2}{\rho_m^2}\mathbf{v}_{2j}^2\left[\frac{\alpha_2\rho_2}{\rho_1}+\rho_1\right] \tag{A.26}$$

Multiplying the ρ_1 term in the bracket with $\frac{\alpha_1}{\alpha_1}$:

$$\alpha_1\rho_1\mathbf{v}_{1m}\mathbf{v}_{1m}+\alpha_2\rho_2\mathbf{v}_{2m}\mathbf{v}_{2m}=\frac{\alpha_2\rho_1\rho_2}{\rho_m^2}\mathbf{v}_{2j}^2\left[\frac{\alpha_2\rho_2}{\rho_1}+\frac{\alpha_1\rho_1}{\alpha_1}\right] \tag{A.27}$$

Thus results in the following form:

$$\alpha_1\rho_1\mathbf{v}_{1m}\mathbf{v}_{1m}+\alpha_2\rho_2\mathbf{v}_{2m}\mathbf{v}_{2m}=\frac{\alpha_2}{(1-\alpha_2)}\frac{\rho_1\rho_2}{\rho_m}\mathbf{v}_{2j}^2 \tag{A.28}$$

By using Equation A.28, the following form of mixture momentum equation is obtained:

$$\frac{\partial\rho_m\mathbf{v}_m}{\partial t}+\nabla\cdot\left(\rho_m\mathbf{v}_m\mathbf{v}_m\right)=-\nabla P_m+\nabla\cdot\left[\mathbf{T}+\mathbf{T}^t\right]-\nabla\cdot\left[\frac{\alpha_d}{(1-\alpha_d)}\frac{\rho_c\rho_d}{\rho_m}\mathbf{v}_{dj}\mathbf{v}_{dj}\right]+\rho_m\mathbf{g}+\mathbf{m}_m \tag{A.29}$$

A.1.4. Disperse-Phase Transport Equation

The derivation of the disperse-phase transport equation for drift-flux model starts from the dispersed-phase continuity equation. Rewritten Equation A.11, the continuity equation for the dispersed-phase is:

$$\frac{\partial\alpha_2\rho_2}{\partial t}+\nabla\cdot\alpha_2\rho_2\mathbf{v}_2=0 \tag{A.30}$$

Using definitions of:

$$\mathbf{v}_2=\mathbf{v}_{2m}+\mathbf{v}_m \tag{A.31}$$

$$\mathbf{v}_{2m}=\frac{\rho_1}{\rho_m}\mathbf{v}_{2j} \tag{A.32}$$

To the Equation A.11 results in the following form:

$$\frac{\partial\alpha_2\rho_2}{\partial t}+\nabla\alpha_2\rho_2\left(\mathbf{v}_m+\frac{\rho_1}{\rho_m}\mathbf{v}_{2j}\right)=0 \tag{A.33}$$

Rearranging gives **the disperse-phase transport equation**:

$$\frac{\partial\alpha_2\rho_2}{\partial t}+\nabla\alpha_2\rho_2\mathbf{v}_m=-\nabla\left(\frac{\alpha_2\rho_1\rho_2}{\rho_m}\right)\mathbf{v}_{2j} \tag{A.34}$$

A.2. Validation of Simulated SSC

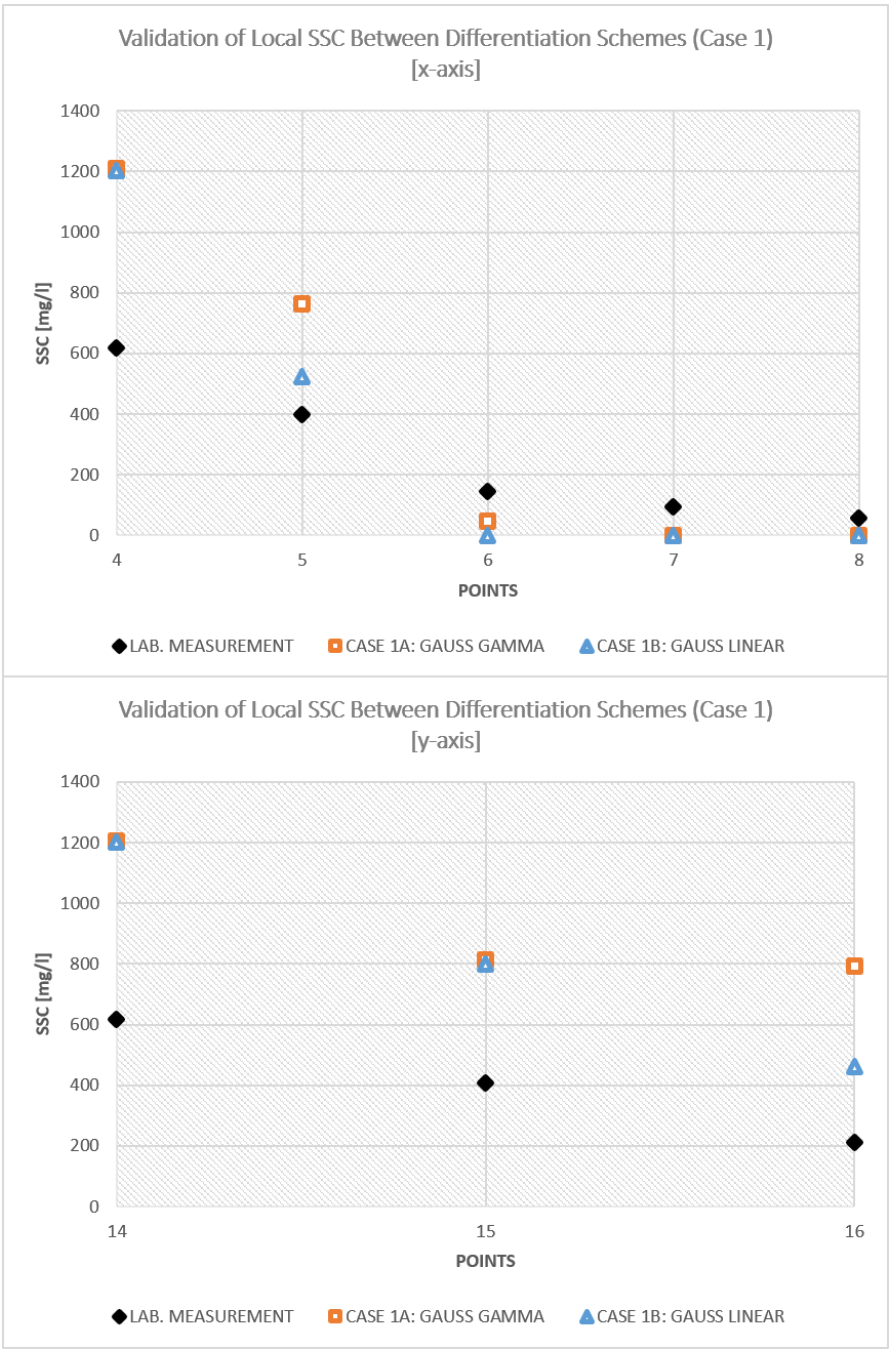

Figure A.1: SSC comparison of laboratory measurement and Case 1A & 1B

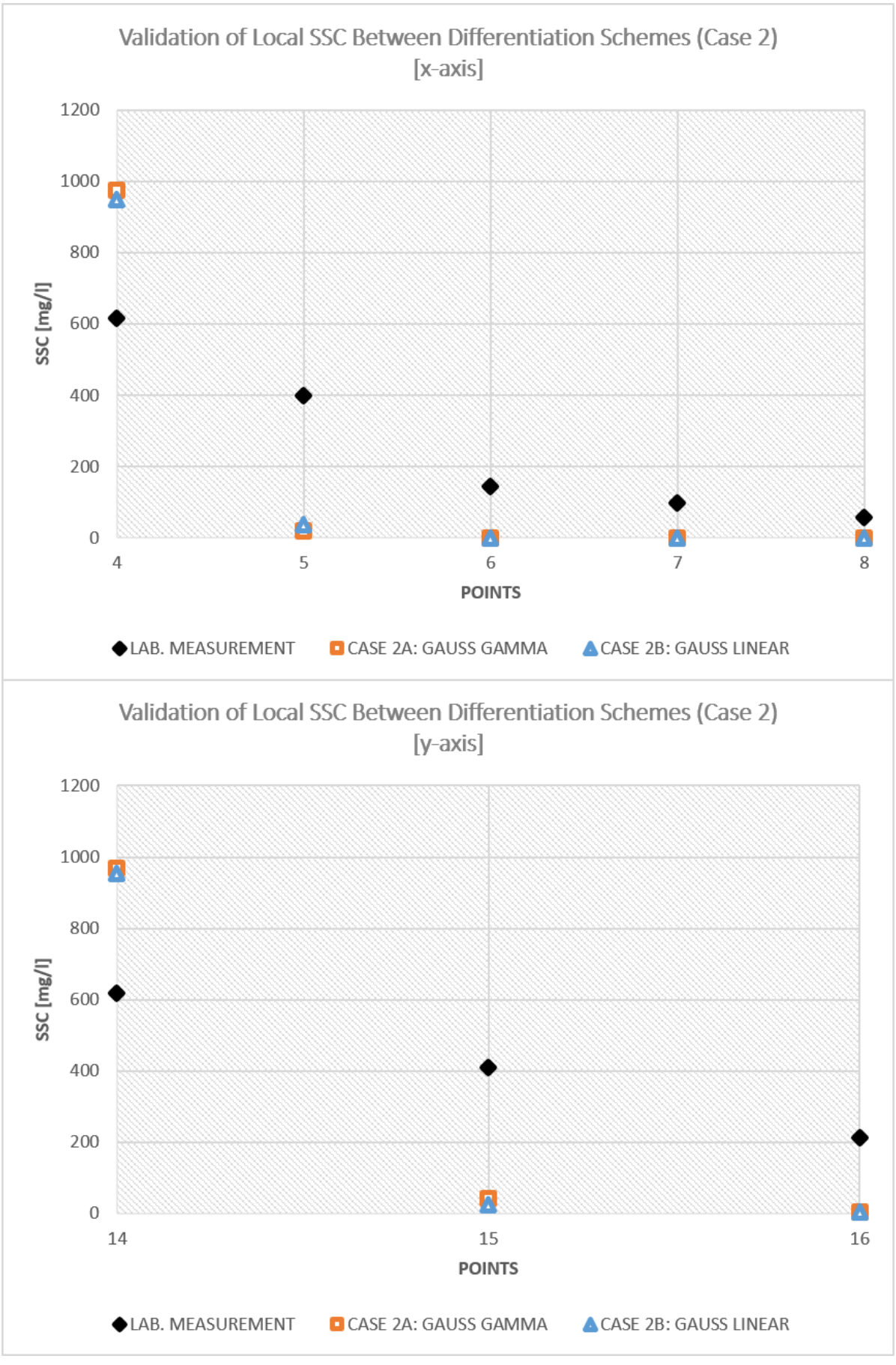

Figure A.2: SSC comparison of laboratory measurement and Case 2A & 2B

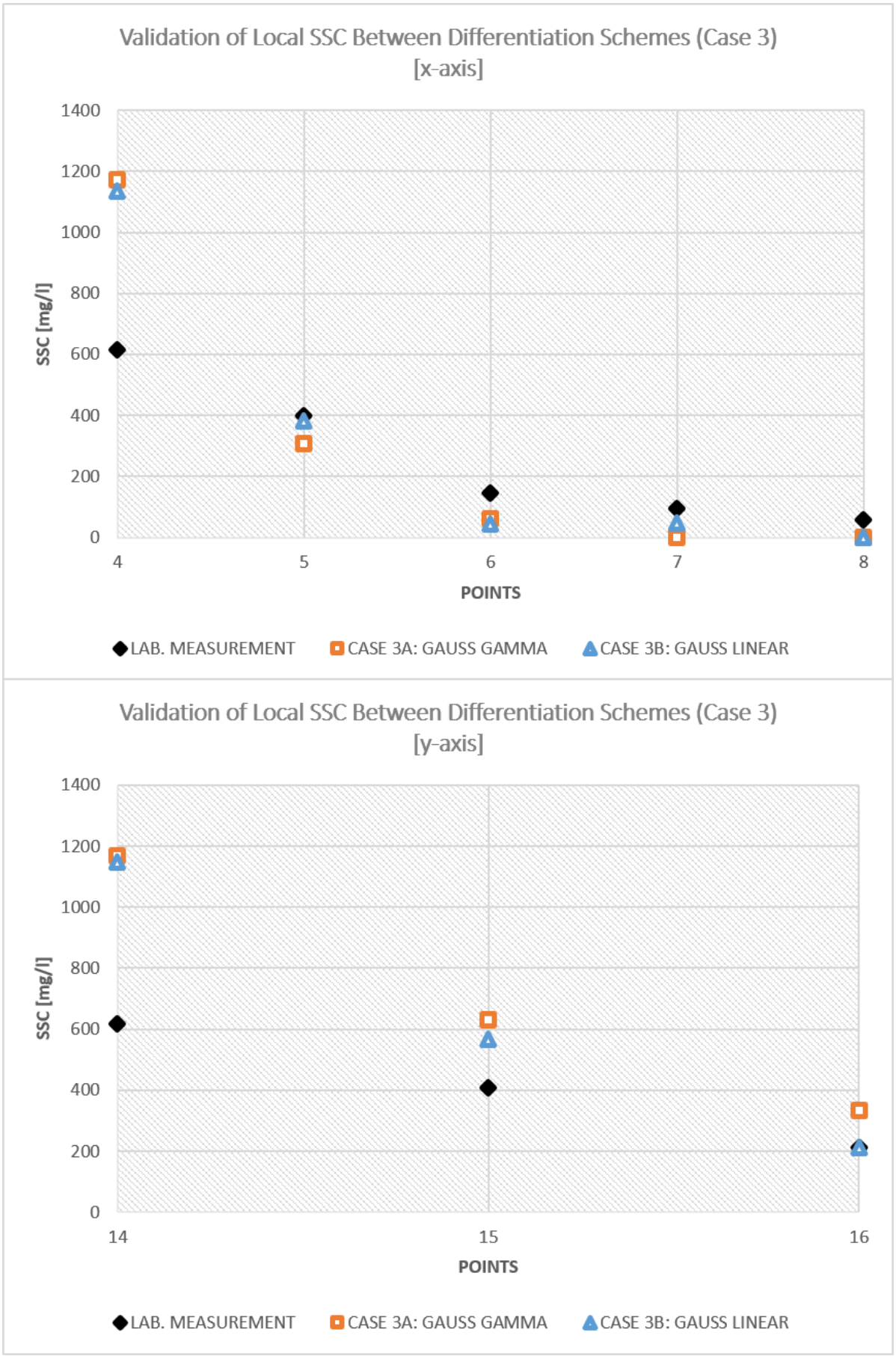

Figure A.3: SSC comparison of laboratory measurement and Case 3A & 3B

Bibliography

Dhafar Ibrahim Ahmed. *Experimental and numerical study of model gravity currents in coastal environment: bottom gravity currents*. PhD thesis, 2017.

Daniel Brennan. *The numerical simulation of two phase flows in settling tanks*. PhD thesis, Imperial College London (University of London), 2001.

Protogene Byishimo. Experiments and 3d cfd simulations of deep-sea mining plume dispersion and seabed interactions. 2018.

Mijanur R Chowdhury and Firat Y Testik. Axisymmetric underflows from impinging buoyant jets of dense cohesive particle-laden fluids. *Journal of Hydraulic Engineering*, 141(3):04014079, 2014.

Paul Cooper and Gary R Hunt. Impinging axisymmetric turbulent fountains. *Physics of fluids*, 19(11):117101, 2007.

Lynyrd De Wit. 3d cfd modelling of overflow dredging plumes. 2015.

Józef Dubiński. Sustainable development of mining mineral resources. *Journal of Sustainable Mining*, 12(1): 1–6, 2013.

Tanushree Dutta, Ki-Hyun Kim, Minori Uchimiya, Eilhann E Kwon, Byong-Hun Jeon, Akash Deep, and Seong-Taek Yun. Global demand for rare earth resources and strategies for green mining. *Environmental Research*, 150:182–190, 2016.

RI Ferguson and M Church. A simple universal equation for grain settling velocity. *Journal of sedimentary Research*, 74(6):933–937, 2004.

Joel H Ferziger and Milovan Peric. *Computational methods for fluid dynamics*. Springer Science & Business Media, 2012.

JC Goeree. *Drift-flux modeling of hyper-concentrated solid-liquid flows in dredging applications*. PhD thesis, Delft University of Technology, 2018.

Christopher J Greenshields. Openfoam user guide. *OpenFOAM Foundation Ltd, version*, 3(1):e2888, 2015.

Porter Hoagland, Stace Beaulieu, Maurice A Tivey, Roderick G Eggert, Christopher German, Lyle Glowka, and Jian Lin. Deep-sea mining of seafloor massive sulfides. *Marine Policy*, 34(3):728–732, 2010.

Mamoru Ishii and Takashi Hibiki. *Thermo-fluid dynamics of two-phase flow*. Springer Science & Business Media, 2010.

Hrvoje Jasak. Error analysis and estimation for the finite volume method with applications to fluid flows. 1996.

Gerhard H Jirka and Robert L Domeker. Hydrodynamic classification of submerged single-port discharges. *Journal of hydraulic engineering*, 117(9):1095–1112, 1991.

NB Kaye and GR Hunt. Overturning in a filling box. *Journal of Fluid Mechanics*, 576:297–323, 2007.

Nikolas E Kotsovinos. Axisymmetric submerged intrusion in stratified fluid. *Journal of hydraulic engineering*, 126(6):446–456, 2000.

Gregory A Lawrence and Michael R Maclatchy. Radially spreading buoyant flows. *Journal of Hydraulic Research*, 39(6):583–590, 2001.

Joseph Hun-wei Lee and Vincent Chu. *Turbulent jets and plumes: a Lagrangian approach*. Springer Science & Business Media, 2012.

EJ List. Turbulent jets and plumes. *Annual review of fluid mechanics*, 14(1):189–212, 1982.

Mikko Manninen, Veikko Taivassalo, Sirpa Kallio, et al. On the mixture model for multiphase flow. 1996.

Kathryn A Miller, Kirsten F Thompson, Paul Johnston, and David Santillo. An overview of seabed mining including the current state of development, environmental impacts, and knowledge gaps. *Frontiers in Marine Science*, 4:418, 2018.

F Moukalled, L Mangani, M Darwish, et al. The finite volume method in computational fluid dynamics. *An advanced introduction with OpenFoam® and Matlab®. Nueva York: Springer. Recuperado de http://www. gidropraktikum. narod. ru/Moukalled-et-al-FVM-OpenFOAM-Matlab. pdf*, 2016.

Stephen B Pope. Turbulent flows, 2001.

Eva Ramirez-Llodra, Hilde C Trannum, Anita Evenset, Lisa A Levin, Malin Andersson, Tor Erik Finne, Ana Hilario, Belinda Flem, Guttorm Christensen, Morten Schaanning, et al. Submarine and deep-sea mine tailing placements: a review of current practices, environmental issues, natural analogs and knowledge gaps in norway and internationally. *Marine Pollution Bulletin*, 97(1-2):13–35, 2015.

JF Richardson and WN Zaki. Sedimentation and fluidisation: Part i. *Chemical Engineering Research and Design*, 75:S82–S100, 1997.

E Robertson, V Choudhury, S Bhushan, and DK Walters. Validation of openfoam numerical methods and turbulence models for incompressible bluff body flows. *Computers & Fluids*, 123:122–145, 2015.

PN Rowe. A convenient empirical equation for estimation of the richardson-zaki exponent. *Chem. Eng. Sci.*, 42:2795–2796, 1987.

Rahul Sharma. Environmental issues of deep-sea mining. *Procedia Earth and Planetary Science*, 11:204–211, 2015.

F van Grunsven, G Keetels, and C van Rhee. Modeling offshore mining turbidity sources. *WODCON XXI: Innovations in dredging*, 2016.

Henk Kaarle Versteeg and Weeratunge Malalasekera. *An introduction to computational fluid dynamics: the finite volume method*. Pearson education, 2007.

David C Wilcox et al. *Turbulence modeling for CFD*, volume 2. DCW industries La Canada, CA, 1998.

Novak Zuber and JAa Findlay. Average volumetric concentration in two-phase flow systems. *Journal of heat transfer*, 87(4):453–468, 1965.